

1978

# Pixel displacement determination in cascaded images utilizing coherent light fringe patterns

Gary Alvin Granneman  
*Iowa State University*

Follow this and additional works at: <https://lib.dr.iastate.edu/rtd>

 Part of the [Electrical and Electronics Commons](#)

## Recommended Citation

Granneman, Gary Alvin, "Pixel displacement determination in cascaded images utilizing coherent light fringe patterns " (1978).  
*Retrospective Theses and Dissertations*. 6388.  
<https://lib.dr.iastate.edu/rtd/6388>

This Dissertation is brought to you for free and open access by the Iowa State University Capstones, Theses and Dissertations at Iowa State University Digital Repository. It has been accepted for inclusion in Retrospective Theses and Dissertations by an authorized administrator of Iowa State University Digital Repository. For more information, please contact [digirep@iastate.edu](mailto:digirep@iastate.edu).

## INFORMATION TO USERS

This was produced from a copy of a document sent to us for microfilming. While the most advanced technological means to photograph and reproduce this document have been used, the quality is heavily dependent upon the quality of the material submitted.

The following explanation of techniques is provided to help you understand markings or notations which may appear on this reproduction.

1. The sign or "target" for pages apparently lacking from the document photographed is "Missing Page(s)". If it was possible to obtain the missing page(s) or section, they are spliced into the film along with adjacent pages. This may have necessitated cutting through an image and duplicating adjacent pages to assure you of complete continuity.
2. When an image on the film is obliterated with a round black mark it is an indication that the film inspector noticed either blurred copy because of movement during exposure, or duplicate copy. Unless we meant to delete copyrighted materials that should not have been filmed, you will find a good image of the page in the adjacent frame.
3. When a map, drawing or chart, etc., is part of the material being photographed the photographer has followed a definite method in "sectioning" the material. It is customary to begin filming at the upper left hand corner of a large sheet and to continue from left to right in equal sections with small overlaps. If necessary, sectioning is continued again—beginning below the first row and continuing on until complete.
4. For any illustrations that cannot be reproduced satisfactorily by xerography, photographic prints can be purchased at additional cost and tipped into your xerographic copy. Requests can be made to our Dissertations Customer Services Department.
5. Some pages in any document may have indistinct print. In all cases we have filmed the best available copy.

**University  
Microfilms  
International**

300 N. ZEEB ROAD, ANN ARBOR, MI 48106  
18 BEDFORD ROW, LONDON WC1R 4EJ, ENGLAND

7907251

GRANNEMAN, GARY ALVIN  
PIXEL DISPLACEMENT DETERMINATION IN CASCADED  
IMAGES UTILIZING COHERENT LIGHT FRINGE  
PATTERNS.

IOWA STATE UNIVERSITY, PH.D., 1978

University  
Microfilms  
International 300 N. ZEEB ROAD, ANN ARBOR, MI 48106

© 1979

GARY ALVIN GRANNEMAN

All rights reserved

Pixel displacement determination in cascaded images  
utilizing coherent light fringe patterns

by

Gary Alvin Granneman

A Dissertation Submitted to the  
Graduate Faculty in Partial Fulfillment of  
The Requirements for the Degree of  
DOCTOR OF PHILOSOPHY

Major: Electrical Engineering

Approved:

Signature was redacted for privacy.

In Charge of Major Work

Signature was redacted for privacy.

~~For the Major~~ Department

Signature was redacted for privacy.

For the Graduate College

Iowa State University  
Ames, Iowa  
1978

Copyright © Gary Alvin Granneman, 1979.  
All rights reserved.

## TABLE OF CONTENTS

	Page
1. INTRODUCTION	1
1.1. General	1
1.2. The Specific Problem	4
2. BACKGROUND	8
2.1. Introduction	8
2.2. Mathematical Description of Light Waves	8
2.3. Irradiance	12
2.4. Diffraction and Interference of Light	12
2.5. Fraunhofer Diffraction and the Fourier Transform of an Aperture	14
3. LITERATURE REVIEW	19
4. ONE-DIMENSIONAL RECORDS	26
4.1. Theory	26
4.1.1. Introduction	26
4.1.2. Shift in exposure	27
4.1.3. The H - D curve and density records	32
4.1.4. Complex exponentiated records	36
4.1.5. Computer model	40
4.1.6. Random signal generation	46
4.1.7. Results	48
4.1.8. Cascaded records	65
4.1.9. Conclusions	66
4.2. Experimental Realization	67

4.2.1.	Introduction	67
4.2.2.	Calibration	70
4.2.3.	Random signal	74
4.2.4.	Signal spectrum whitening	75
4.2.5.	Experimental results	78
4.2.6.	Conclusions	83
5.	TWO-DIMENSIONAL RECORDS	85
5.1.	Introduction	85
5.2.	Theory	85
5.3.	Experimental Realization	98
5.3.1.	Introduction	98
5.3.2.	Apparatus	101
5.3.3.	Calibration	102
5.3.4.	Signal spectrum whitening	105
5.3.5.	Fresnel zone ring "correlation"	110
5.3.5.1.	"Autocorrelation" and zone ring diameter versus plate separation	111
5.3.5.2.	"Autocorrelation" with zone ring offset	114
5.3.5.3.	"Cross correlation," absorption versus phased inputs	116
5.3.6.	Some experimental examples	120
5.3.6.1.	Terrain stereotrans- parencies	120
5.3.6.2.	SEM stereotrans- parencies	123

5.3.6.3.	Beam deflection transparencies	123
6.	CONCLUSIONS AND RECOMMENDATIONS	126
6.1.	Conclusions	126
6.2.	Recommendations	129
7.	BIBLIOGRAPHY	131
8.	ACKNOWLEDGEMENTS	135
9.	APPENDIX	136
9.1.	Introduction	136
9.2.	The Fourier Transform	136
9.3.	Transfer Through Open Space	137
9.4.	Transfer Through a Convex Lens	138
9.5.	Some Common Transform Pairs Used in Optical Computing	139

## 1. INTRODUCTION

### 1.1. General

One signal searching for itself within another signal is a simple definition of correlation. If the two signals are exactly alike, except for a position shift, this procedure is called autocorrelation. If the two signals are not exactly alike, this procedure is called cross correlation. In either case, the correlation function gives a measure of the fit or likeness of the signals as a function of their relative displacement with respect to each other.

The use of a correlation function for the determination of the degree of fit versus displacement in one-dimensional signals is found in many disciplines. For example, real-time correlation receivers (1) are used to optimally detect a known signal amongst multiply-shifted signals. Off line digital techniques are used to compute a correlation function to determine the propagation delay for Tropospheric Scatter studies by a RAKE (2) receiver. A special digital technique (3,4) is used to identify noise sources by their coherent output power spectrum. It takes advantage of multipath propagation delays from source to sensor to compute a special correlation function. Radio astronomy (5) uses multiply-positioned receiver sites to induce known

delays between received signals. These known delays are used in data processing and mapping of signal sources. Passive sonar systems also use multiple sensor sites and detect time delays between received signals by correlation techniques. These delays or shifts are used to determine a source's location in a hyperbolic navigation system.

Interest in using correlation for detection of signal shifts in two-dimensional signals e.g., optical images, is increasing rapidly. Initial work was in the area of photogrammetry for the determination of parallax between stereotransparencies. Parallax is a measurement of pixel shift caused by a change in a viewing position. Parallax is used to determine elevation contours in topographic mapping. Today, modern digital computer techniques are used (6) to compute parallax by correlation of electrical signals representing digitized picture elements.

Since the development of the laser in 1960, both holography and coherent optical data processing have been used to determine parallax. The two major types of techniques used in this area are image-image correlation (7,8,9) and image-matched filter correlation (10,11,12,13, 14). Göpfert (10) gives an extensive list of references in this area up to 1976. Correlation by complex expo-

mentation (10,15) has significance as an accurate method in the determination of the shift instead of the "degree of fit" obtained by conventional correlation techniques. The determination of small displacements and strains in three dimensional physical devices is another area of special interest in optical data processing. For example, holographic interferometry (16,17) readily allows for the measurement of very small motion (a few wavelengths of light) parallel to the illumination direction. Speckle diffraction interferometry (18) is suited for measurement of motion transverse to the illumination direction. These techniques are complementary, but each has its own specific limitations; not the least of which is the need for laser illumination of the original object. This dissertation addresses ways to overcome some of these limitations.

All of the above mentioned signal processing systems can be classified as one of two major types. The first type is where a known signal source is available. This allows the signal processing solution to take advantage of known a priori signal details. Characteristics such as probability distribution, coding format, waveform or time delay are used to optimally process the signal. Typically, the system output is a likeness of the original signal.

of-fit in the normal correlation sense, but provides a good measure of the relative displacement of the pixels.

The single major disadvantage is the need for the input signal record to contain at least a minimum high spacial frequency content. But if not naturally occurring, this can be artificially induced by such techniques as texturing the surface of an object prior to making the photographs.

Examples of a priori known signal processing systems are real-time correlation and matched filter receivers. Optical systems for image-matched filter correlation also require known a priori images from which to construct the matched filter.

The second type of signal processing system is one concerned with the detection and processing of signals with unknown a priori details. Here, system design cannot be limited to optimally process "a" signal but must be capable of processing random or at least band limited signals. This is a very demanding design criterion for the processor. Many times the desirable system is not an exact likeness of the input but rather a measure of the signal magnitude, and/or the position shift relative to another signal. Examples of systems designed to process unknown a priori signals are radio astronomy receivers, passive sonar detectors, and noise location by coherent power spectrum analysis. Optical image-image correlation systems are also examples of two-dimensional signal processors of this type.

### 1.2. The Specific Problem

Optical schemes for the determination of signal shifts can be classified as one of three types. The

first type correlates optical transparencies by either image-image or image-matched filter techniques. The problems of conventional correlations with density transparencies as inputs are many. The increased absorption of density inputs greatly decreases the correlation signal output; especially with low signal-to-noise ratios. Although preprocessing of absorption transparencies to increase the output intensity can be done, contrast balancing and high frequency bandpass filtering are demanding in time and effort. Furthermore, the "correlation spot" is often rather large, making the determination of its exact center difficult.

The phasing (bleaching) of inputs to conventional image-image correlators and image-matched filter correlators has greatly improved their output intensity and signal-to-noise ratio, but determination of its exact center of location remains difficult. Additional preprocessing such as making positive and negative image transparencies and holographically formed mask images are still required in most systems.

Holographic interferometry is another totally different scheme for the determination of differential displacements of surfaces in a direction parallel to the direction of illumination. It is advantageous in the

detection of small motions of macroscopic objects (room-sized or smaller). Disadvantages are the requirements of coherent illumination, mechanically rigid exposure systems, and limited motion (a maximum of a few wavelengths of the illumination source).

A third scheme, speckle diffraction interferometry, is another totally different technique for the determination of differential displacements of surfaces with motion perpendicular to the direction of illumination. Advantages are the ability to detect in-plane motion, the direction of the motion, and a greater range of motion compared to holographic interferometry. Disadvantages are the need for coherent illumination, for mechanically rigid exposure systems, and a limited range of detectable in-plane motion.

A new type of optical image-image "quasi-correlation" technique is proposed and developed in this dissertation. This quasi-correlation technique has shown itself to be quite capable for the determination of in-plane differential displacements. Pixel motion of any magnitude between one image and a second image have been readily detectable to within a few micrometers in the image coordinate system. Advantages are use of non-coherent illumination to make the original records,

simple and separate photographic exposures, simple preprocessing, and minimal system rigidity. The single major disadvantage is the need for the record to contain at least a minimum high spacial frequency content. If not naturally occurring, this can be artificially induced by such techniques as texturing the surface of an object prior to making the photographs. The output of this scheme is not a measure of correctness of fit in the normal correlation sense, but it provides a good measure of relative displacement.

The general applicability of the technique is demonstrated by application to terrain stereotransparencies, SEM stereotransparencies, and mechanical beam deflection transparencies.

## 2. BACKGROUND

### 2.1. Introduction

In this section a brief review of some basic topics involved with optical data processing are presented. It is the author's intent to present only a tutorial level of discussion so as to aid the reader. Each topic can be investigated in greater depth by referring to one of several texts such as; Born and Wolf (19) on geometrical optics, Bracewell (20) on the Fourier Transform and its applications, and Goodman (7) or Preston (21) on optical data processing.

### 2.2. Mathematical Description of Light Waves

Quasi-monochromatic, linearly polarized light from a laser source can be described by a real-valued scalar function of position and time. If we assume that this scalar function corresponds to a rectangular component of the electric field vector of the light wave field, it can be written as

$$U(x,y,z;t) = a(x,y,z) \cos [2\pi v_0 t - \phi(x,y,z)] \quad (2.1)$$

where

$v_0$  = temporal frequency of the wave

$a(x,y,z)$  = magnitude of the wave

and the argument of the cosine function is the phase of the wave. The surfaces in space described by  $\phi(x,y,z) = \text{constant}$  are said to be wavefronts. By defining a space varying function called the complex amplitude of the wavefield as

$$u(x,y,z) = a(x,y,z) e^{j\phi(x,y,z)} \quad (2.2)$$

Equation (2.1) can be written as

$$u(x,y,z;t) = \text{RE} \left\{ u^*(x,y,z) e^{j2\pi\nu_0 t} \right\} \quad (2.3)$$

where  $\text{RE} \{ \}$  is the "real part" operator and  $*$  indicates the complex conjugate. Goodman (7) and others have shown that Equation (2.2) must be a solution of the time-independent Helmholtz equation, and it may, therefore, be used to solve many problems of interest without carrying along the time-varying part.

The complex amplitude of a plane wave traveling with direction cosines  $(\alpha, \beta, \gamma)$  can be written as

$$u(x,y,z) = A e^{jk(\alpha x + \beta y + \gamma z)} \quad (2.4)$$

where  $\alpha^2 + \beta^2 + \gamma^2 = 1$ ,  $A = \text{constant}$ , and  $|\vec{k}| = 2\pi/\lambda$ .

Our primary interest in this dissertation is with the propagation of light from one plane ( $z = z_1$ ) to another plane ( $z = z_2$ ). For simplicity, the complex amplitude at a plane ( $z = z_i$ ) can be denoted by

$$u_i(x, y) = u(x, y, z_i)$$

Then the complex amplitude of a general plane wave at plane  $z = z_1$  can be written as

$$\begin{aligned} u_1(x, y) &= A e^{jk(\alpha x + \beta y + \gamma z_1)} \\ &= A e^{jk\gamma z_1} e^{jk(\alpha x + \beta y)} \\ &= A' e^{jk(\alpha x + \beta y)} \end{aligned} \quad (2.5)$$

where the constant  $e^{jk\gamma z_1}$  has been combined with  $A$  to give  $A'$ .

Similarly the complex amplitude distribution of a spherical wave at plane  $z = z_2$ , radiating from a point source at a point  $(a, b, z_1)$  in plane  $z = z_1$  can be written (7) as

$$u_2(x, y) = \frac{\cos \theta}{j\lambda d_{12}} e^{jkd_{12}} \quad (2.6)$$

where  $d_{12} = \sqrt{(z_2 - z_1)^2 + (x-a)^2 + (y-b)^2}$  and  $\theta$  is the angle between  $k$  and the  $z$ -axis is shown in Figure 2.1.

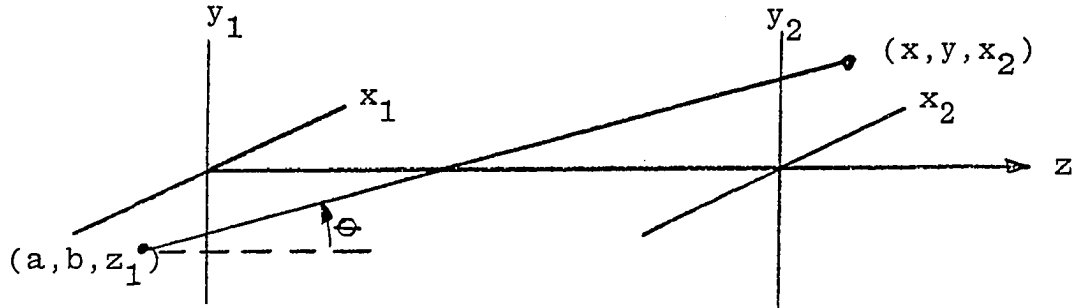


Figure 2.1. Spherical wave propagation geometry

If we restrict the source and observation points to regions near the  $z$ -axis, whose sizes are small compared to  $z_2 - z_1 = z_{12}$ , and if

$$z_{12}^3 \gg \frac{\pi}{4\lambda} \left[ (x-a)^2 + (y-b)^2 \right]_{\max}^2 \quad (2.7)$$

then Equation (2.6) may be approximated as

$$\begin{aligned} u_2(x, y) &= \frac{e^{jkz_{12}}}{j\lambda z_{12}} e^{j\pi/\lambda z_{12} [(x-a)^2 + (y-b)^2]} \\ &= B_{12} e^{j\pi/\lambda z_{12} [(x-a)^2 + (y-b)^2]} \end{aligned} \quad (2.8)$$

where  $B_{12}$  is the complex constant  $e^{jkz_{12}}/j\lambda z_{12}$ . This representation of a spherical wavefront by a parabolic

wavefront is a common practice and greatly simplifies computation.

### 2.3. Irradiance

Irradiance is a measure of the radiant-flux density (e.g., power per unit area) incident on a surface and is measured in Watts/square meter. It is irradiance rather than field intensity that almost all detectors at optical wavelengths respond to. For monochromatic light, the irradiance distribution can be computed from the complex amplitude function directly as

$$I(x,y,z) = |U(x,y,z)|^2 \quad (2.9)$$

This eliminates the necessity of computing the time average of the square of Equation (2.1) for nonmonochromatic light.

### 2.4. Diffraction and Interference of Light

The basic mechanisms involved in most coherent optical systems are wave interaction and diffraction phenomena. When two wave trains superimpose, there is a wave interaction called interference. If the two waves have a constant phase difference at a fixed point, and

nearly equal wavelength, amplitude, polarization and direction of travel, a well-defined interference pattern may be observed. In 1802, Thomas Young performed the first recorded experiment revealing an interference pattern due to the superposition of wave trains from two pin holes. Figure 2.2 is a simplified representation of Young's experiment.

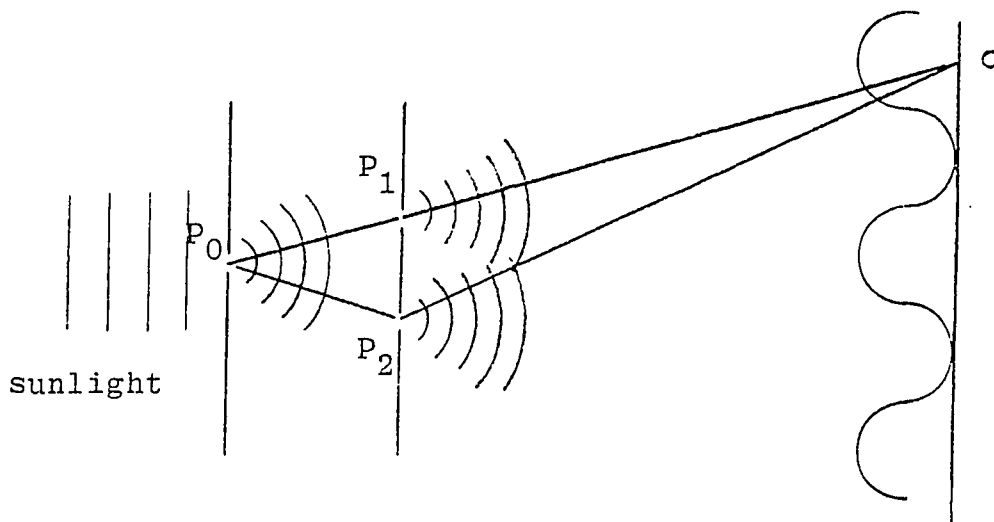


Figure 2.2. Young's interference experiment

Of special interest is that constructive interference occurs when the path length difference is  $\lambda$  and, therefore, a maximum in intensity occurs as represented at a point o on the observation screen. For a path length difference of  $\lambda / 2$  a minimum in intensity occurs.

Diffraction has been conveniently defined by

Sommerfeld (22) as "any deviation of light rays from rectilinear paths which cannot be interpreted as reflections or refraction." When waves pass through an aperture or past the edge of an obstacle, they always spread to some extent into the region which is not directly exposed to the oncoming waves.

## 2.5. Fraunhofer Diffraction and the Fourier Transform of an Aperture

The diffraction effects of apertures and obstacles are commonly classified as Fraunhofer (far-field) and Fresnel (near-Field) diffraction. Fraunhofer diffraction represents the special case where the light source and the observation point are both moved to infinity. This is of particular importance because it applies in optical systems when the light source and observation point are conjugate image points of one another. Thus, the diffraction seen at the focal point of a simple lens is the Fraunhofer diffraction pattern and its intensity distribution has been shown (7,20,21) to be proportional to the Fourier Transform of the aperture.

Consider the cross-sectional view of a multiple slit aperture of Figure 2.3 with plane wave illumination. For simplicity, an aperture with equal widths of openings

and spacings was chosen. Also, the slit length (into the plan of the paper) is large compared to the slit width  $a$ .

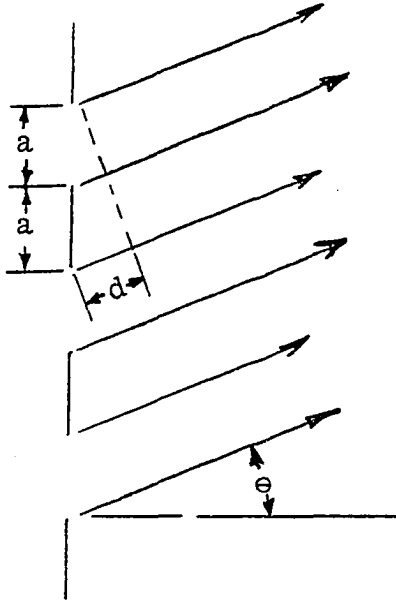


Figure 2.3. Fraunhofer diffraction from a multiple slit

For an angle  $\theta$  the distance  $d$  is

$$d = 2a \sin \theta \quad (2.10)$$

Then any two parallel diffracted wave trains have a relative phase difference of

$$\Delta\phi = 2\pi \frac{d}{\lambda} \quad (2.11a)$$

Substituting Equation (2.10) into (2.11a) gives

$$\Delta\phi = 2\pi \frac{2a}{\lambda} \sin \theta \quad (2.11b)$$

Maximum constructive interference at the far-field occurs when the phase difference  $\Delta\phi$  is an integer multiple of  $2\pi$ . Setting  $\Delta\phi = m2\pi$ ,  $m=0, 1, 2, 3, \dots$  in Equation (2.11b) gives

$$\Delta\phi = m2\pi = 2\pi \frac{2a}{\lambda} \sin \theta$$

$$\frac{m\lambda}{a} = \sin \theta$$

$$\theta_m = \arcsin \frac{\lambda m}{2a}, m=0, 1, 2, 3 \quad (2.12)$$

The angles  $\theta_m$  for various values of  $m$  are the angles where the parallel diffracted wave trains have a relative phase difference of  $m2\pi$ . Now if the aperture is placed in front of a double convex lens (see Figure 2.4) each set of parallel diffracted waves at an angle  $\theta_m$  will be focused to a point in the lens' focal plane one focal length  $F_L$  behind the lens.

By similar triangles in Figure 2.4 we can write

$$\frac{m\lambda}{2a} = \sin \theta = \frac{x_2}{F_L} m \quad (2.12b)$$

or

$$x_{2m} = \frac{m\lambda}{2a} F_L = m f_x \lambda F_L \quad (2.13)$$

where  $\frac{1}{2a} = f_x$ , the spacial frequency of the multiple slit aperture.

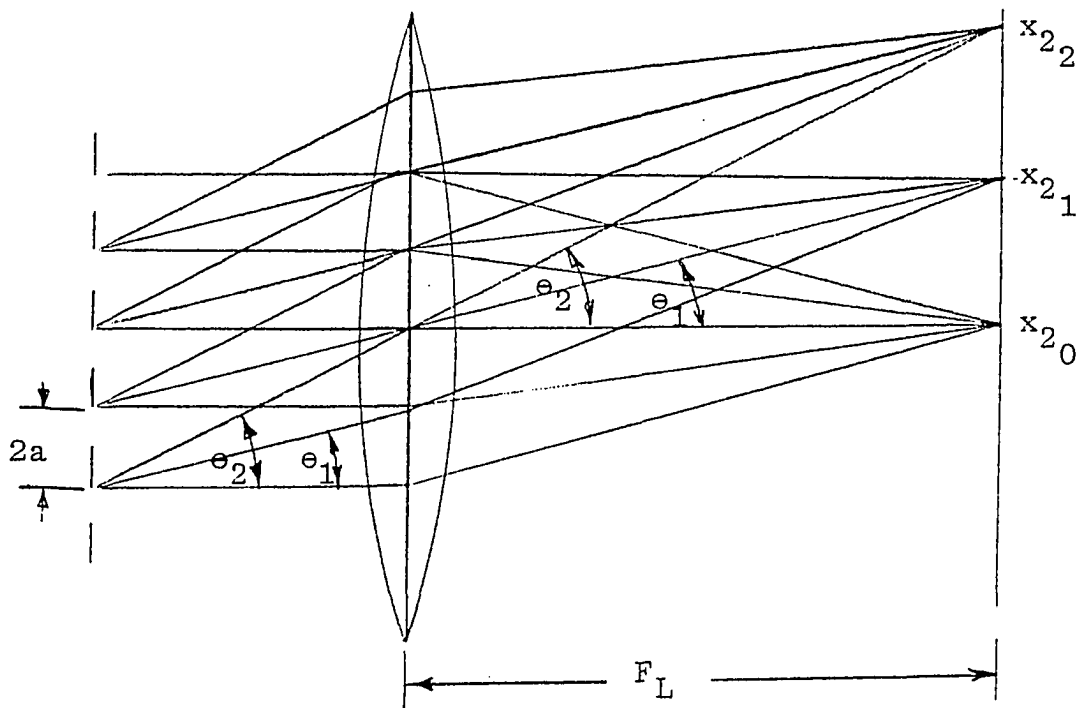


Figure 2.4. Fraunhofer diffraction using a convex lens

Equation (2.13) gives the distance of the  $m^{\text{th}}$  order constructive interference spot from the zero-order (optical axis) interference spot. The intensity and location of each interference spot is, therefore, proportional to the magnitude of and order of the  $m^{\text{th}}$

order coefficient of the Fourier Transform of the transmittance function of the aperture.

A more detailed mathematical treatment of definitions, relationships and Fourier Transform pairs is given in the Appendix.

### 3. LITERATURE REVIEW

In 1948, Dennis Gabor (23) published a paper giving a solution to the problem of the limited resolving power of the then newly developed electron microscope. The resolving power fell short of the theoretical limit of  $4\text{\AA}$  (0.4 nanometers) mainly because of spherical aberration errors which caused excessive blurring in the magnified recorded image. His solution was to go ahead and take a bad electron picture, but one which contains the "whole" information, and correct it by optical means. This could be done, if at all, only with a coherent electron beam, with electron waves which have a definite phase. But an ordinary photograph loses the phase completely; it records only the intensity. His basic solution was to add a coherent reference wave along with the object wave, which together produce interference fringes. The fringes then capture the relative phase between the object and reference beam. Recorded as a photograph and reilluminated with the reference wave alone, the original objects' waves are then reproduced with correct amplitude and phase. This recording of the whole picture Gabor called a "hologram" from the Greek word "holos"-- the whole.

Those first holograms were made with an inline geometry with the light reference source, the object, and the

recording media along a straight line. There were many difficulties, but the main one was that of obtaining a coherent light source.

With the development of the laser in 1962, Leith and Upatnieks (24) produced the first holograms with an offset alignment. The new coherent light source and the offset configuration produced superior results. Since then many articles and texts have been written on holography.

During this time period research reported in 1956 by O'Neill (25) and in 1960 by Cutrona, Leith, Palerma, and Porcello (26) developed new ideas and applied many of the theories of linear temporal systems to optical systems. In 1964 Rotz and Vander Lugt (27, 28) implemented an image-match filter technique, made by holographic techniques, for the process of signal detection by complex filtering in coherent optical systems.

Since those early times, encouraged by a reliable coherent light source from a laser, scientific investigators have developed new ideas and new applications in the field of coherent optical data processing. The general area is very active and has seen new publications (e.g., Applied Optics, Optical Engineering, Laser Focus, Electro Optical Systems Design), and international conferences (e.g., the annual International Optical Computing Conference, seven to

date) all devoted to optical data processing (ODP). Stroke's "Optical Computing" (29) lists 51 references, Vander Lugt's "Coherent Optical Processing" (30) lists 151 references and Goodman (31) lists 49 references as further examples of the magnitude of research being conducted and the information available.

Because the "quasi-correlation" technique developed in this paper uses a coherent optical spectrum processor, most of the reference material mentioned is of a general background nature. Furthermore, to the author's knowledge, no other researcher has published information on or used Fresnel zone ring patterns as a means of determining a locational correlation between displaced picture elements (pixels). The present (1978) known optical systems being used are of two types, the image-image and the image-matched filter schemes for optical correlation. The following reviews the most recent and related literature.

Several problems are encountered when cross correlation of stereotransparencies is implemented by image-matched filter techniques. The first problem is the cross correlation output signal deterioration due to image distortions between perspective views of objects with depth. The second problem is the limited spacial frequency spectrum and its exponential roll off (32) of most input signals.

In 1974, Stark and Garcia (33) developed a procedure to enhance the high frequencies of the frequency spectrum by using a special film developer that gives an extremely low film  $\gamma$ . The low  $\gamma$  gives a  $D - \log E$  curve (see Section 4.1.3) which is linear over many orders of exposure magnitude. For a large class of signal sources this is equivalent to "companding", e.g., high frequency enhancement. This has the effect of increasing the space autocorrelation output signal.

Another approach to increasing the correlation output signal has been to phase the input records. Gray and Barnett (13), again using image-matched filtering employed the use of a thermoplastic media for both the frequency plane filter and the input image transparency. They were able to process the frequency plane matched filter in situ (at the frequency plane without moving it). Thus, the severe practical problem of relocating it after processing to an accuracy of the order of a micrometer was eliminated. In as much as continuous tone photographic transparencies tend to have a rather low diffraction, the range of intensities present in the spacial frequency plane is very large, and generally beyond the dynamic sensitivity range of photographic materials used for recording them as matched filters. Therefore, Gray and Barnett chose to use

thermal-plastic media to record input records and thereby achieve what is called in this dissertation "whitening".

Balasubramanian and Bennett (11) have generated contour lines from two stereotransparencies that were phased by bleaching. The phased inputs were used to make an image hologram of one, while the other served as the input to the correlator. Again, the result was to increase the correlation signal output level.

An alternative scheme for inputs to an image-image correlator was recently reported by Wertheimer and Givens (8). The technique is to make a positive transparency from one input photograph and a negative transparency from the other input photograph. A simplifying assumption is that the copies are made within the straight line portion of the H - D curve and the positive and negative film gammas are equal. When the image transparencies are properly inserted into the optical correlator, a contour curve is generated for a given record shift. Adjusting the record shift gives another contour curve. The contour widths, however, are generally wider than those obtained from more classical techniques, and hence less accurate. The technique has greater potential for close range work.

Rotz (12) has described a very sophisticated automatic stereocompilation device, COMAP, which uses the image-matched filter technique. Perhaps its most important

advantage is that it can "find" itself after passing through a region which will not allow any useful correlation (e.g., a snow field or a lake with no detail). The ultimate speed of the COMAP system is limited by three things: input scanning, correlation peak detection, and data processing. The system still uses absorption type input records and holographically produced matched filters.

A common problem for most all stereotransparency input correlators is that input photos must be rectified. Basically, this is a procedure to correct for original camera axis skew from a true vertical. Casasent and Furman (14) describe an optical match-filter system that is capable of correlating nonvertical imagery with no loss in the peak intensity and signal-to-noise ratio, SNR, of the output correlation. From the coordinates of the correlation peak, the tilt angle of one camera and the scale of the image can be determined. The system uses an input transparency preprocessed by a scale transformation and the optical Fourier Transformation property of a lens to effectively compute the Mellin Transformation of the inputs.

With advancements in input devices, such as the pockels readout optical modulator (PROM) by the Itek Corporation (34) and the recent development of the liquid

crystal image transducer (35, 36) by Hughes Research Laboratory, the future promises "real-time" optical data processing. These, and other new techniques, like Fresnel zone ring quasi-correlation, offer expanded possibilities.

## 4. ONE-DIMENSIONAL RECORDS

### 4.1. Theory

#### 4.1.1. Introduction

In reviewing the previous chapters, it becomes obvious that the requirements of coherent illumination and mechanically rigid exposure systems limit the utilization of holographic and speckle diffraction interferometry. The following analysis is of a technique utilizing double exposures or, alternately, cascaded photographic records as inputs. These records are made with noncoherent illumination and conventional photography. This procedure eliminates those two requirements and greatly enhances the opportunity to use optical data processing.

In this analysis we are interested in the basic question of what happens when a double exposed image of an object is made, the first image with the object in one position and the second image with the object displaced and/or distorted from its original position.

Although the primary interest in this chapter is in determining the location of one one-dimensional record in another one-dimensional record, the following analysis is done in two-dimensions, a common practice for optical systems. It is later assumed there is no variation along the second direction.

#### 4.1.2. Shift in exposure

For purposes of mathematical development here, the most basic signals to consider are those corresponding to the original exposure signals that impinge on a recording medium. Let us consider the first exposure to be  $E_{1T}(x,y)$  and the second exposure to be a x-direction displaced version of the first plus a noise component. The noise component accounts for signal differences resulting from recording medium characteristics as well as actual signal differences due to perspective viewing of a three-dimensional object. Thus, the noise of both signals has been combined and represented as one component. The total exposure of the recording medium can be written as

$$E_T(x,y) = E_{1T}(x,y) + \beta E_{1T}(x-x_0,y) + n(x,y) \quad (4.1)$$

where  $\beta$  is a measure of similarity. If the two images are obtained from an electronic imaging system (e.g., SEM or T.V.) where image inverting can be done, the double exposed image can be either the sum or the difference of the two exposures. In order to explicitly denote this possibility, let us assume  $\beta$  to be numerically positive and indicate the sum and/or difference by a  $\pm$  designation. Additionally, it is common practice to write the individual image signals

as the sum of an average plus a variable component.

Therefore, the total exposure of the medium can be written as

$$\begin{aligned} \underline{E}_T &= (1 + \beta) E_{O1} + E_1(x,y) + \beta E_1(x-x_0,y) + n(x,y) \\ &= E_0 [1 + e_1(x,y) + \beta e_1(x-x_0,y)] + n(x,y) \end{aligned} \quad (4.2)$$

where  $E_0 = (1 + \beta) E_{O1}$

and  $e_1(x,y) = E_1(x,y)/E_0$

with  $x_0$  denoting the displacement of the second exposure.

If the Fourier Transform of the exposure  $e_1(x,y)$  is defined as

$$F \left\{ e_1(x,y) \right\} = \underline{E}_1(f_x, f_y)$$

then

$$\underline{E}_T(f_x, f_y) = F \left\{ \underline{E}_T(x,y) \right\} \quad (4.3)$$

$$= E_o \left[ \delta(f_x, f_y) + \underline{E}_1(f_x, f_y) (1 + \beta e^{-j2\pi f_x x_o}) \right] + \underline{N}(f_x, f_y) \quad (4.4a)$$

$$= E_o \left[ \delta(f_x, f_y) + \beta \underline{E}_1 \left( \left( \frac{1-\beta}{\beta} \right) + 1 \pm e^{j2\pi f_x x_o} \right) \right] + \underline{N}(f_x, f_y) \quad (4.4b)$$

$$= E_o \left[ \delta(f_x, f_y) + 2 \beta \underline{E}_1 e^{j\pi f_x x_o} \left( \frac{1-\beta}{2\beta} \right) \cdot e^{-j\pi f_x x_o} + \left[ \begin{array}{c} \cos \pi f_x x_o \\ \text{or} \\ -j \sin \pi f_x x_o \end{array} \right] \right] + \underline{N}(f_x, f_y) \quad (4.4c)$$

where the cosine term is associated with the upper sign (+) and the sine term with the lower sign (-). Looking at the terms and their location as found in the Fourier Transform plane of an optical system we identify:

$$E_o(f_x, f_y) \delta(f_x, f_y) = \text{a weighted average appearing as a point on the optical axis.}$$

and  $\underline{E}_1(f_x, f_y)$  = the signals' Fourier Transform  
distributed throughout the frequency  
plane.

The cosine or the sine term modulates the amplitude of  $\underline{E}_1(f_x, f_y)$  while the exponential term is a temporal phase change of the light from one position to another in the Fourier Transform plane. Because most light recording devices are intensity sensitive, the recorded Fourier Transform plane is therefore

$$\left| \underline{E}_T(f_x, f_y) \right|^2 = \underline{E}_T \underline{E}_T^* \quad (4.5)$$

where \* means the complex conjugate.

To better comprehend what this means, let us assume the noise is negligible and  $\beta$  is unity. The two cases, (+) giving cosine and (-) giving sine modulation, are illustrated in Figure 4.1 for a signal with a spectrum arbitrarily represented as  $\underline{E}_1(f_x, f_y) = \underline{E}_1(f_x) \delta(f_y)$ . Note that the displacement shift  $x_0$  is inversely related to the distance between intensity minimums caused by the sine-cosine modulation terms. Also, note the maximum at zero for the sum (+) and the null at zero for the difference (-)

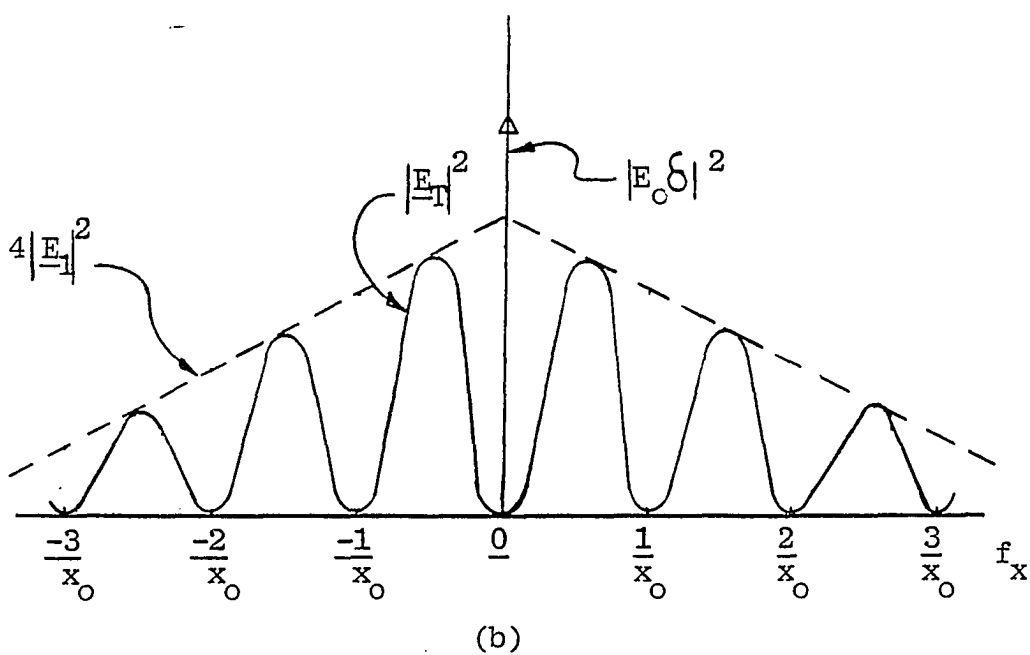
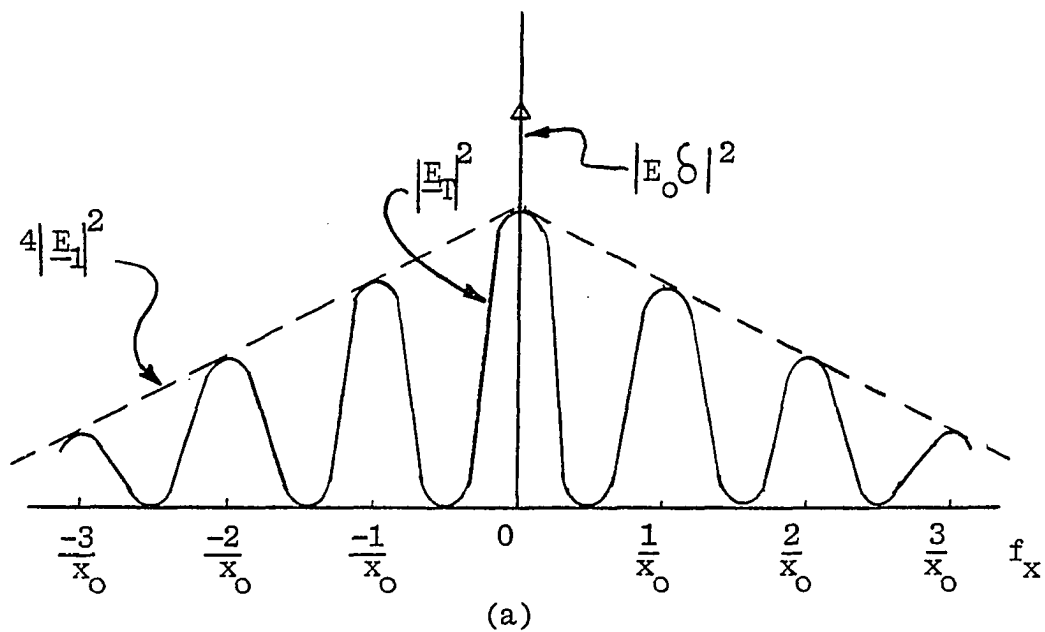


Figure 4.1. Illustrations of the Fourier Transform plane intensity recording for (a) the sum and (b) the difference of two exposures with shifted signals

exposure signals.

The effect of the signals not being identical and with additional noise is a tendency to wash out the distinctness of the fringe pattern. In the instance of small  $\beta$  and large  $n$ , the fringes may not ever be detectable.

#### 4.1.3. The H - D curve and density records

The above mathematical development illustrated that a shift in image exposure signals can be detected as a fringe modulation of the Fourier Transform of the signal. Presently no known coherent optical data processing scheme uses actual exposure signals directly, but some utilize them as a means of modifying another physical property of a receiving device. Our concern is in a way to measure the relative displacement  $x_0$  through the use of photographically recorded images. These images might be absorption or complex exponentiated (i.e. phased) transparencies. We now investigate how well this displacement information transfers through these photographic processes.

The optical density of a photographic transparency as a function of exposure is defined by the Hurter-Driffield curve, better known as the H - D curve. A typical H - D curve is illustrated in Figure 4.2. Even though an exact mathematical expression for the H - D curve may not be

easily obtained, experience shows that the total optical density can be expressed as

$$D_T(x,y) = D_0(1 + d(x,y)) \quad (4.6)$$

where  $D_0$  is the optical density corresponding to  $E_0$  and  $d(x,y)$  is a result of the variation of  $E_1 \pm E_2$  about  $E_0$ . It is also clear that  $d(x,y)$  will have zero crossings at the same  $x,y$  positions as  $e_1(x,y) \pm e_2(x,y)$ . The effect of the nonlinear transformation between exposure,  $E$ , and density,  $D$ , for the two major sections of the  $H - D$  curve is developed next.

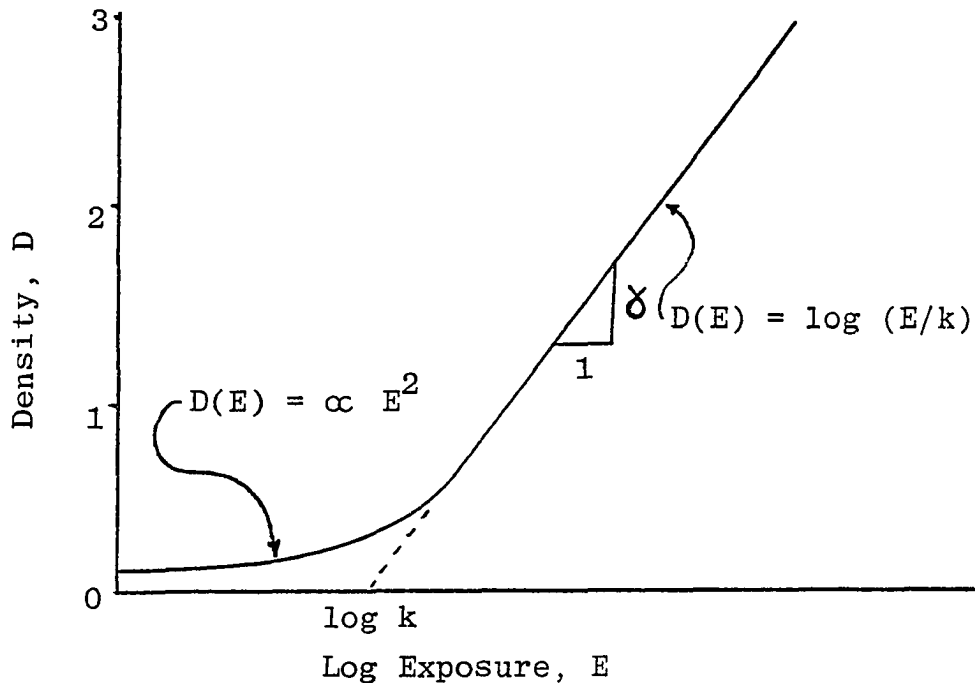


Figure 4.2. A typical  $H - D$  curve

When  $D \lesssim 1$ , the H - D curve can be closely approximated by

$$D(E) = \propto E^2 \quad (4.7)$$

Recalling that  $E = E_0(1 + e_1 \pm e_2)$  and substituting

$$\begin{aligned} D(E) &= \propto E_0^2 (1 + e_1 \pm e_2)^2 \\ &= \propto E_0^2 (1 + 2(e_1 \pm e_2) + (e_1 \pm e_2)^2) \\ &= \propto E_0^2 [1 + 2(e_1 \pm e_2) + e_1^2 \pm 2e_1e_2 + e_2^2] \end{aligned} \quad (4.8)$$

It is now apparent that this nonlinear transformation has definitely recorded the sum or difference signals and also added some higher order terms. It should be noted (see Appendix) that the Fourier Transform of a density recorded transparency is proportional to its amplitude transmission,  $t(x,y)$ . By definition  $t(x,y) \triangleq K e^{-D(x,y)/2}$  when phase effects are neglected. With  $e_2(x,y) = e_1(x-x_0,y)$  it is clear that the Fourier Transforms of  $e_1(x,y) \pm e_1(x-x_0,y)$  and of  $e_1(x,y)^2 + e_1(x-x_0,y)^2$  will both produce an interference pattern superimposed onto the spacial frequency plane with spacing  $1/x_0$ . Recalling the location of fringe nulls from Figure 4.1, we see these fringe patterns

will reinforce each other for sum (+) inputs and will be destructive for difference (-) inputs. Also note that if  $(e_1 \pm e_2) < 1$  then  $(e_1 + e_2)^2 \ll 1$  and these effects are further nullified.

When  $D \gtrsim 1$  the H - D curve can be closely approximated by

$$D(E) = \gamma \log(E/k) = (\gamma / \ln 10) \ln (E/k) \quad (4.9)$$

Letting  $\gamma' = \gamma / \ln 10$  and recalling that  $E = E_0(1 + e_1 \pm e_2)$  allows  $D(E)$  to be written and expanded as

$$D(E) = \gamma' \ln (E_0/k) + \gamma' \ln (1 + e_1 \pm e_2) \quad (4.10a)$$

$$= D_0 + \gamma' \left[ (e_1 \pm e_2) - 1/2(e_1 \pm e_2)^2 + 1/3(e_1 \pm e_2)^3 + \cdots \frac{(-1)^{n-1}}{n} (e_1 \pm e_2)^n \right] \quad (4.10b)$$

$$= D_0 - \gamma' \left[ \sum_{n=1}^{\infty} \frac{(-1)^n}{n} (e_1 \pm e_2)^n \right] \quad (4.10c)$$

$$\begin{aligned}
&= D_0 - \gamma' \sum_{n=1}^{\infty} (-1)^n/n \left[ e_1^n \pm e_1^{n-1} e_2 + \right. \\
&\quad \left. e_1^{n-2} e_2^2 \pm e_1^{n-1} e_2^3 + \cdots + e_1 (\pm e_2)^{n-1} + (\pm e_2)^n \right]
\end{aligned}
\tag{4.10c}$$

Again with  $e_2(x,y) = e_1(x - x_0, y)$ , it is clear that the Fourier Transforms of  $e_1^n \pm e_2^n$  will produce an interference pattern superimposed onto the spacial frequency plane with a spacing of  $1/x_0$ . These fringe patterns will reinforce each other for all sum (+) signals and for  $n =$  even powers of difference (-) type signals. For  $n =$  odd powers the  $e_1^n - e_2^n$  terms cause fringes that are destructive. It is not clear exactly what the cross product terms  $e_1^{n-m} \cdot e_2^m$  will give. However, with  $|e_1 \pm e_2| < 1$ , the dominant term will be  $e_1 \pm e_2$ , which will produce quite distinct fringes.

#### 4.1.4. Complex exponentiated records

Conventional density input transparencies can be phased by one of several known bleaching processes. This bleaching changes the transparency from a light energy absorption device to one that changes the temporal phase of the light passing through it. The optical

transmission of the transparency may then be written as

$$t(x,y) = e^{jPD(x,y)} = e^{jPD(E)} \quad (4.11)$$

As before, when  $D \lesssim 1$ , the H - D curve can be closely approximated by

$$\begin{aligned} D(E) &= \alpha E^2 = \alpha E_0^2 (1 + e_1 \pm e_2)^2 \\ &= \alpha E_0^2 [1 + 2(e_1 \pm e_2) + (e_1 \pm e_2)^2] \end{aligned} \quad (4.12)$$

Substitution of  $D(E)$  into the phased transparency function gives

$$\begin{aligned} t(x,y) &= e^{jP} \alpha E_0^2 [1 + 2(e_1 \pm e_2) + (e_1 \pm e_2)^2] \\ &= e^{jP} \alpha E_0^2 e^{jP \alpha E_0^2 2(e_1 \pm e_2)} \\ &= e^{jP} \alpha E_0^2 (e_1 \pm E_2)^2 \end{aligned} \quad (4.13a)$$

Using the exponential expansion  $e^x = 1 + \sum_{n=1}^{\infty} x^n/n!$  on

the second and third terms gives

$$t(x,y) = e^{jP \propto E_0^2} \left[ 1 + \sum_{n=1}^{\infty} \left[ \frac{jP \propto E_0^2}{n!} 2(e_1 \pm e_2) \right]^n \right] \\ \cdot \left[ 1 + \sum_{n=1}^{\infty} (jP \propto E_0^2 (e_1 \pm e_2)^2)^n / n! \right] \quad (4.13b)$$

Now if  $(e_1 + e_2) < 1$  then  $(e_1 \pm e_2)^n / n! \ll 1$  and the higher order terms of  $(e_1 \pm e_2)^n$  are small. It is clear that the dominant term will be  $e_1 \pm e_2$  and where  $e_2(x,y) = e_1(x - x_0, y)$  it will produce distinct interference fringes in the Fourier Transform plane in the same manner as before.

When  $D \gtrsim 1$  we again approximate the H - D curve by

$$D(E) = \gamma' \ln E_0/k + \gamma' \ln (1 + e_1 \pm e_2) \quad (4.14)$$

Substitution of  $D(E)$  into the phased transparency function gives

$$t(x,y) = e^{jPD_0} e^{jP \gamma' \ln (1 + e_1 \pm e_2)} \quad (4.15)$$

Using the exponential expansion

$$e^x = 1 + \sum_{n=1}^{\infty} x^n/n!$$

$$\text{and } \ln(1+x) = x - x^2/2 + x^3/3 + \cdots (-1)^{n-1} x^n/n$$

we can write

$$t(x,y) = e^{jPD_0} \left[ 1 + \sum_{n=1}^{\infty} \frac{jP \delta' \ln(1 + e_1 \pm e_2)^n}{n!} \right] \quad (4.16a)$$

$$= e^{jPD_0} \left\{ 1 + \sum_{n=1}^{\infty} (jP \delta')^n/n! \left[ \sum_{m=1}^{\infty} (-1)^{m-1}/m \left[ e_1^m \pm e_1^{m-1} e_2 + \cdots + e_1 (\pm e_2)^{m-1} + (\pm e_2)^m \right] \right] \right\} \quad (4.16b)$$

Now if  $(e_1 \pm e_2) < 1$  then  $(e_1 \pm e_2)^n \ll 1$  and it is clear that the dominant term will be  $e_1 \pm e_2$ . When  $e_2(x,y) = e_1(x-x_0,y)$  it will produce distinct interference fringes in the Fourier Transform plane in the same manner as before.

The degree to which the neglected crossproduct terms will tend to wash out the fringes is not clear. To gain a better understanding of their effect, a computer simulation

was initiated. This is summarized in the next section.

#### 4.1.5. Computer model

The validity of the foregoing arguments was demonstrated by the development of a model and some computer generated spectrums. These spectrums indicate that distinct interference fringes are imposed on them by both the sum and difference exposures. Three separate but sequential programs were used to compute the Fourier Transform plane of exposure, density records, and complex exponentiated records for identical input signals. Digital computation permits making a better comparison between input record types.

The general H - D curve of Figure 4.2 was used for the development of the computer model. The upper straight line section of the H - D curve for the practical photographic emulsion can be accurately written as

$$D(E) = \gamma \log (E/k) = (\gamma / \ln 10) \ln (E/k), \quad E/k \geq E_b/k \quad (4.17)$$

where  $E_b/k$  is the break point in the curve. The section of the H - D curve to the left of the break point is quite accurately described by an amplitude transmission function,  $t$ , shown in Figure 4.3.

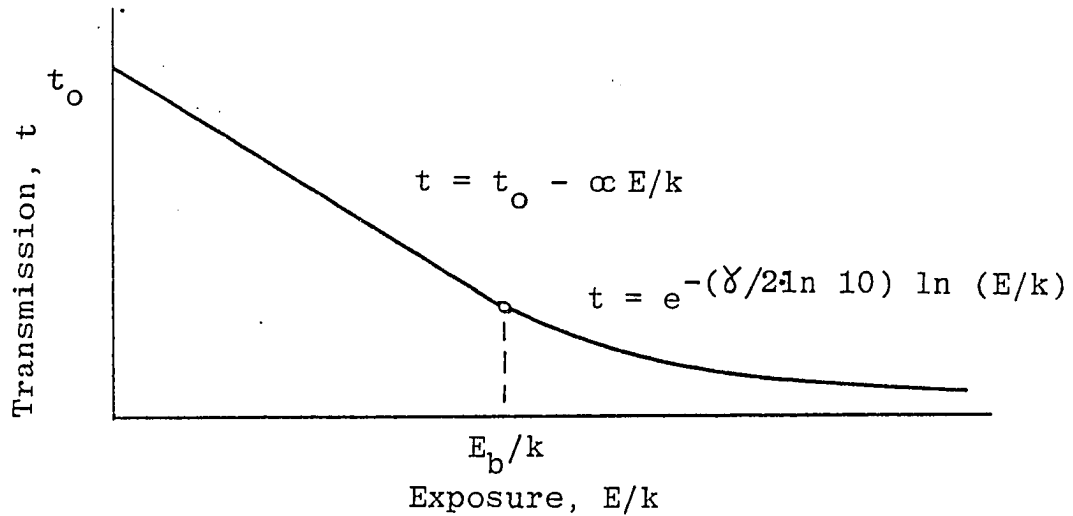


Figure 4.3. A typical amplitude transmission curve for a photographic emulsion

Experience also indicates that the amplitude transmission of practical photographic emulsions have a straight line section to the left of the break point as shown in Figure 4.3. The amplitude transmission function is also written as  $t = e^{-D/2}$  by the definition of optical density. Both the amplitude transmission curve and the H - D curve must be continuous with a continuous derivative with respect to exposure,  $E/k$ . Thus, at the break point,  $E_b/k$ , the two functions are equated as

$$\begin{aligned}
 t_0 - \alpha (E_b/k) &= e^{-(\gamma/\ln 100) \ln (E_b/k)} \\
 &= (E_b/k)^{-\gamma/\ln 100} \qquad (4.18)
 \end{aligned}$$

and the first derivatives are equated as

$$\alpha = \gamma / \ln 100 (E_b/k)^{-(\gamma + \ln 100) / \ln 100} \quad (4.19)$$

When  $\alpha$  is substituted back into the transmission equation we obtain

$$t_o - \gamma / \ln 100 (E_b/k)^{-\gamma / \ln 100} = (E_b/k)^{-\gamma / \ln 100}$$

or

$$\begin{aligned} E_b/k &= \left[ \left[ \frac{\gamma + \ln 100}{\ln 100} \right]^{-1} t_o \right]^{-\frac{\ln 100}{\gamma}} \\ &= \left[ t_o (\ln 100) / (\gamma + \ln 100) \right]^{-(\ln 100) / \gamma} \end{aligned} \quad (4.20)$$

To use this model, a value of  $\gamma$  and  $t_o$  are chosen for the photographic emulsion to be modeled. We next compute the break point exposure  $E_b/k$  and then the proportionality term  $\alpha$ .

The density,  $D$ , and transmission,  $t$ , can now be computed for a sequence of input exposure values  $E/k$ . If  $E/k \leq E_b/k$  the amplitude transmission can be evaluated as

$$t = t_o - \alpha (E/k) \quad (4.21)$$

and the optical density as

$$D = - \log t^2 \quad (4.22)$$

If  $E/k \geq E_b/k$  the optical density can be computed as

$$D = \gamma \log (E/k) \quad (4.23)$$

and the amplitude transmission as

$$t = e^{-D/2} \quad (4.24)$$

As an evaluation of the computer model, a family of H - D curves and amplitude transmission curves were generated. A practical value of amplitude transmission  $t_0$  is approximately unity. Typical values of the slope,  $\gamma$ , of the straight line segment of H - D curves vary from 1 to 8. Therefore, setting  $t_0 = 1$  an evaluation of values for  $E_b/k$ ,  $\alpha$ , and  $E/k$  required to achieve a certain optical density for various film  $\gamma$ 's can be obtained. Table 4.1 is a summary of these calculations.

Figure 4.4 and Figure 4.5 illustrate the amplitude transmission and H - D curves of this model for several different values of  $\gamma$ . These curves appear very much like

Table 4.1. Compilation of film characteristics

$\delta$	$E_D/K$	$\alpha$	D at $E_D/K$	E/K			
				at D = 2	D = 3	D = 4	D = 5
1	2.471836	0.072176	0.393020	100.0--	1000.--	$10^4$	$10^5$
2	2.294421	0.131969	0.721346	10.0--	31.62277	100.--	316.2277
3	2.159894	0.182633	1.003297	4.641589	10.--	21.54435	46.41589
4	2.053959	0.226313	1.250367	3.162278	5.623413	10.--	17.78279
5	1.968107	0.264494	1.470244	2.511886	3.981072	6.309573	10.--
6	1.896942	0.298249	1.668324	2.154435	3.162278	4.641589	6.812921
7	1.836866	0.328374	1.848542	1.930698	2.682696	3.727594	5.179475
8	1.785385	0.355475	2.013855	1.778279	2.371374	3.162278	4.216965

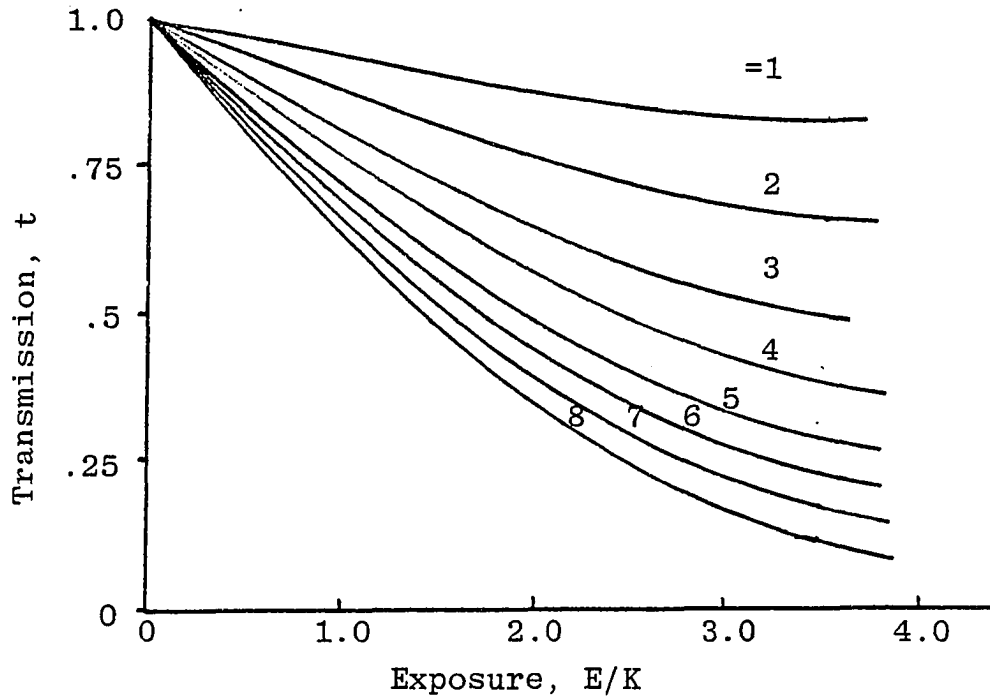


Figure 4.4. Amplitude Transmission curves for computer models

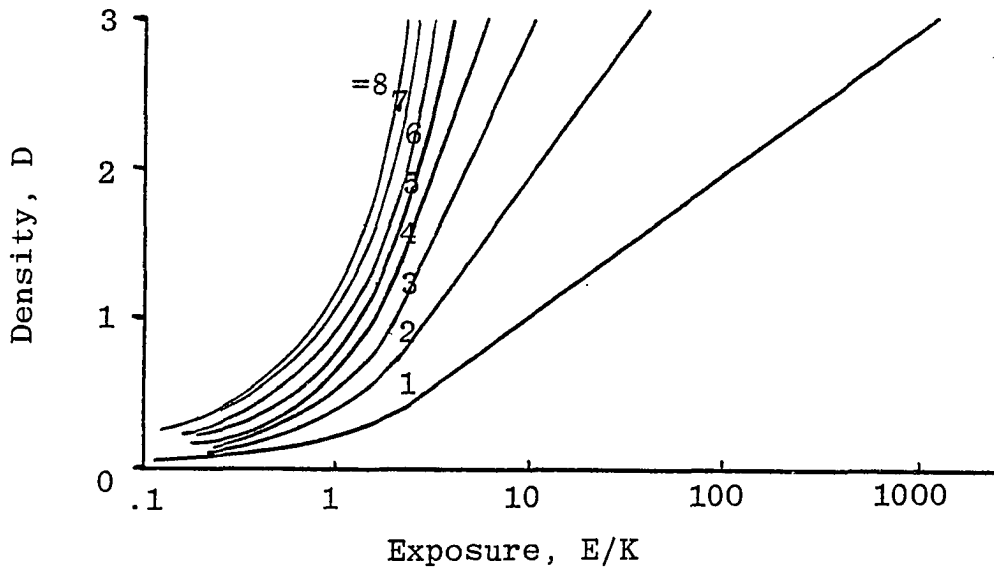


Figure 4.5. H - D curves for computer models

those measured for real emulsions. The computer calculated results were found to correspond in general with experimentally observed fringe patterns.

This hypothetical H - D curve can be used to compute the optical density and the related amplitude transmission at each position of the input plane, given the exposure at that position as described in the next section. For an absorption type photographic input, the amplitude transmission function given by equation (4.21) or (4.24) is used as the input for computing the Fourier Transform fringe pattern. For a phased type input the optical density function is used to compute a related phase function through use of Euler's relationship  $e^{jPD} = \cos PD (x,y) + j \sin PD(x,y)$ . This last process has been called complex exponentiation (9,15) and effectively describes the bleaching of a density input.

#### 4.1.6. Random signal generation

To utilize the computer model of the H - D curve for an investigation of fringe formation, a random bandlimited signal was computer generated to represent the one-dimensional exposure signal. The band limited random distribution of the exposure signal was obtained by SPLINE fitting a continuous curve to a sequence of points with randomly

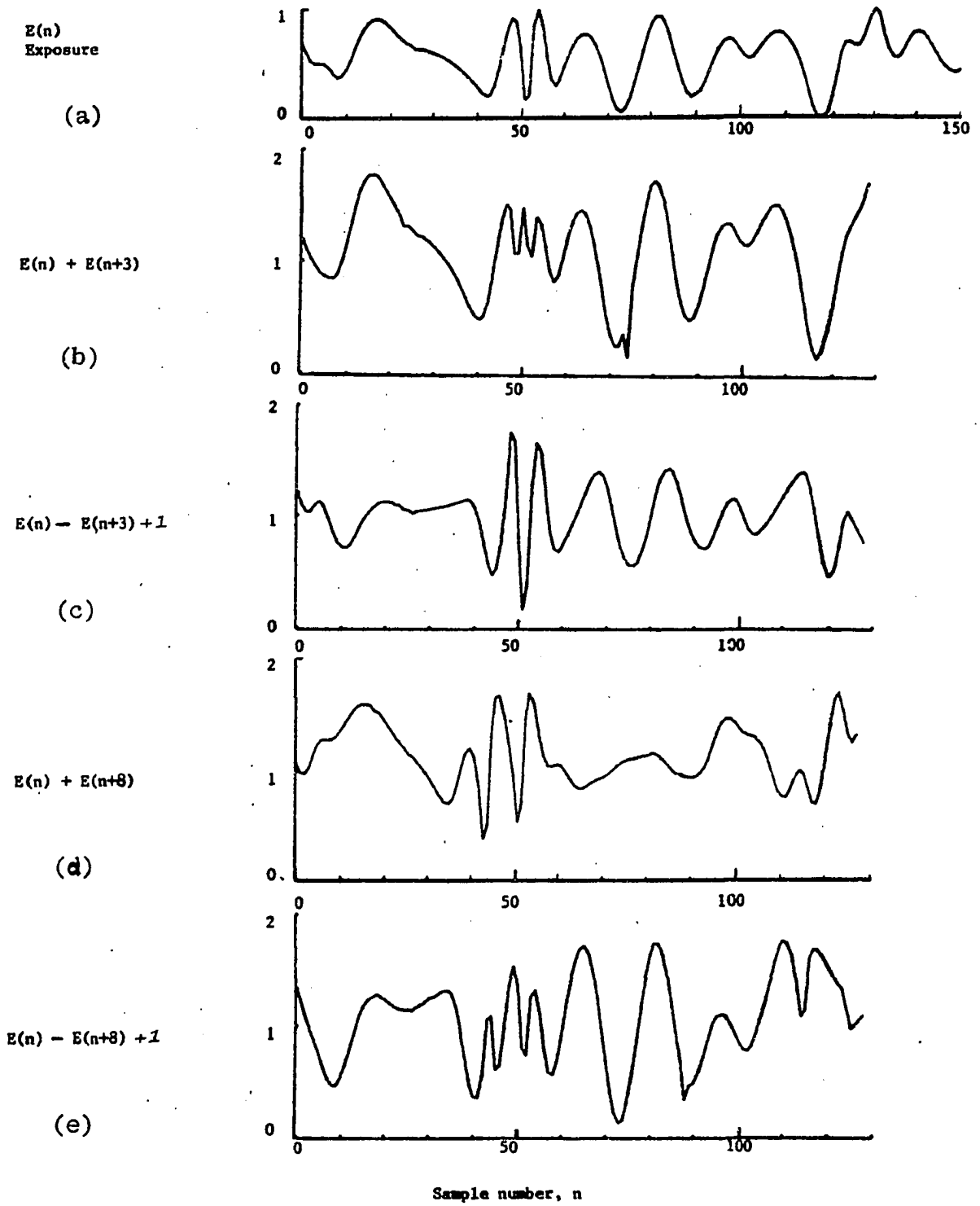


Figure 4.6. Random Signal  $E(n)$  and waveforms when shifted and added

chosen, uniformly distributed amplitudes and spacings. The SPLINE fit curve is band-limiting by requiring it to have continuous first and second order derivatives. The final smoothed curve was then sampled at equal spacings to form a digitized computer array of exposure for use in the computer model.

Figure 4.6a gives a continuous curve plot of the computed exposure function  $E(n)$  for the first 150 array subscripts,  $n$ . The other four curves of Figure 4.6 show the results of shifting an identical exposure curve by either 3 or 8 sample spaces and then adding or subtracting it from the original signal.

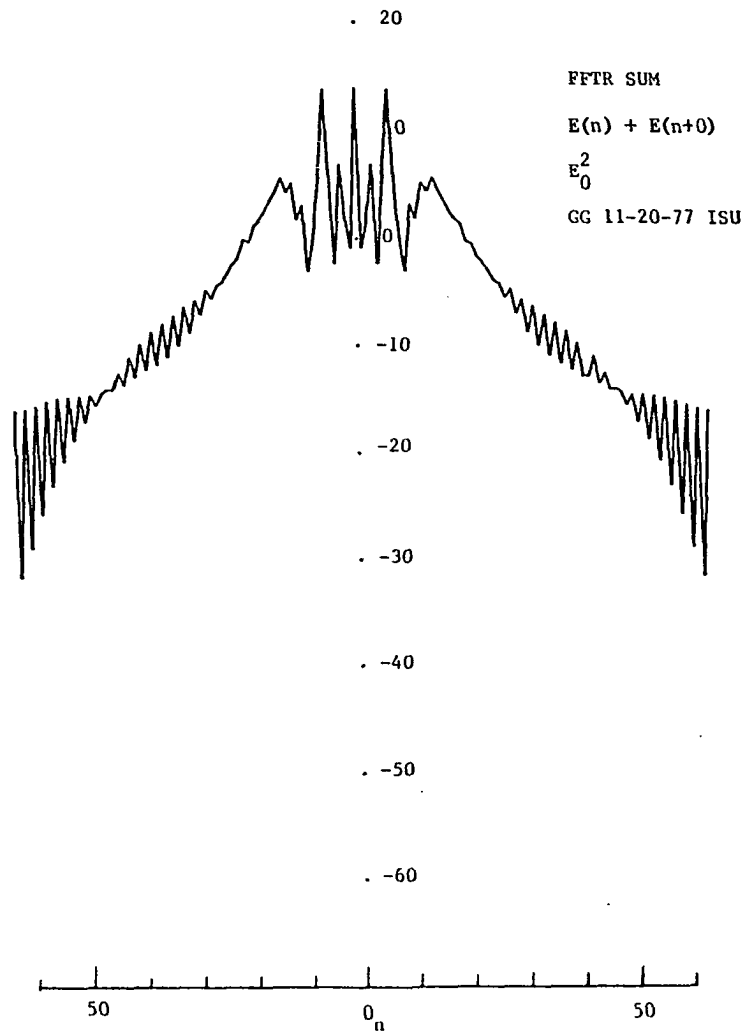
It is interesting to note that with only a small sample shift of 3 spaces there is a considerable change in the additive exposure's waveform. The author finds it extremely difficult to look at these shifted additive waveforms and discern the original waveform and its shift. This is more understandable when one recalls that adding random waveforms gives another random waveform.

#### 4.1.7. Results

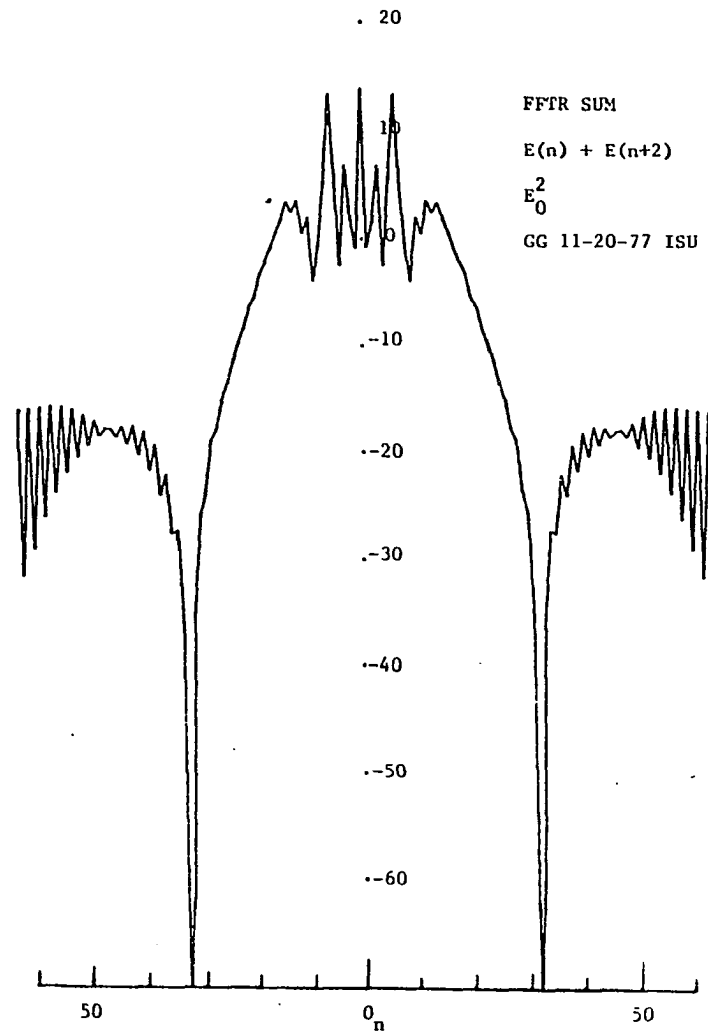
This section summarizes the output of an extensive set of calculations made on a digital computer. Through the use of the computer model and its quantitative numerical

data, an analysis of specific system parameters was performed. This allowed for a better comparison of data between calculations than was available from experimental results given in a later section. In that section the reader will find documentation of experimental verification of much of the computer results. The rest of this section is a discussion of the many specific observations made which are further exemplified by the graphs of the computer output.

To aid the reader in quickly understanding the graphs, an explanation of the common nomenclature and of the units is given. First, all of the graphs are cross-sectional plots of the computed Fourier Transform plane of the input data. The ordinate units are in logarithmic intensity,  $db = \log I$ , and the abscissa units are sample number,  $n$ . The symbols FFTR and FFTP represent Fast Fourier Transform programs (FFT) for real (FFTR) and complex (FFTP) input data.  $E(n) + E(n + m)$  represents the addition of original exposure signals at sample number  $n$  with a shift of  $m$ . The minimum and maximum limits of exposure signals are indicated by subscripts and superscripts on  $E$ . If exposure was converted to density, the limits of the density ( $D$ ) range are similarly given and means that the input data was converted to density values by a  $H - D$  curve with  $\gamma = 3$

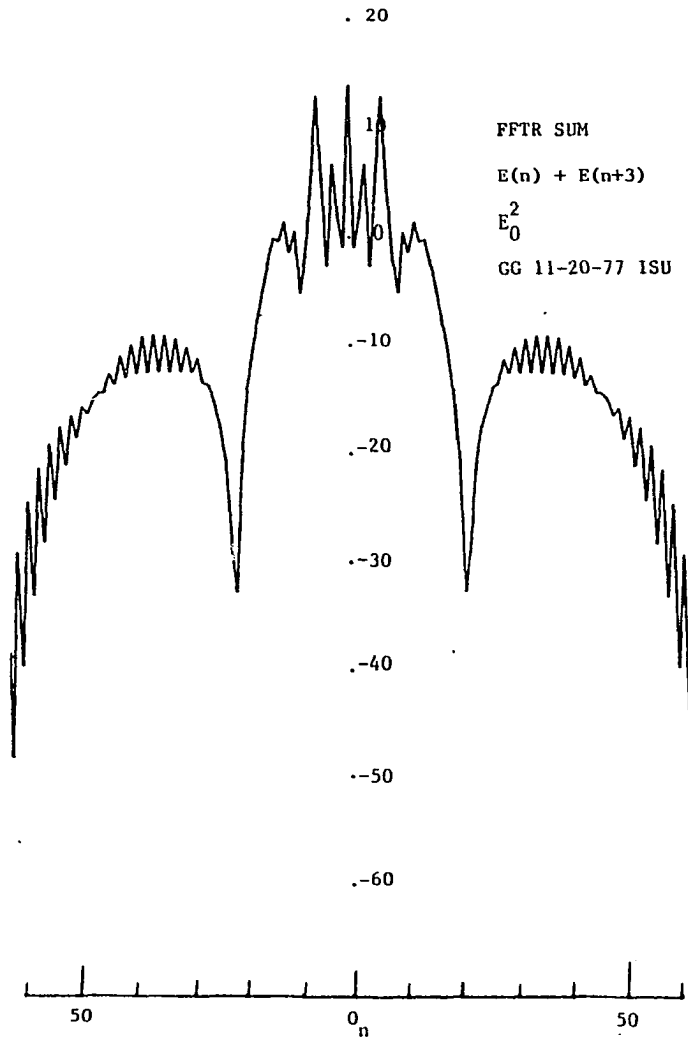


(a)

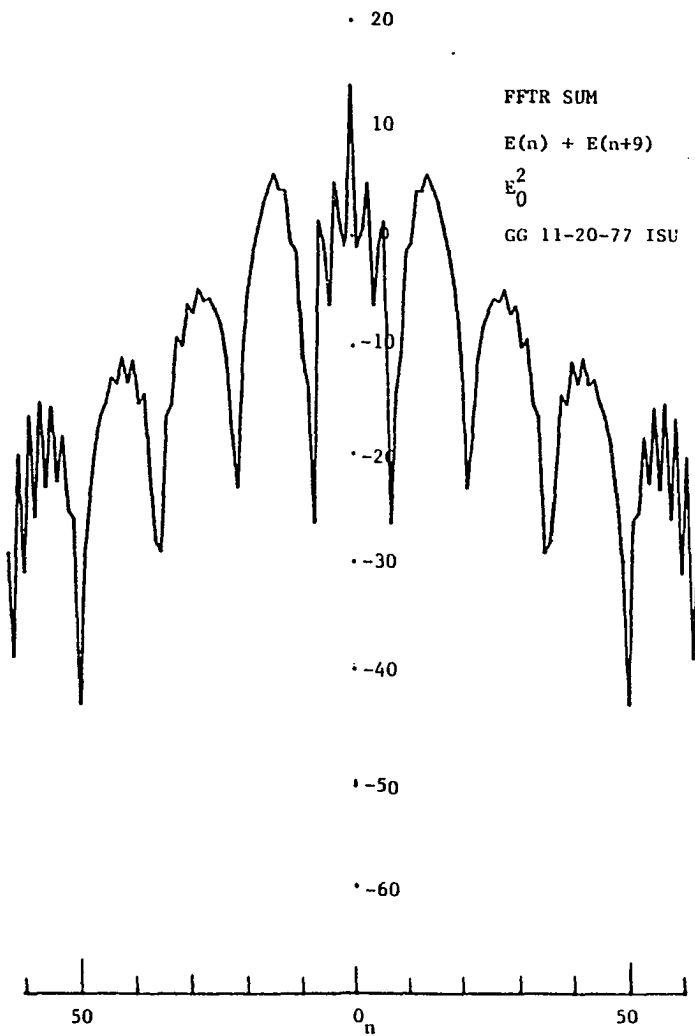


(b)

Figure 4.7. The Fourier Transforms of multiple exposure signals for shifts of (a) zero and (b) 2 of 128 sample numbers



(a)



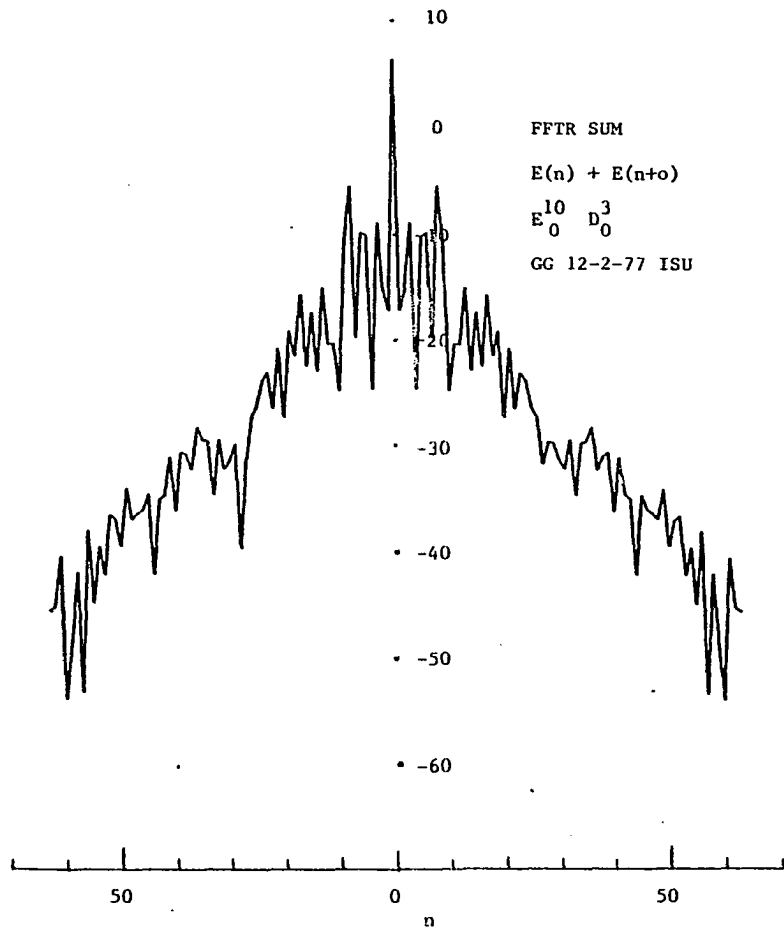
(b)

Figure 4.8. The Fourier Transforms of multiple exposure signals for shifts of  
(a) 3 of 128 and (b) 9 of 128 sample numbers

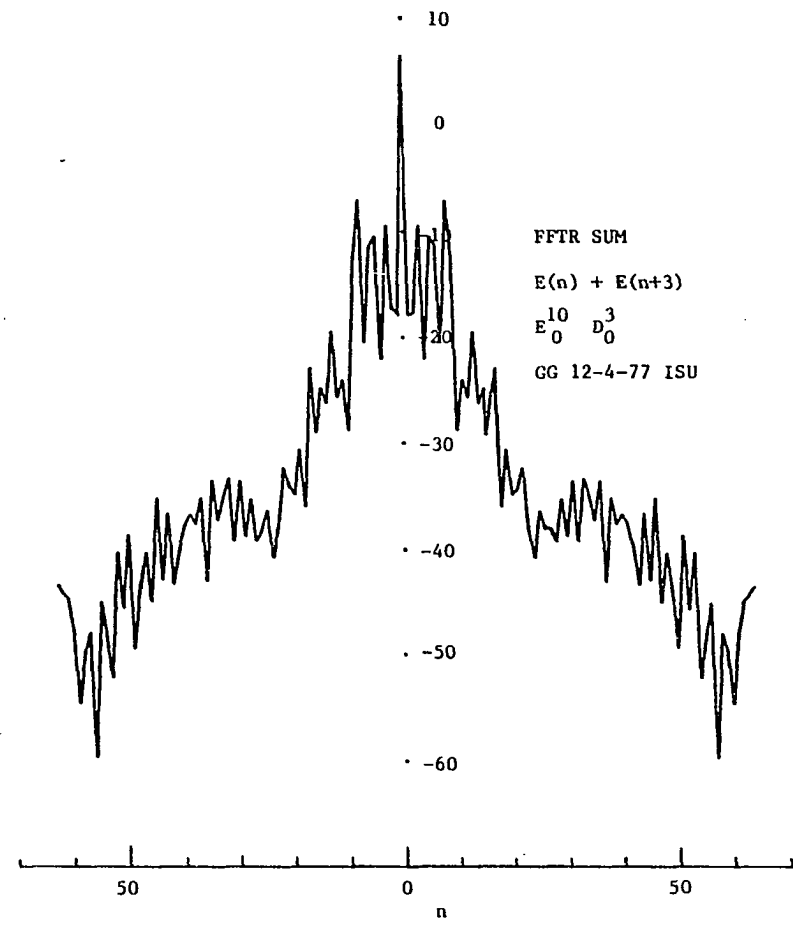
and  $t_0 = 1$ . Finally, complex exponentiation of the input density data is indicated by  $PEX \cdot D$  with its limits similarly given, but units are in radians.

Figures 4.7 and 4.8 show the development of the fringe patterns and their inverse relationship to the amount of shift between the two input exposure signals. The distance between fringe nulls is the reciprocal of the percent of shift in the digital window, or 128 divided by the shift value  $m$ . The sharpness of the nulls was caused by the plotting of the spectrum intensity instead of the amplitude and the use of a logarithmic ordinate. The logarithmic ordinate allows the fringe patterns to be seen at higher order harmonics than a linear ordinate plot allows. A linear ordinate suppresses any fringe pattern at higher-order harmonics and makes the entire spectrum appear like a Dirac delta function at the origin.

For reference purposes, Figure 4.7a shows the spectrum of the two added exposure signals with no shift. Note the higher-order harmonics are -20 to -30 dB below the low-order harmonics. Figure 4.7b shows a null for a shift of 2 of 128 samples. Because of its reciprocal nature and numerical limitations, this is the smallest shift capable of giving a positive indication of nulls. The deep nulls of Figure 4.7b are believed to be a consequence of the

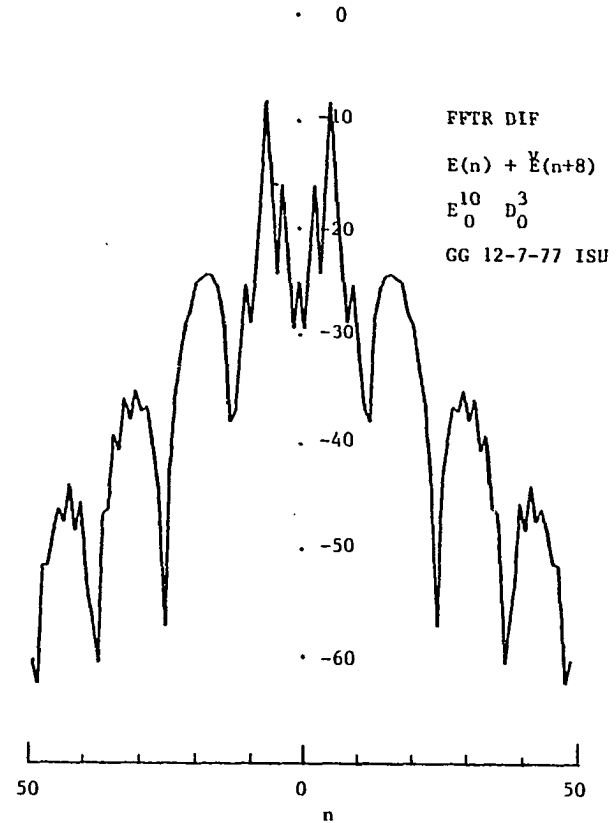
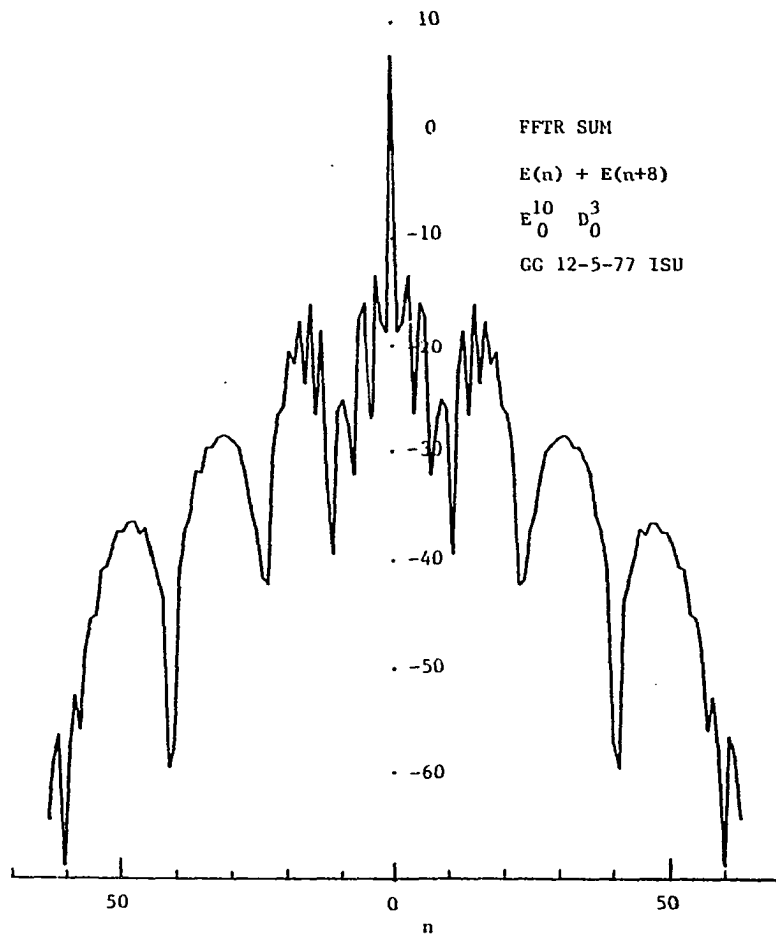


(a)



(b)

Figure 4.9. The Fourier Transforms of multiple exposure density inputs with shifts of (a) zero and (b) 3 of 128 sample numbers

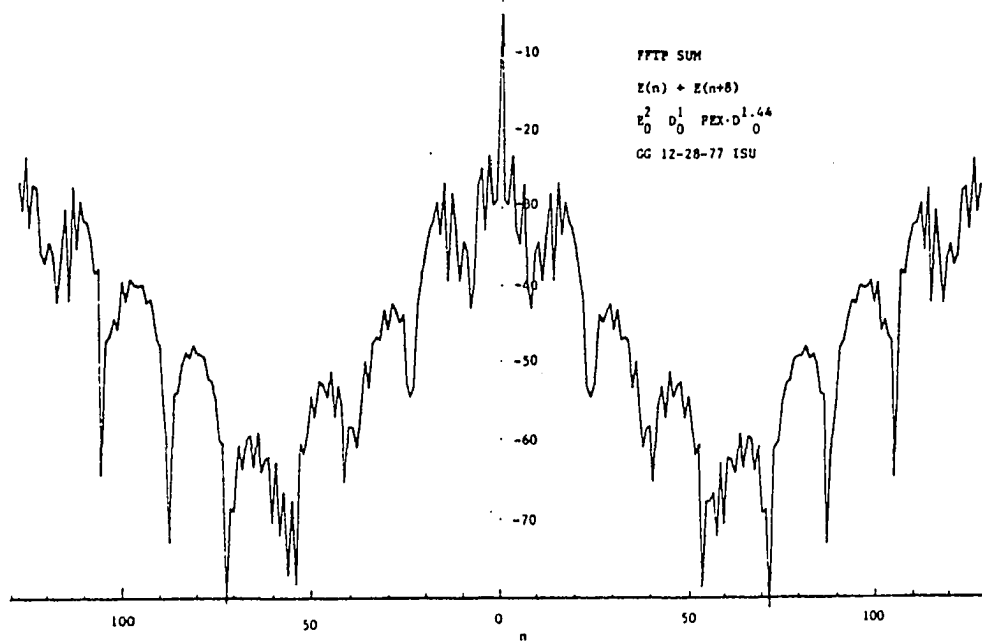


(a) (b)  
 Figure 4.10. The Fourier Transforms of multiple exposure density inputs with shifts 8 of 128 sample numbers. Inputs are additive in (a) and difference in (b)

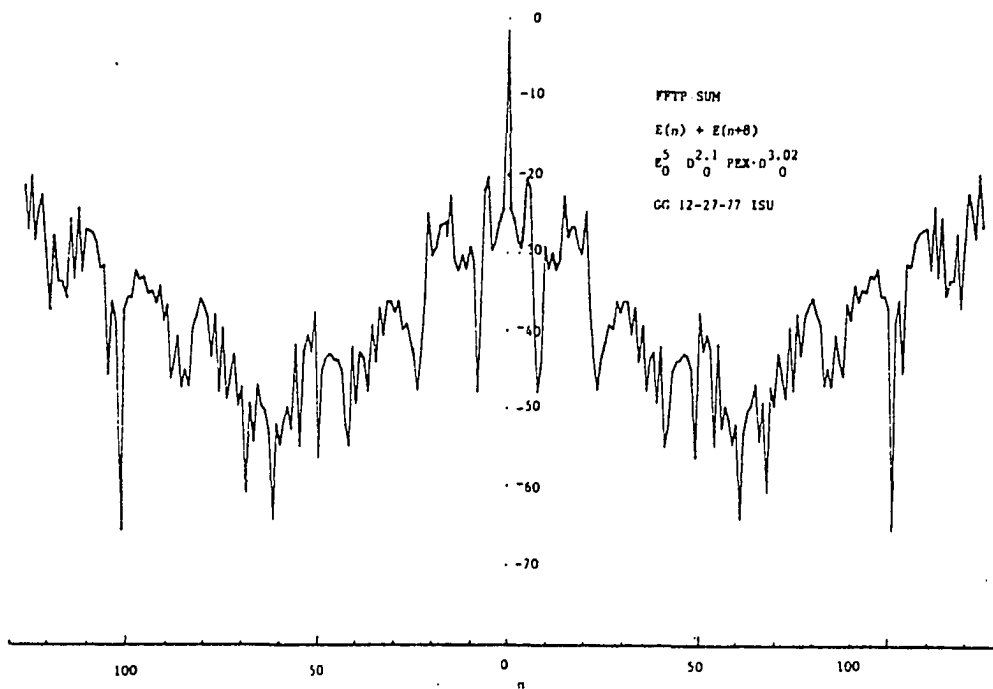
computational procedure. Figures 4.8a and 4.8b show fringes for signal shifts of 3 and 9 sample spaces respectively. Even though the higher harmonics are less intense, the fringes show up distinctly.

Figures 4.9 and 4.10 show the development of the fringe patterns for inputs of the same exposure signals converted to a photographic absorption type input using the H - D model previously discussed with  $\gamma = 3$  and  $t_0 = 1$ . Note the general reduction in harmonic signal intensity of the plotted spectrums from the original exposure spectrums of Figures 4.7a and 4.8a. This decrease is typical of an optical absorption input. Figure 4.9b shows that a low shift value such as 3 of 128 is barely discernible. Figure 4.10a is for a sum input and Figure 4.10b is for a difference input with an 8 of 128 shift. The difference input signal spectrum verifies the null at  $n = 0$  developed in section 4.1.2. and shown in Figure 4.1b. Again note the large roll off of higher order harmonics.

Figures 4.11 and 4.12 show fringe patterns for input exposures converted to density records and then complex exponentiated. The major effect to note is the increase in the magnitude of the higher order harmonics. The original signal's spectrum has been increased and broadened. This result is hereafter referred to as signal spectrum whitening.

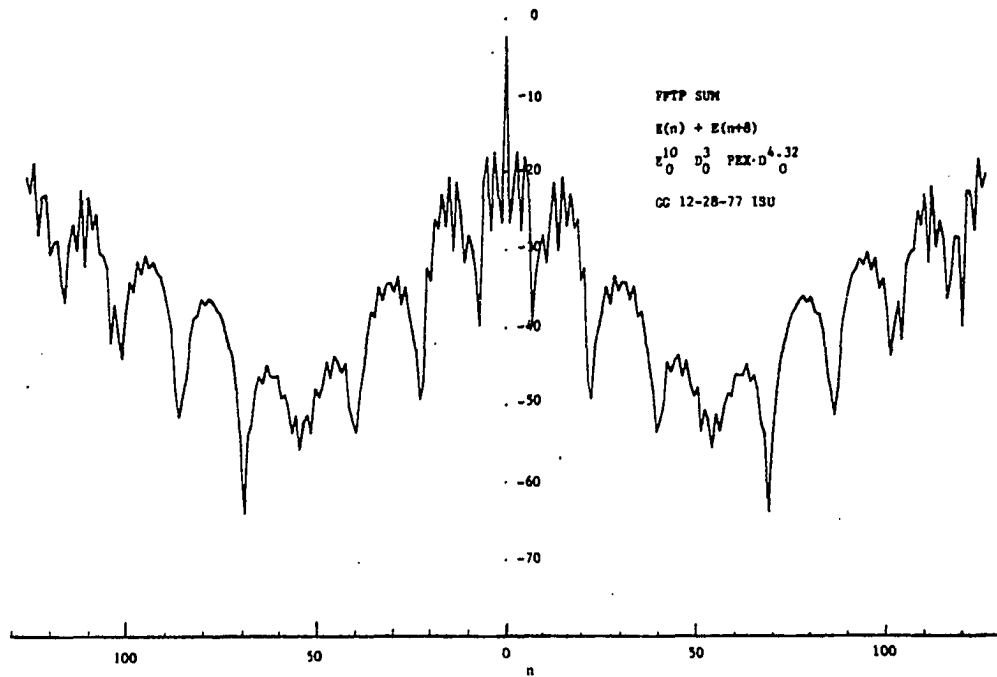


(a)

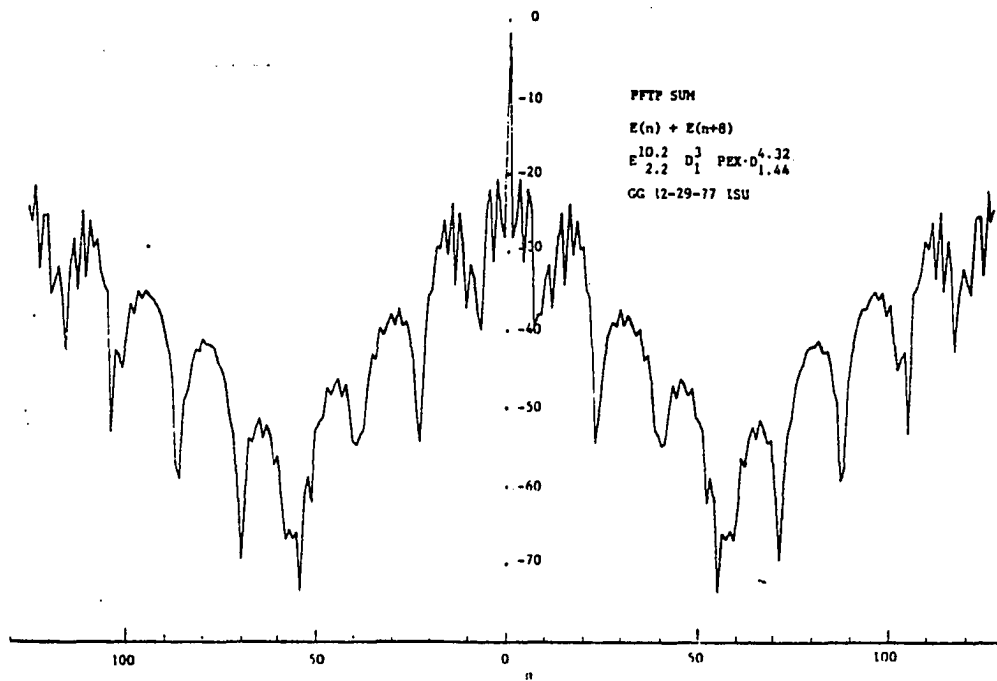


(b)

Figure 4.11. The Fourier Transform of multiple records shifted 8 of 128 sample numbers with different signal input levels phased



(a)

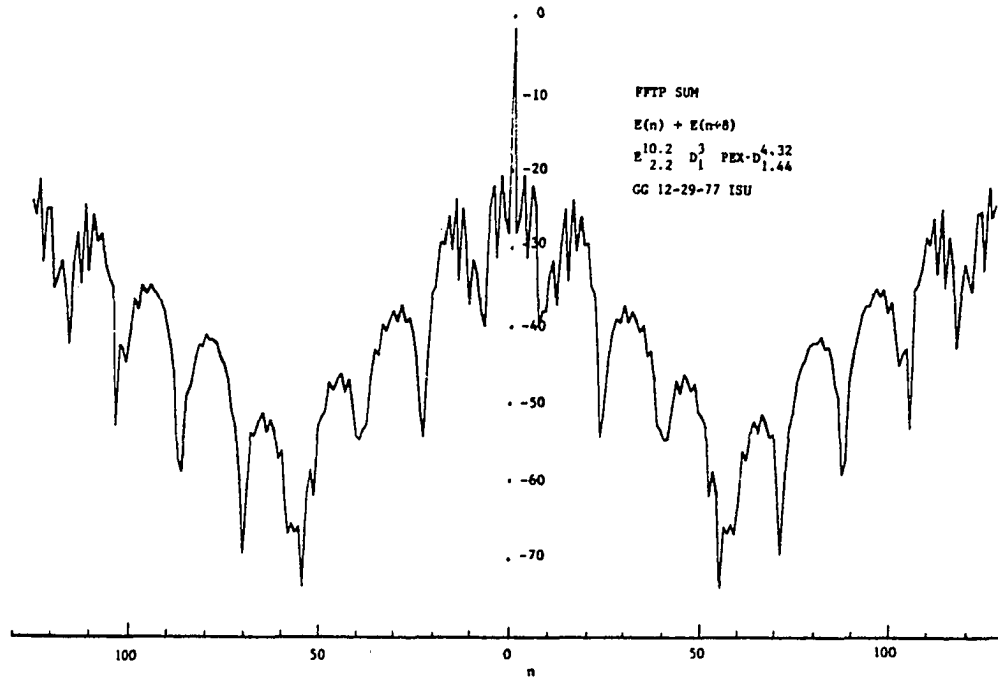


(b)

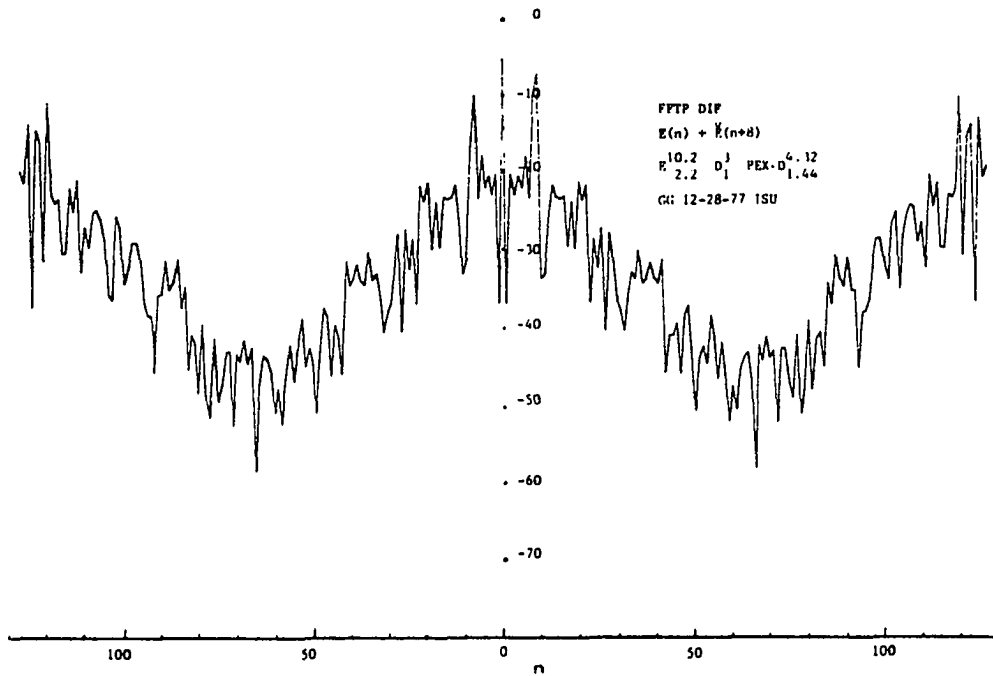
Figure 4.12. The Fourier Transform of multiple records shifted 8 of 128 sample numbers with different signal levels phased

The objective of these four iterations of the same shifted signal is to determine the smoothest most distinct fringe pattern curve. The input signal's bias and peak-to-peak value are changed so as to use different sections of the H - D curve and various magnitude ranges of  $PEX \cdot D$ . The author believes the best curve to determine the signal shift is that of Figure 4.12b. The exposure signal was biased to be in the linear section of the H - D curve and the signal amplitude was adjusted to give an optimal  $PEX \cdot D$  range of  $\pi$  radians. This confirms the results Göpfert (9, 15) obtained in his research on correlation of complex exponentiated signals. The signal of Figure 4.11b also has a  $PEX \cdot D$  range of  $\pi$  but exposure-to-density conversion occurs across the break point in both sections of the H - D curve. The nonlinearity of this exposure process greatly diminishes the fringe pattern formation.

A comparison between additive and difference input signals is shown in Figures 4.13 and 4.14. For the same input signal, a shift of 8 or 9 of 128 sample numbers, the additive signal processing gives a distinctly smoother fringe pattern curve. The exact cause of the noisy spectrum fringe patterns for the difference process is unknown, but it should be related to the odd-order difference signals' nulls discussed before. It should be noted here that

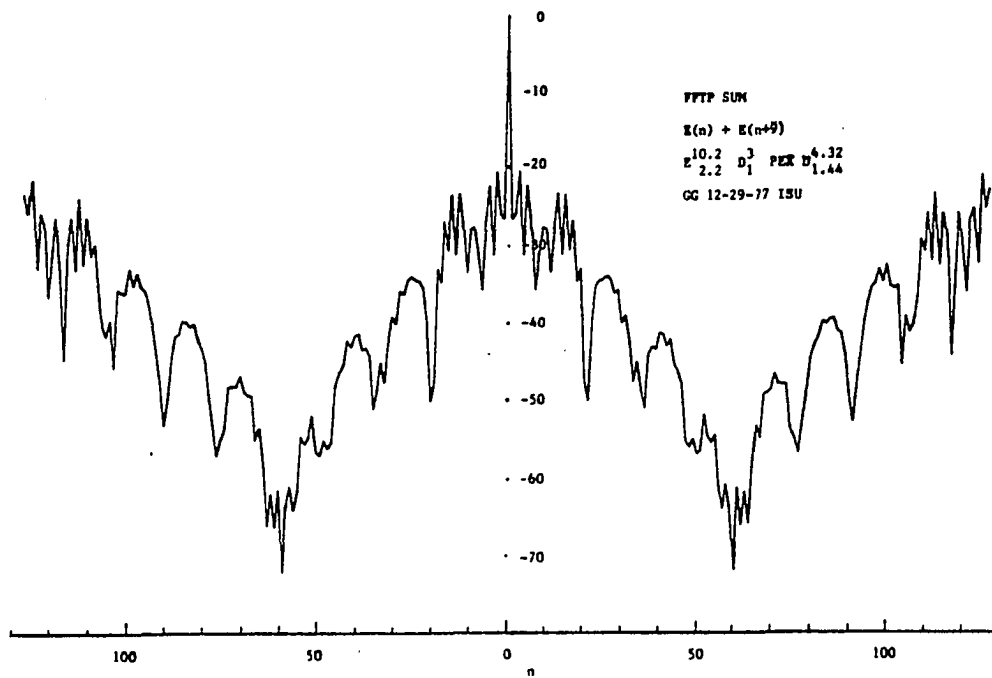


(a)

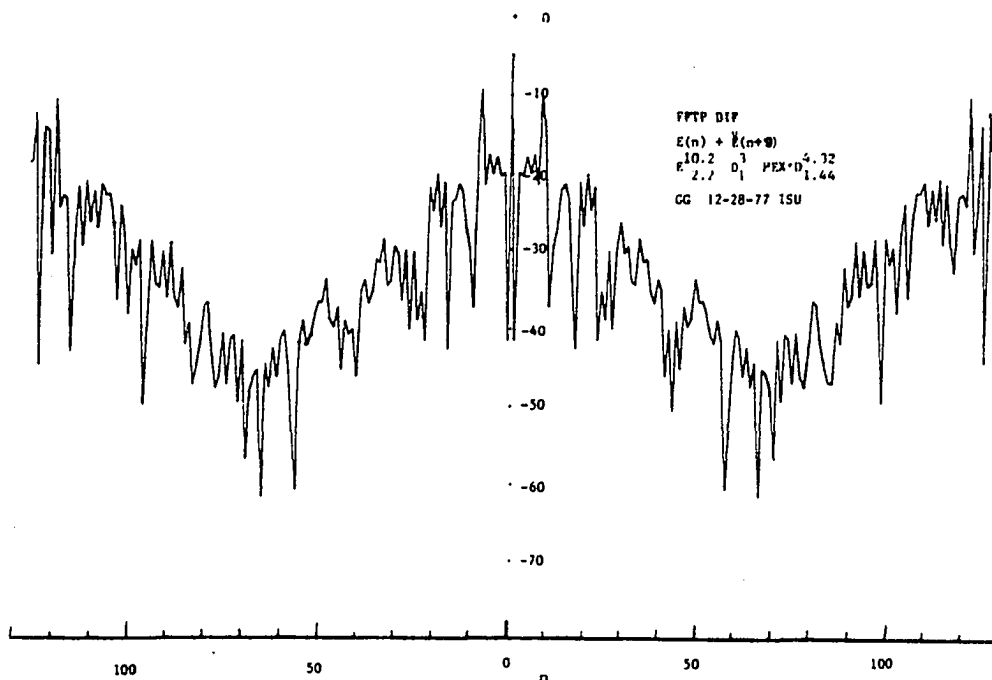


(b)

Figure 4.13. Fourier Transform of multiple phased records shifted 8 of 128 sample numbers showing spectra for (a) additive and (b) inverted inputs



(a)



(b)

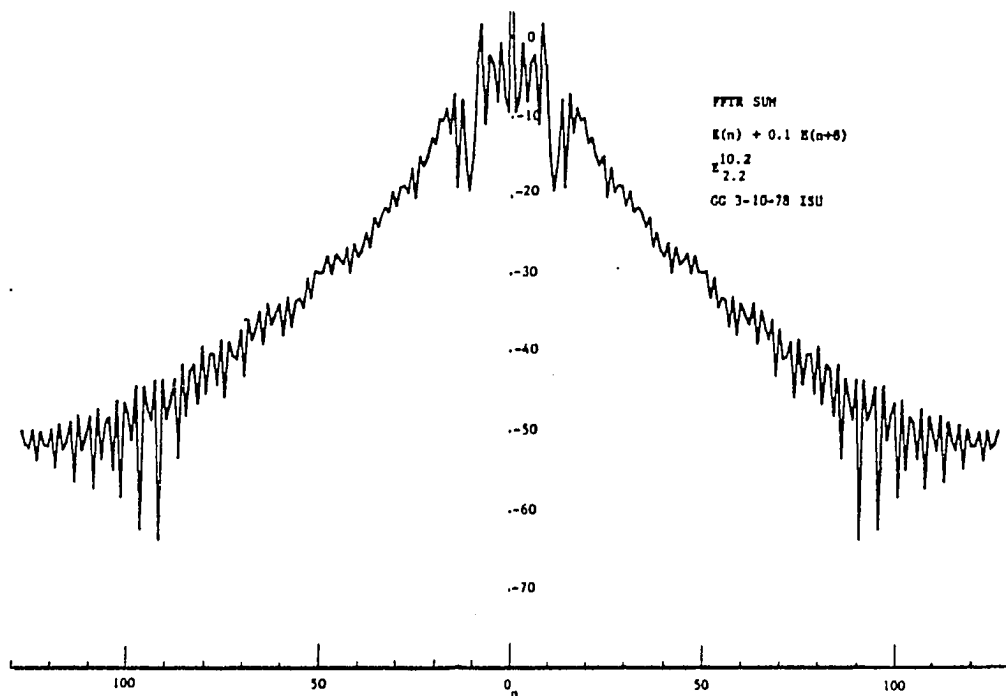
Figure 4.14. Fourier Transform of multiple phased records shifted 9 of 128 sample numbers showing spectra for (a) additive and (b) inverted inputs

difference type photographic inputs have experimentally produced less distinct fringes than summation type inputs. It thus appears that the observation made here is not a consequence of the particular set of random numbers used to simulate the process.

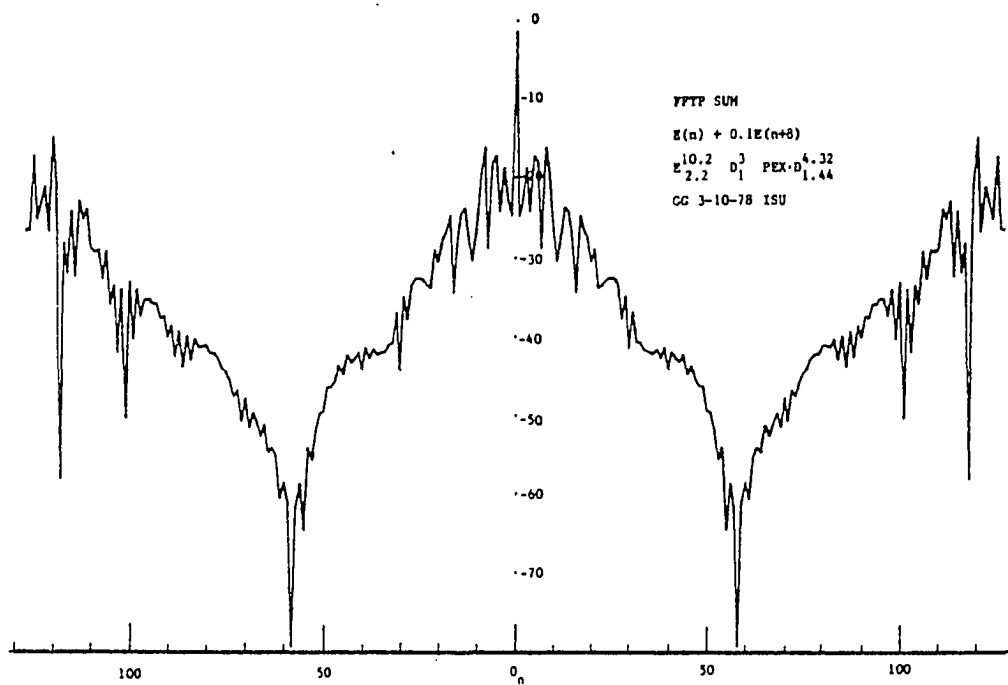
The fact that the additive (+) signals produced the better fringe pattern is an advantage since it is usually far easier to superimpose two additive exposures than their differences.

A study of the effect of various input signal ratios is shown in Figure 4.15. This set of spectrum plots shows that fringe patterns of shifted inputs signals with signals ratios of 10 to 1 are discernible by the complex exponentiation process. This appears to be about the limiting ratio and could easily be obtained by photographic or electronic preprocessing of input signals.

If we refer back to the spectrum of Figure 4.7a again, we will note that a linear ordinate would produce a plot that looks much like a Dirac delta function at the spectrum center with very small harmonic intensities. This type of plot would greatly suppress all fringe pattern information. A Fourier Transform made of this linear ordinate spectrum would give a transform dominated by a uniformly distributed "white" spectrum resulting from the Dirac delta spike at its



(a)



(b)

Figure 4.15. Fourier Transform of multiple inputs shifted 8 of 128 sample numbers. Inputs of a 10 to 1 ratio show fringes with complex exponentiated inputs (b) but are not discernible in the original additive exposure signals (a)

center. All frequencies of this new spectrum would be nearly the same in intensity and no information about the original shifted signal would be discernible. However, if the first Fourier Transform spectrum intensity is plotted with a logarithmic ordinate, the higher order frequencies and the fringe pattern are emphasized as illustrated in the preceding figures. If this logarithmic intensity spectrum was again Fourier Transformed, the new spectrum intensity plot would have two distinct nonzero peaks. The position of this peak would be an exact measure of the shift in the original signals. Since the original signal intensity spectrum was real and symmetrical only the right half is given in Figure 4.16 of such a spectrum plot and the spike appears at the eighth sample position.

This double Fourier Transform procedure was tried on two additive signals with a single shift and various amplitude ratios. Excellent results were obtained for signal ratios of 10 to 1 and less. The procedure did not appear to work well on multiply shifted input signals. The procedure was easily implemented on a digital computer, but optical implementation would require an optical device with a logarithmic intensity transfer function in the first Fourier Transform plane. The simplest such device is a photographic film but it requires conventional developing

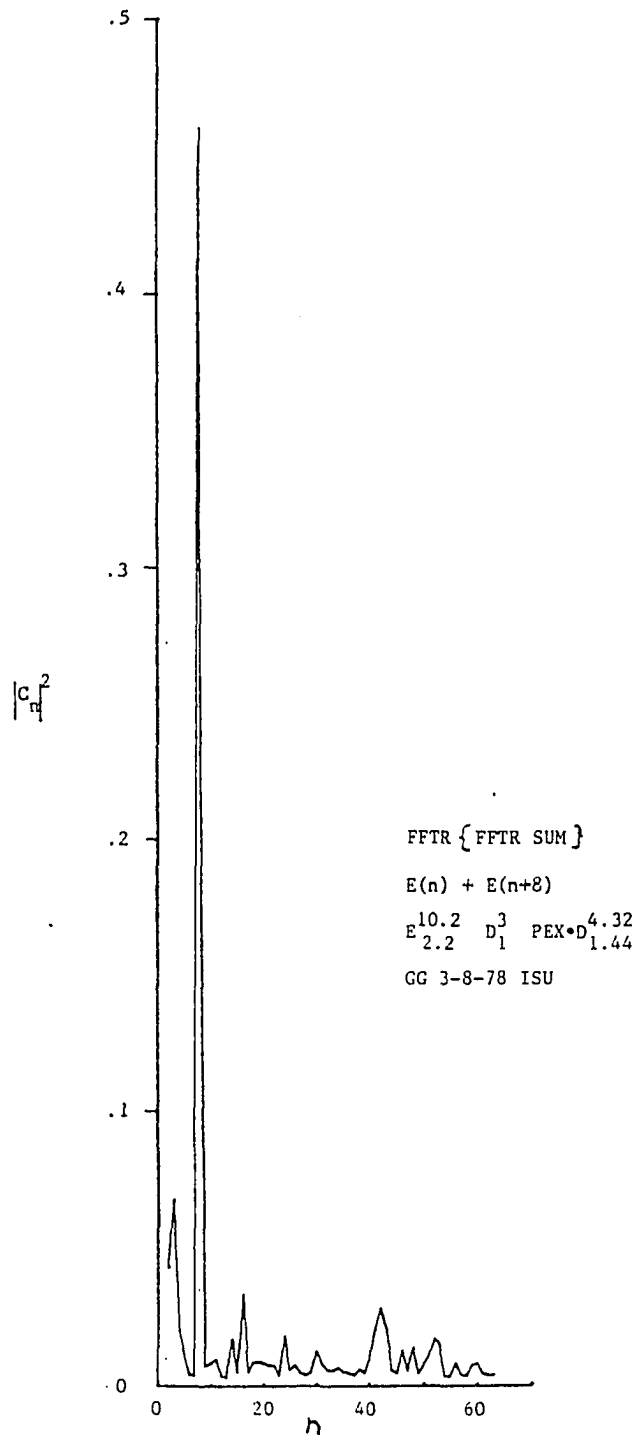


Figure 4.16. The Fourier Transform of a logarithmic intensity plot of the Fourier transform of complex exponentiated shifted input signals

and is not a real-time device. Digital applications of the procedure might be found in processing sound or electronic signals of one-dimension with a single shift.

#### 4.1.8. Cascaded records

The results of the computer simulation suggest that a means of obtaining an adjustable shift between the input signals would be advantageous. It is well-known that for cascaded input transparencies the total amplitude transmission function is the product of the individual transparencies' amplitude transmission functions. Recalling that the individual amplitude transmission as a function of density was expressed by Equation (4.24) as  $t = e^{-D/2}$ . The total amplitude transmission for two cascaded input transparencies can then be written as

$$\begin{aligned} t_T(x,y) &= t_1(x,y) t_2(x,y) \\ &= e^{-D_1(x,y)/2} e^{-D_2(x,y)/2} \\ &= e^{-(D_1 + D_2)/2} \end{aligned}$$

If  $D_2(x,y) = D_1(x - x_0, y)$  and  $D_2$  can be either positive

or negative (+), it is clear that the total amplitude transmission for the two cascaded density records is essentially the same as a double exposure on one density type record.

For the phased input records the amplitude transmission was given by Equation 4.11 as

$$t_T(x,y) = e^{jPD(x,y)} \quad (4.11)$$

and the same arguments hold. It was with these results in mind that the records used in the later experimental realization were made on separate records and cascaded.

#### 4.1.9. Conclusions

The previous sections show that a shift between two similar signals is detectable as a fringe pattern on the Fourier Transfer spectrum of the composite signal. The fringe pattern null spacing is inversely related to the shift between the two signals. The sum of two shifted inputs signals gives a much better fringe pattern than the difference of those signals. The use of spectrum graphs with ordinate plots of logarithmic intensity increases the visibility of the fringe patterns.

The complex exponentiation of the input signals

increases the magnitude and broadens the harmonic components of the spectrum. It also provides greater fringe pattern visibility than absorption type input records. Both records require some preprocessing but are readily realizable. Direct exposure signals have yet to be processed.

The use of logarithmic intensity plots of the first Fourier Transform spectrum allows the application of a second Fourier Transform to determine the amount of shift between inputs signals. This procedure works extremely well for singularly shifted inputs with various signal amplitude ratios. It provides a very distinct spike whose position in the computed spectrum directly indicates the amount of shift between the two original signals.

## 4.2. Experimental Realization

### 4.2.1. Introduction

The experimental realization of the processing of the one-dimensional records used in this section was done with the optical data processing system developed and delineated in Chapter 5 on two-dimensional records. Only a simple schematic representation of the system will be given here. In figure 4.17, the basic system components are the input plane, the transforming lens  $L_1$ , the output frequency plane, and a second lens  $L_2$  that provides a magnified image of the

frequency plane. This magnified image was used to record the spectrum graphs while the photographs are properly enlarged photos made from true size negatives made at the frequency plane.

The system uses a coherent parallel laser beam of light with a diameter that is adjustable from about 0.5 to 1.5 mm. The beam impinges on the input plane records which spacially modulates the light rays. The transform lens gathers these diffracted rays and displays on the frequency plane a Fourier Transform of the amplitude transmittance of the input record. A more detailed description of the Fourier Transforming process is given in the Appendix. It is sufficient here to repeat briefly the two-dimension Fourier Transform relationship. An input transparency with amplitude transmittance function  $g(x_o, y_o)$  in Figure 4.17 has its Fourier Transform formed on the output frequency plane according to the relationship

$$\underline{G}(f_x, f_y) = k \exp\left(\frac{j\pi}{\lambda F}\right) \left(1 - \frac{D}{F}\right) (x_f^2 + y_f^2) F_o g(x_o, y_o) \quad (4.25)$$

where  $x_f = \lambda F f_x$  and  $y_f = \lambda F f_y$  relate the spacial frequency in the  $x_o$ - $y_o$  plane to the position in the  $x_f$ - $y_f$  plane.

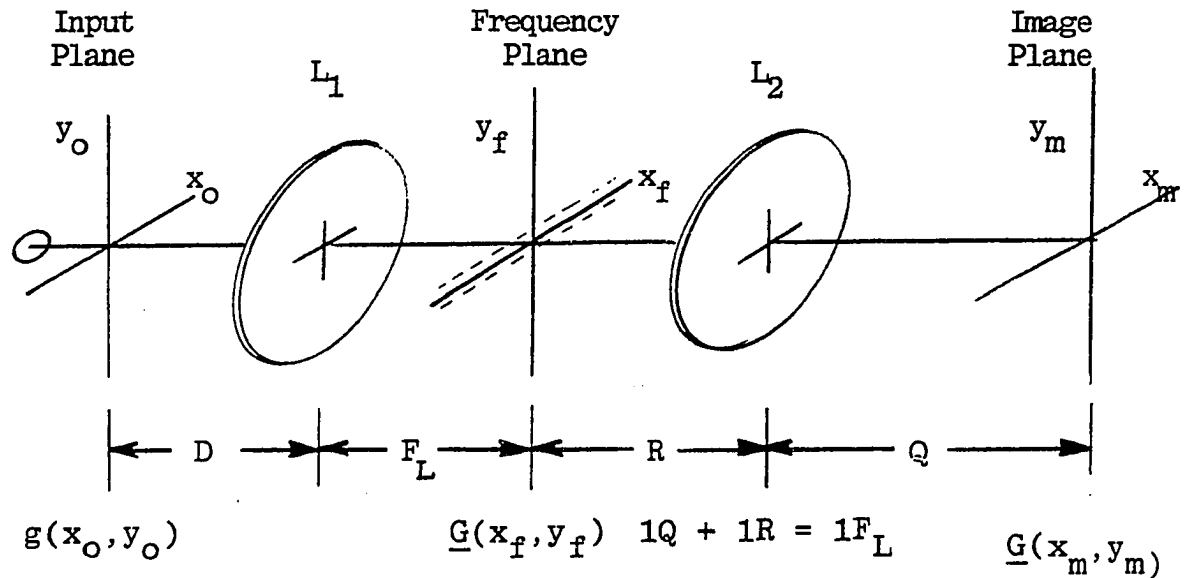


Figure 4.17. A schematic diagram of an optical Fourier Transforming device.

For one-dimensional input signals the Fourier Transform will be written as

$$\underline{G}(f_x, f_y) = \underline{G}(f_x) \delta(f_y) \quad (4.26)$$

where the  $\delta(f_y)$  represents the narrow strip (in the  $y_f$ -direction) along and centered on the  $x_f$ -axis. For  $D = F$  the phase factor is zero and a true Fourier Transform with measurable intensity is displayed in the frequency plane as

$$I(x_f, y_f) = \underline{G}(x_f, ) \underline{G}(x_f, )^* \delta(y_f)^2 \quad (4.27)$$

This is the intensity spectrum that is magnified onto the  $x_m$ - $y_m$  plane, where it was measured and recorded with a photo-optic light sensor of the Bell & Howell type 529, a logarithmic amplifier and an x-y recorder.

#### 4.2.2. Calibration

Once the physical system was constructed, it was necessary to verify calculated and observed spectral relations. If the lenses have a focal length  $F_L = 193$  mm and the light wavelength  $\lambda = 0.6328 \mu\text{m}$ , then an input spacial frequency  $f_x$  in the  $x_o$ -direction will cause a displacement

$$\begin{aligned} x_f &= \lambda F f_x \\ &= 0.6328 \times 10^{-6} \cdot 193 \times 10^{-3} \cdot f_x \\ &= 0.12213 \cdot f_x \text{ mm} \end{aligned} \tag{4.28}$$

when  $f_x$  is given in lines/mm. The graphs were plotted from the magnified image of the frequency plane. With  $Q = 842$  mm and  $R = 254$  mm, a magnification factor  $m = Q/R = 843/253 = 3.33$  was calculated. This magnified frequency plane will therefore have an  $x_m = 0.4067 \cdot f_x$  mm.

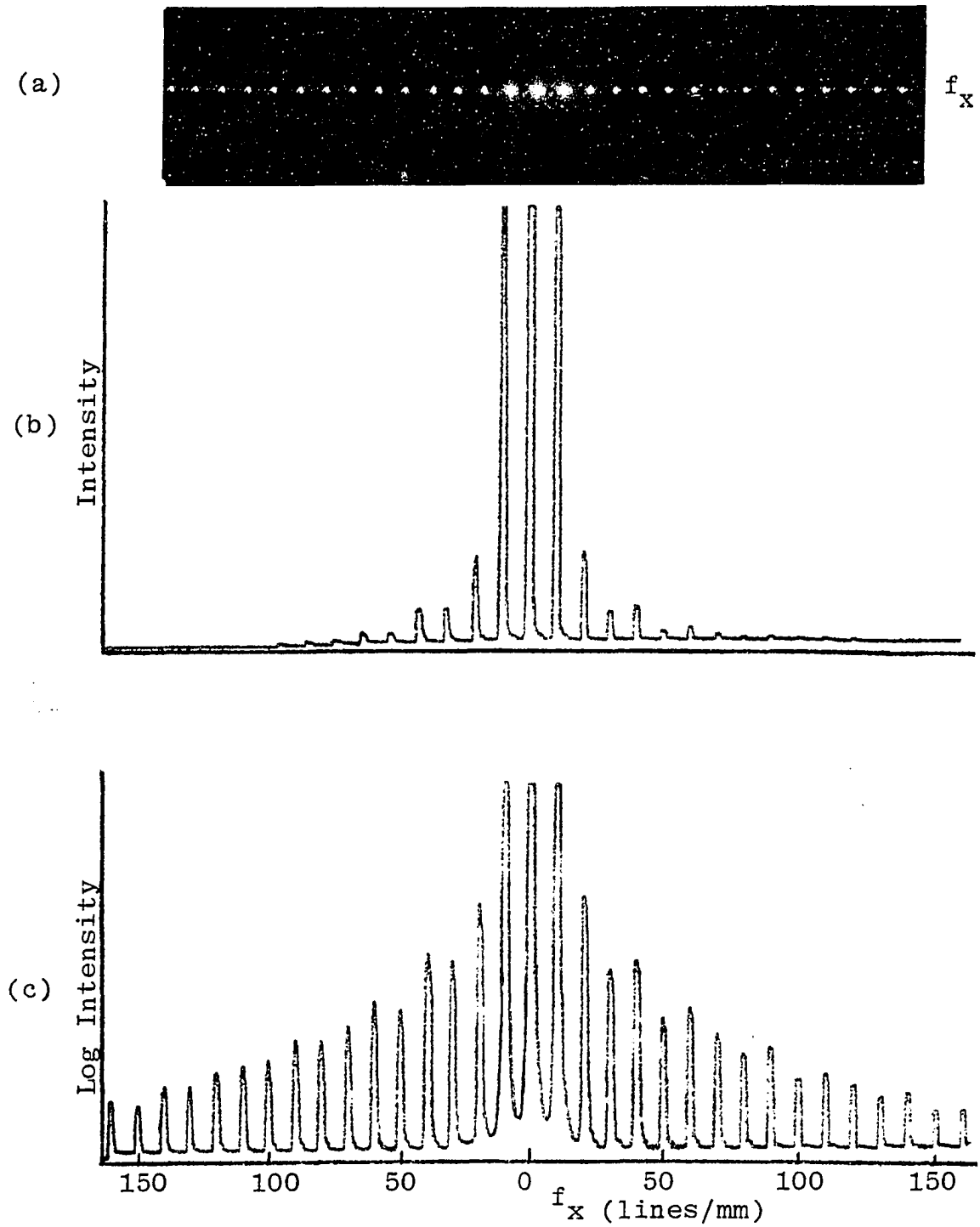


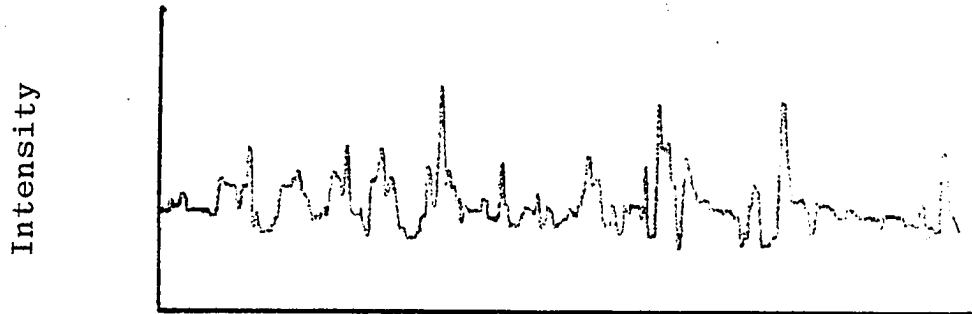
Figure 4.18. Calibration of Fourier Transform with Ronchi ruling input. (a) photograph of Fourier Transform plane (b) Linear intensity recording (c) Log-Intensity recording

Calibration of the system was done with a Ronchi ruling with 250 lines/inch (9.84 lines/mm) as the input transparency. Figure 4.18 shows the magnified frequency plane (hereafter just called the frequency plane for graphs and enlarged photos) with the Ronchi ruling as the input. Figure 4.18a is a photograph of the frequency plane. Figure 4.18b is a linear ordinate and Figure 4.18c is a logarithmic ordinate plot of relative spectrum intensity. No need for a quantitative ordinate scale was seen for simply recording spectrums and their fringe patterns. The log intensity graph clearly shows the higher-order frequency spectra.

The measured displacement in the frequency plane for the harmonically related spectra was 123.0 mm/30 harmonic spaces for 4.100 mm/harmonic displacement. The calculated value for a 9.84 line/mm Ronchi ruling was 4.002 mm/harmonic displacement and agrees very favorably with the measured value. For reference purposes, the Log Intensity recording of Figure 4.18c has its abscissa calibrated in units of 50 lines/mm. The few calculations of displacement made later will use the more precise values from the calibration.



(a)



(b)

Figure 4.19. Copy of one-dimensional density recorded signal used in experiments. (a) Photographic print (b) Linear intensity recording

### 4.2.3. Random signal

The random one-dimensional signal shown in Figure 4.19 was generated by a special homemade film exposure modulator with a 25  $\mu$ m by 25 mm clear slit illuminated by two light emitting diodes (LED). The diodes were biased to about 15 mA of current and a random signal source was then used to intensity modulate an exposure ( $\pm 10$  mA) signal onto the film as it was moved at a constant speed under the slit.

The slight y-direction change in density was caused by the nonuniform intensity of the light source and dust particles in the length of the slit. A visual inspection of the intensity plot of Figure 4.19b and the Fourier spectrum at many different places (see Figure 4.20a for example) on the film gave evidence of the quality of the random signal.

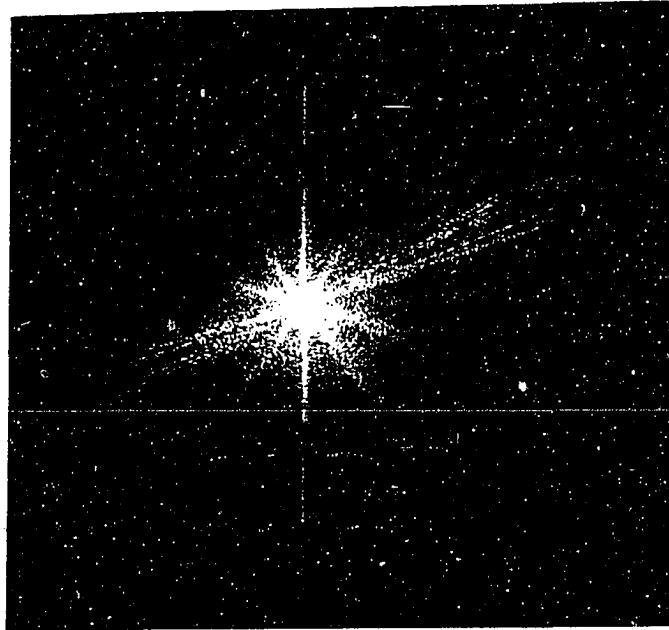
The film strip was then contact copied twice onto KODAK 120-02 film plate, first with the film strip's emulsion in contact with and then away from the film plate's emulsion. The film plate copies were then developed by conventional procedures and allowed to dry. The two final plate copies then could be placed with their emulsions in contact and one shifted with respect to the other with micrometer positioners. The ability to physically vary the shift of one signal with respect to the other was used to

control the signal shifts and resulting fringe patterns given later in Section 4.2.5 on the results on this experimental realization.

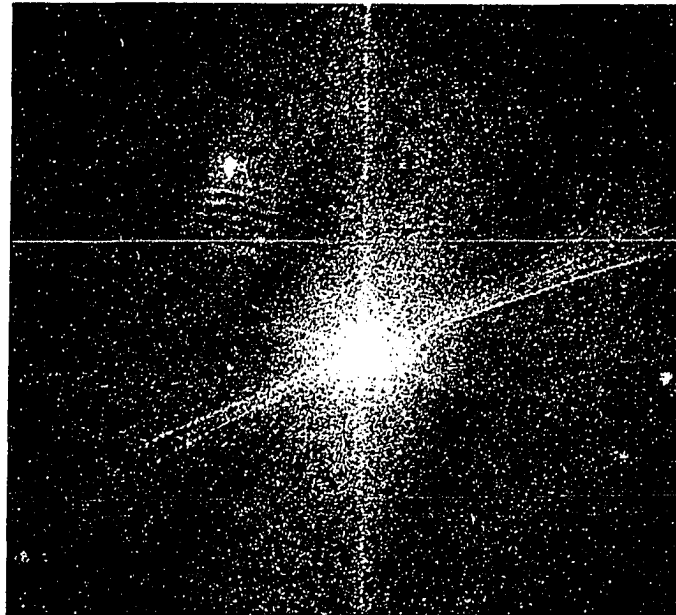
#### 4.2.4. Signal spectrum whitening

Section 4.1.4 on complex exponentiation of one-dimensional signals showed that this procedure gave a definite signal spectrum increase and broadening of the higher-order harmonics. In this section, we show experimental verification of this result obtained by bromine vapor bleaching of density copies of the random signal recorded in Figure 4.19. When this phasing by a bleaching process is applied to a density record, we can speak of the increase in spectrum width and intensity as a "whitening" of the signal spectrum. The term "complex exponentiation" will be used in reference to computational data techniques.

Two frequency spectrums of the same small 1 mm diameter area circled in Figure 4.19a are shown in Figure 4.20. The spectrum shown in Figure 4.20a is for a density record type input. The same signal area was then phased and the whitened spectrum is shown in Figure 4.20b. The only difference in the total photographic processing of these two spectral photos is that of the bromine vapor bleaching process.



(a)



(b)

Figure 4.20. Example of Fourier Transform Plane of the same 1-D Signal input showing signal spectrum whitening (a) density input (b) phased (bleached) input

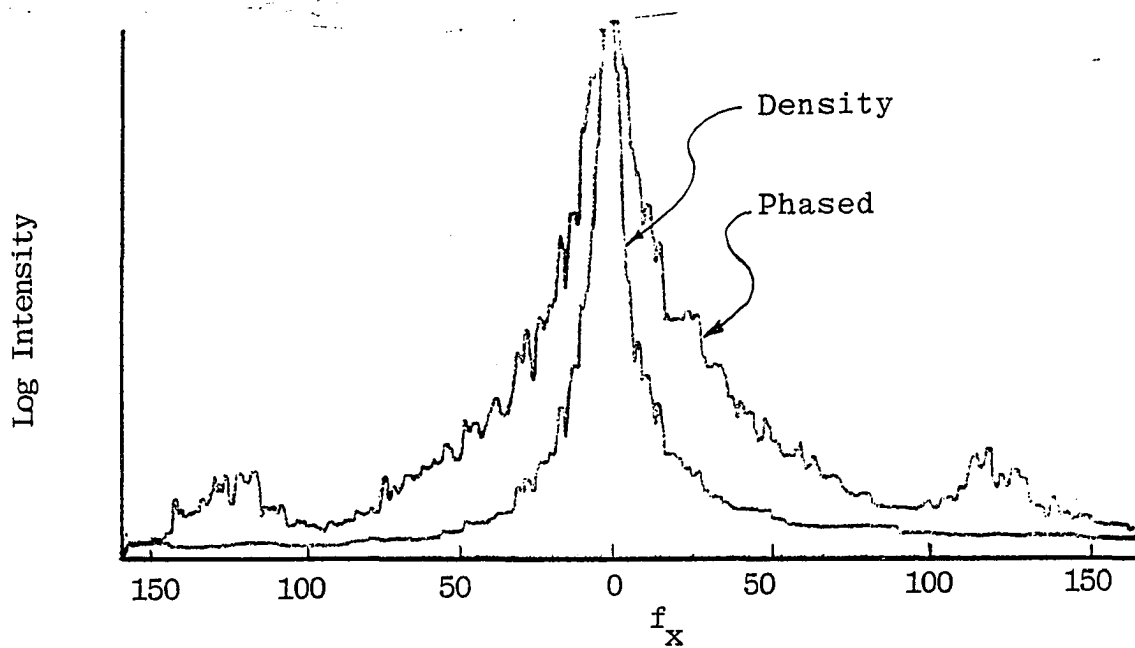


Figure 4.21. Comparative recording of Fourier Transform plane for density and phased signal shows spectrum whitening resulting from the bleaching process

A further indication of the degree of whitening is shown in the log intensity plots in Figure 4.21 of these same spectrums. This general level of whitening was readily obtained at any position of the phased random signal. More dramatic results are given in the later section on two-dimensional signal spectrum whitening.

#### 4.2.5. Experimental results

The following examples of Fourier Transform spectrum fringe patterns for cascaded and shifted 1-D signals are for phased input records. The cascading of the two density records produced such a low intensity frequency spectrum that the fringe patterns were barely discernible and then only in the region of the lowest frequencies of the spectrum. This observation further illustrated an advantage of phased input records with signal spectrum whitening. The whitened spectrum of phased inputs with shifted signals is shown in Figures 4.22 and 4.23.

To be able to compute the signal shifts for the given fringe patterns, recall that the fringe modulation for an additive shifted signal is determined by the cosine ( $\pi f_x x_0$ ) term of Equation (4.4c). Nulls in the modulation term occur when the function term  $\cos(\pi f_x x_0) = 0$  or its argument is  $\pm (2n + 1) \pi/2$ ,  $n = 0, 1, 2, 3, \dots$ . Recalling

that  $f_x = x_f/(\lambda F)$  and substituting we can write for any null position  $n$  that

$$\frac{\pi x_{fn}}{\lambda F} x_o = \pm (2n + 1) \pi/2, \quad n = 0, 1, 2, 3, \dots$$

$$\text{or } x_{f_n} = \pm \frac{(2n + 1)}{2} \frac{\lambda F}{x_o} \quad (4.29)$$

For the first null

$$x_{f_1} = \frac{\lambda F}{2x_o}$$

and for the second null

$$x_{f_2} = \frac{3\lambda F}{2x_o}$$

The separation distance,  $d_f$ , between nulls in the  $x_f$ -direction is therefore

$$d_f = x_{f_2} - x_{f_1} = \frac{3}{2} \frac{\lambda F}{x_o} - \frac{1}{2} \frac{\lambda F}{x_o} = \frac{\lambda F}{x_o}$$

or the signal shift  $x_o$  is

$$x_o = \frac{\lambda F}{d_f} \quad (4.30)$$

For a null spacing,  $d_m$ , in the magnified image

spectrum plane we have  $d_m = (Q/R)d_f = 3.33 d_f$ . Additionally, the accuracy of the measured null spacing can be increased by measuring the overall distance of several nulls and computing an average null spacing,  $\bar{d}_f$ . Equation (4.30) can then be written as

$$x_o = \lambda F / \bar{d}_f = 3.33 \lambda F / \bar{d}_m \quad (4.31)$$

where

$\bar{d}_f$  = average null spacing in frequency plane  $x_f$ - $y_f$ .

$\bar{d}_m$  = average null spacing in frequency image plane  $x_m$ - $y_m$ .

It is interesting to note that the maximum fringe null distance capable of being seen in the frequency image plane had a distance of  $\bar{d}_m = 120$  mm. For this single null distance the computed signal shift from equation (4.31) is  $x_o = 0.4067 \times 10^{-6} / \bar{d}_m = 0.4067 \times 10^{-6} / 120 \text{ mm} = 3.3389 \times 10^{-6}$  meters. This implies that if a null is not seen in the image frequency plane, the signals are shifted less than  $\pm 3.4 \mu\text{m}$ . At the other extreme speckle size and finite-detector-area limited fringe resolution to about 2 mm. This corresponds to a maximum detectable signal shift of  $\pm 200 \mu\text{m}$ .

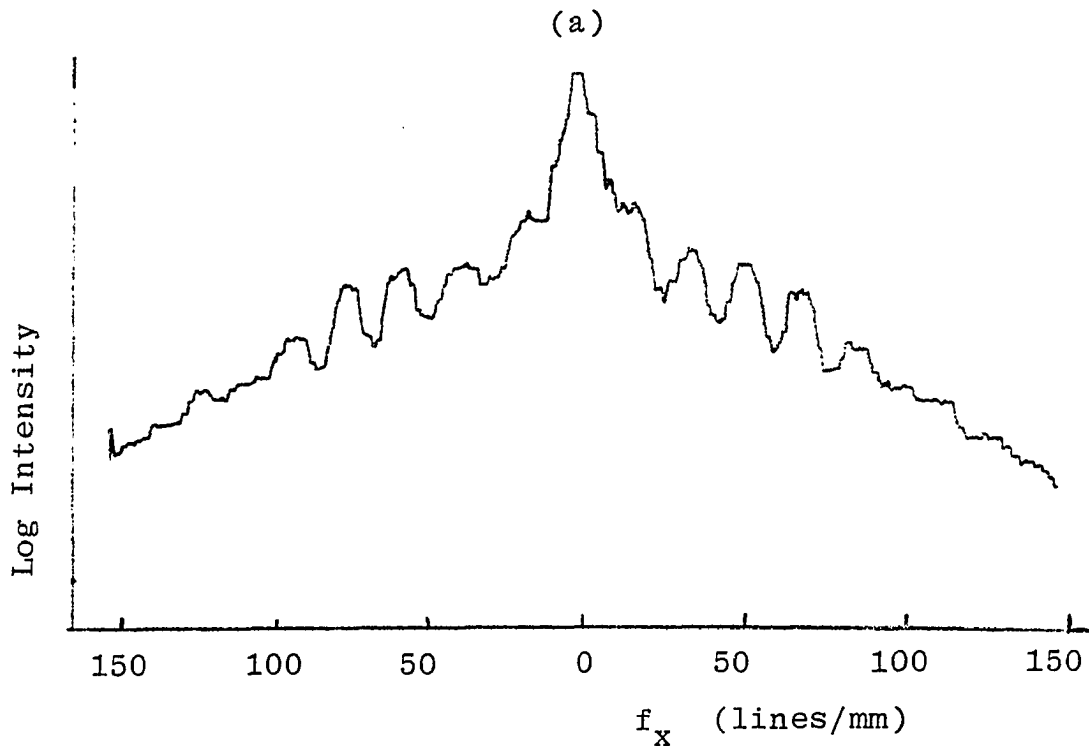
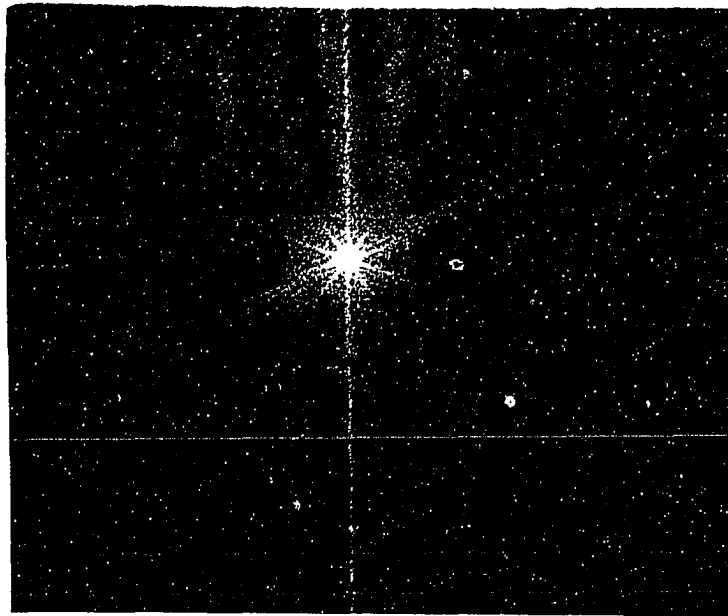
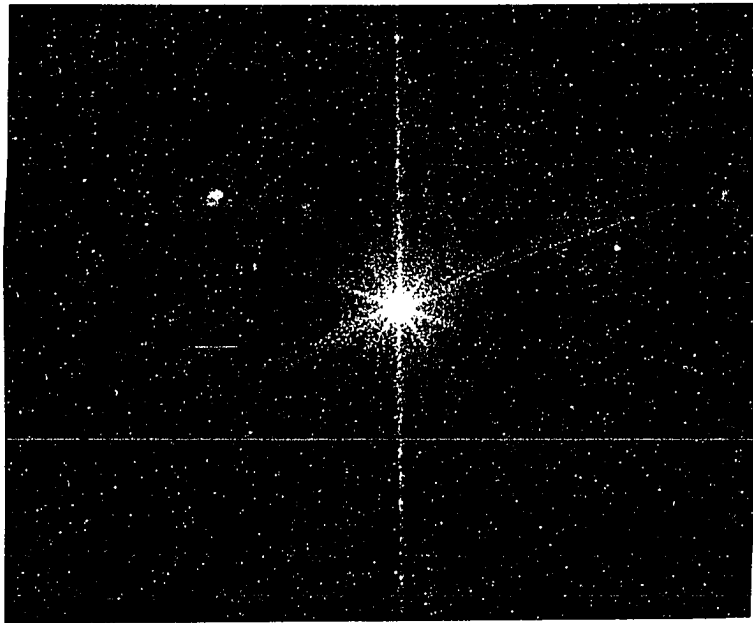
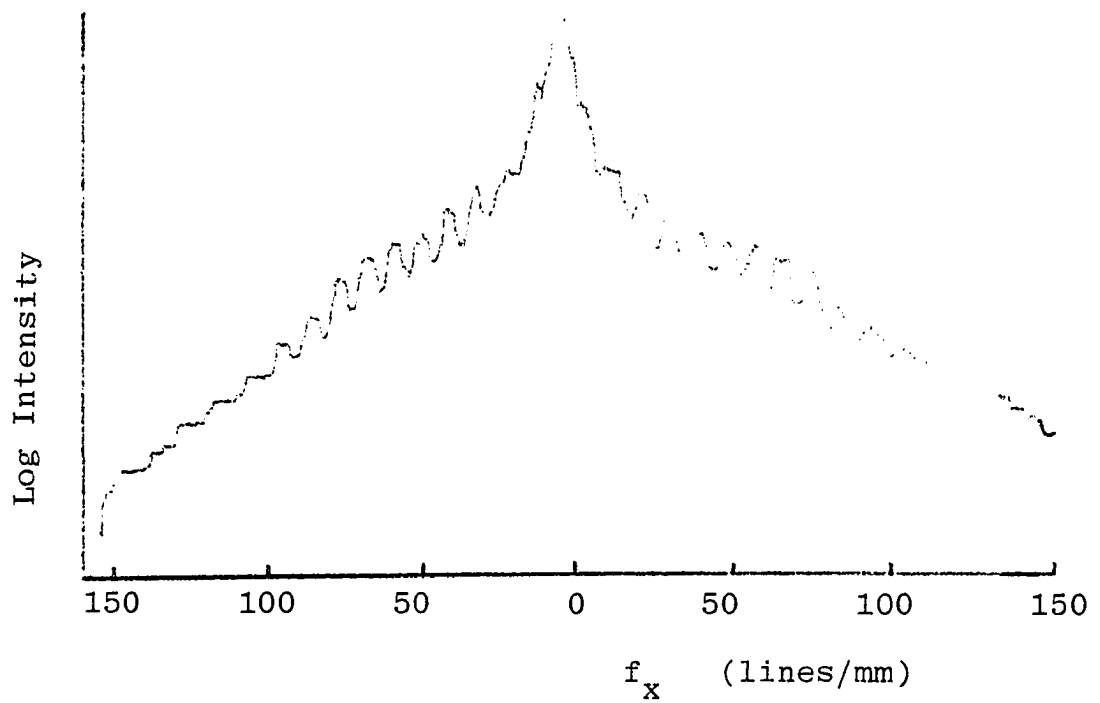


Figure 4.22. Fourier Transform Plane of "Autocorrelation" of 1-D Signals both whitened. No separation between plates. Signal shift is 0.055 mm



(a)



(b)

Figure 4.23. Fourier Transform Plane of "Autocorrelation" of 1-D Signals both whitened. No separation between plates. Signal shift is 0.115 mm

For a single-emulsion-double-exposed input record the system's detectable limits of signal shift are from  $\pm 3.4$  to  $\pm 200$  micrometers. The upper limit can be made unbounded if the input signals can be recorded separately, cascaded, and then mechanically moved so the common pixels are within these shift limits.

Figures 4.22 and 4.23 show spectrum fringe patterns caused by shifting one phased signal with respect to the other by a micro-meter positioner. The measured shifts induced by the mechanical micro-positioner were obtained by first obtaining a fringe spacing and recording the positioner's value. Then the positioner was moved through the "zero shift" and stopped when the original fringe pattern spacing was again obtained. This second positioner's value was then recorded. The difference in the positioner values was twice the actual shift distance. The measured signal shifts for Figures 4.22 and 4.23 are 0.051 mm and 0.113 mm respectively. This compares well with computed shifts of 0.055 mm and 0.115 mm.

#### 4.2.6. Conclusions

The previous section on the experimental realization of shifted signal shows how spectrum fringe patterns are produced by a coherent optical spectrum processor and

how the fringe pattern null spacings are inversely related to the signal shift. It also shows visibility of the fringe pattern is greatly enhanced by phasing the inputs to cause a signal spectrum whitening. It illustrates that there are limits of detectability of the signal shift for signals recorded as a double exposure on one record, but that there is virtually no limit on the maximum shift if separate records can be made and then cascaded and mechanically shifted to within the system's limits.

## 5. TWO-DIMENSIONAL RECORDS

### 5.1. Introduction

The previous chapter on one-dimensional records delineated the determination of the effects of a signal shift on single records, such as double exposures, or two records cascaded with no separation between them. The obvious extension of those results would be to apply them to two-dimensional signals. To further simplify the mechanical positioning of input records they are recorded as single exposures and cascaded with an adjustable spacing between them. The following section is the theoretical development of this new configuration.

### 5.2. Theory

Figure 5.1 shows a plane wave of phasor amplitude  $U_0$  impinging on the two input transparencies with separation,  $s$ , between them.

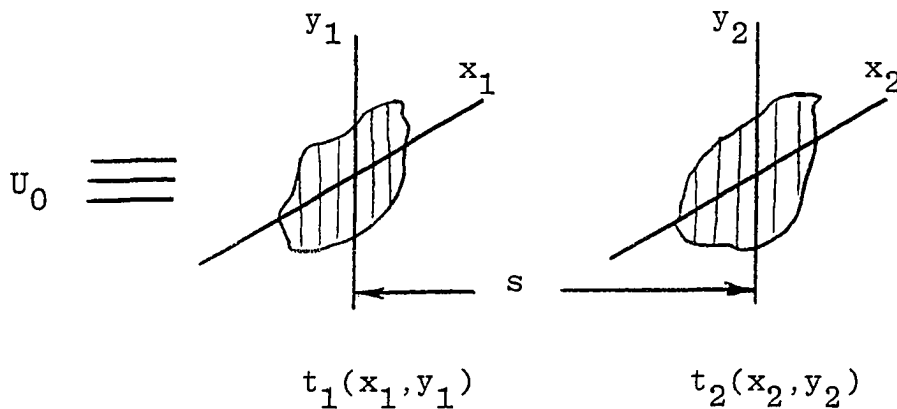


Figure 5.1. The separated input transparencies  $t_1$  and  $t_2$

We can write the amplitude transmission for these transparencies as

$$t_1(x_1, y_1) = t_{o1} + a_1(x_1, y_1)$$

$$\text{and } t_2(x_2, y_2) = t_{o2} + a_2(x_2, y_2) \quad (5.1)$$

where  $t_{o1}$  and  $t_{o2}$  are the average transmissions and  $a_1$  and  $a_2$  are the signals of interest.

The phasor amplitude of the signal to the right of transparency  $t_1$  can be written as

$$U_1(x_1, y_1) = U_o [ t_{o1} + a_1(x_1, y_1) ] \quad (5.2)$$

Goodman (7) and others have shown that the light transfer through open space from plane  $x_1$ - $y_1$  to plane  $x_2$ - $y_2$  can be specified by a phase factor and a Fourier Transform of the light from the plane  $x_1$ - $y_1$ . For the light from  $t_1(x_1, y_1)$  and incident on  $t_2(x_2, y_2)$  we can write

$$U_2(x_2, y_2) = K e^{j(\pi/\lambda s)(x_2^2 + y_2^2)} \cdot F \left\{ U_1(x_1, y_1) e^{j(\pi/\lambda s)(x_1^2 + y_1^2)} \right\} \quad (5.3)$$

where  $x_2/\lambda s = f_{x_1}$  and  $y_2/\lambda s = f_{y_1}$

relate position in the  $x_2$ - $y_2$  plane with spacial frequency  $f_x, f_y$  in the  $x_1$ - $y_1$  plane. Substituting Equation (5.2) into (5.3) and multiplying by  $t_2$ , from Equation 5.1, the light on the right side of  $t_2$  can be written as

$$\begin{aligned}
 U_2(x_2, y_2) &= K [t_{o2} + a_2(x_2, y_2)] e^{j(\pi/\lambda s)(x_2^2 + y_2^2)} \\
 &\cdot F \left\{ U_o [t_{o1} + a_1(x_1, y_1)] e^{j(\pi/\lambda s)(x_1^2 + y_1^2)} \right\} \\
 &= K [t_{o2} + a_2(x_2, y_2)] e^{j(\pi/\lambda s)(x_2^2 + y_2^2)} \\
 &\cdot \iint_{-\infty}^{\infty} U_o [t_{o1} + a_1(x_1, y_1)] e^{j(\pi/\lambda s)(x_1^2 + y_1^2)} \\
 &\cdot e^{-j \frac{2\pi}{\lambda s} (x_2 x_1 + y_2 y_1)} dx_1 dy_1 \quad (5.4)
 \end{aligned}$$

This then describes the phasor amplitude of the light at the input plane of the optical processor shown in Figure 4.17. Note that the subscripts for the input plane have been changed to make the input be to the  $x_2$ - $y_2$  plane.

If we assume that

$$U_o \equiv 1 \text{ and } t_{o1} = t_{o2} = t_o$$

the Fourier Transform of the corresponding input, i.e., Equation 5.4, can be written as

$$U_f(x_f, y_f) = Ke^{j(\pi/\lambda F)(1-D/F)(x_f^2 + y_f^2)} F \left\{ U_2(x_2, y_2) \right\} \quad (5.5a)$$

$$\begin{aligned} &= Ke^{j(\pi/\lambda F)(1-D/F)(x_f^2 + y_f^2)} \\ &\cdot \iint_{-\infty}^{\infty} e^{-j(2\pi/\lambda F)(x_f x_2 + y_f y_2)} \\ &\cdot [t_o + a_2(x_2, y_2)] e^{j(\pi/\lambda s)(x_2^2 + y_2^2)} \\ &\cdot \left[ \iint_{-\infty}^{\infty} [t_o + a_1(x_1, y_1)] e^{j(\pi/\lambda s)(x_1^2 + y_1^2)} \right. \\ &\cdot \left. e^{-j2\pi/\lambda s(x_2 x_1 + y_2 y_1)} dx_1 dy_1 \right] dx_2 dy_2 \quad (5.5b) \end{aligned}$$

The integration can be broken down into four separate integrals. The first integral is

$$\begin{aligned}
 I_1(x_f, y_f) &= \iint_{-\infty}^{\infty} t_o^2 e^{-j(2\pi/\lambda F)(x_f x_2 + y_f y_2)} \\
 &\quad \cdot e^{j(\pi/\lambda s)(x_2^2 + y_2^2)} \\
 &\quad \left[ \iint_{-\infty}^{\infty} e^{j(\pi/\lambda s)(x_1^2 + y_1^2)} \right. \\
 &\quad \left. \cdot e^{-j(2\pi/\lambda s)(x_2 x_1 + y_2 y_1)} dx_1 dy_1 \right] dx_2 dy_2
 \end{aligned}
 \tag{5.6a}$$

If we let

$$b^2 = \lambda s, \quad f_x = x_2/\lambda s \text{ and } f_y = y_2/\lambda s$$

the inner integral here becomes

$$j\lambda s e^{-j\pi\lambda s [(x_2/\lambda s)^2 + (y_2/\lambda s)^2]}$$

and dropping the complex multiplier  $j\lambda s$  gives

$$e^{+j(\pi/\lambda s)(x_2^2 + y_2^2)}$$

Therefore

$$\begin{aligned} I_1(x_f, y_f) &\triangleq t_o^2 \iint_{-\infty}^{\infty} e^{-j(2\pi/\lambda F)(x_f x_2 + y_f y_2)} \\ &\quad \cdot e^{j(\pi/\lambda s)(x_2^2 + y_2^2)} \\ &\quad \cdot e^{-j(\pi/\lambda s)(x_2^2 + y_2^2)} dx_2 dy_2 \\ &= t_o^2 \delta\left(\frac{x_f}{s}, \frac{y_f}{s}\right) \end{aligned} \quad (5.6b)$$

This is what we would expect the average transmittance would give. Thus for the first integral we have

$$U_1(x_f, y_f) = t_o^2 \delta(f_x, f_y) e^{j(\pi/\lambda F)(1-D/F)(x_f^2 + y_f^2)} \quad (5.7)$$

The second integral is

$$I_2(x_f, y_f) \triangleq t_o \iint_{-\infty}^{\infty} e^{j\pi/\lambda s(x_2^2 + y_2^2)} \cdot e^{-j(2\pi/\lambda F)(x_f x_2 + y_f y_2)} \cdot \left[ \iint_{-\infty}^{\infty} a_1(x_1, y_1) e^{j(\pi/\lambda s)(x_1^2 + y_1^2)} \cdot e^{-j(2\pi/\lambda s)(x_f x_1 + y_f y_1)} dx_1 dy_1 \right] dx_2 dy_2 \quad (5.8a)$$

Combining terms and exchanging the order of integration gives

$$\begin{aligned}
I_2(x_f, y_f) &= t_0 \iint_{-\infty}^{\infty} a_1(x_1, y_1) e^{j(\pi/\lambda s)(x_1^2 + y_1^2)} \\
&\quad \cdot \left[ \iint_{-\infty}^{\infty} e^{j(\pi/\lambda s)(x_2^2 + y_2^2)} \right. \\
&\quad \cdot e^{-j(2\pi/\lambda) \left[ \left(\frac{x_f}{F} + \frac{x_1}{s}\right)x_2 + \left(\frac{y_f}{F} + \frac{y_1}{s}\right)y_2 \right]} \\
&\quad \left. \cdot dx_2 dy_2 \right] dx_1 dy_1 \quad (5.8b)
\end{aligned}$$

then for  $b^2 = \lambda s$ ,  $f_x = \frac{\frac{x_f}{F} + \frac{x_1}{s}}{\lambda}$  and  $f_y = \frac{\frac{y_f}{F} + \frac{y_1}{s}}{\lambda}$

the inner integral gives

$$j\lambda s e^{-j(\pi \lambda s / \lambda^2) \left[ \left(\frac{x_f}{F} + \frac{x_1}{s}\right)^2 + \left(\frac{y_f}{F} + \frac{y_1}{s}\right)^2 \right]}$$

and dropping the complex multiplier  $j\lambda s$  gives

$$e^{-j(\pi s / \lambda) \left[ \frac{x_f^2 + y_f^2}{F^2} + \frac{x_1^2 + y_1^2}{s^2} + 2\left(\frac{x_f x_1 + y_f y_1}{Fs}\right) \right]}$$

The integral  $I_2$  with its quadratic multiplier from the

original integral then gives

$$\begin{aligned}
 U_{f2}(x_f, y_f) &= e^{j(\pi/\lambda F)(1-D/F)(x_f^2 + y_f^2)} \\
 &\quad e^{-j\pi s/\lambda F^2(x_f^2 + y_f^2)} \\
 &\quad \iint_{-\infty}^{\infty} e^{j(\pi/\lambda s)(x_1^2 + y_1^2)} a_1(x_1, y_1) \\
 &\quad e^{-j(\pi/\lambda s)(x_1^2 + y_1^2)} \\
 &\quad \cdot e^{-j(\pi/F\lambda)2(x_f x_1 + y_f y_1)} dx_1 dy_1 \\
 &= e^{j(\pi/\lambda F)(1-(D+s)/F)(x_f^2 + y_f^2)} F \left\{ a_1(x_1, y_1) \right\}
 \end{aligned}$$

where

$$\begin{aligned}
 f_{x_1} &= x_f/\lambda F \text{ and } f_{y_1} = y_f/\lambda F \\
 &= e^{j\pi/\lambda F(1 - \frac{D+s}{F})(x_f^2 + y_f^2)} \underline{A}_1(x_f, y_f) \quad (5.9)
 \end{aligned}$$

The third integral is similar to the second and gives by inspection

$$U_{f3}(x_f, y_f) = e^{j(\pi/\lambda F)(1-D/F)(x_f^2 + y_f^2)} \underline{A}_2(x_f, y_f) \quad (5.10)$$

The fourth integral is considerable more complex and can be written as

$$I_4(x_f, y_f) = \iint_{-\infty}^{\infty} a_2(x_2, y_2) e^{j(\pi/\lambda s)(x_2^2 + y_2^2)} \cdot e^{-j(2\pi/\lambda F)(x_f x_2 + y_f y_2)} \cdot \left[ \iint_{-\infty}^{\infty} a_1(x_1, y_1) e^{j(\pi/\lambda s)(x_1^2 + y_1^2)} \cdot e^{-j(2\pi/\lambda s)(x_2 x_1 + y_2 y_1)} dx_1 dy_1 \right] dx_2 dy_2 \quad (5.11)$$

Although we cannot, in general, evaluate these integrals explicitly, we can visualize their optical effects. If  $s \neq 0$  the inner integral will produce a scattering of the incoming light which will be rescattered by the second transparency. Thus, in the  $x_f$ - $y_f$  plane, the effects of  $a_1$  and  $a_2$  will be to produce a rather random distribution of light around the origin of coordinates. This will be true even if  $a_2 \equiv a_1$ .

From the above, we see that the first and fourth integrals offer little value to us. It is the second and third terms we are interested in. Summing  $U_{f_2}$  and  $U_{f_3}$  and then deleting the unimportant unity amplitude common term

$$e^{j(\pi/\lambda F)(1-D/F)(x_f^2 + y_f^2)}$$

leaves

$$U_{f_{2+3}}(x_f, y_f) = e^{-j(\pi s/\lambda F^2)(x_f^2 + y_f^2)} \underline{A}_1(x_f, y_f) + \underline{A}_2(x_f, y_f) \quad (5.12)$$

Now if we let

$$a_2(x_2, y_2) = \infty a_1(x_1 - x'_0, y_1 - y'_0) + \tilde{\delta}(x_1, y_1)$$

where  $\alpha$  is the similarity factor and  $\tilde{\delta}(x_1, y_1)$  is the difference between  $a_2$  and shifted  $a_1$ , we can then write

$$\begin{aligned}
 U_{f_{2+3}}(x_f, y_f) &= \underline{A}_1(x_f, y_f) \left[ e^{-j(\pi s / \lambda F^2)(x_f^2 + y_f^2)} \right. \\
 &\quad \left. + \alpha e^{j(2\pi / \lambda F)(x_f x'_o + y_f y'_o)} \right] + \Delta(x_f, y_f) \\
 &= (1 - \alpha) \left[ e^{-j(\pi s / \lambda F^2)(x_f^2 + y_f^2)} \right] \\
 &\quad \cdot \underline{A}_1(x_f, y_f) + \Delta(x_f, y_f) \\
 &\quad + 2\alpha \underline{A}_1(x_f, y_f) e^{-j(\pi s / 2\lambda F^2)(x_f^2 + y_f^2)} \\
 &\quad \cdot e^{j(\pi / \lambda F)(x_f x'_o + y_f y'_o)} \\
 &\quad \cdot \cos \left\{ \pi / \lambda F \left[ x_f \left( x'_o - \frac{sx_f}{2F} \right) + y_f \left( y'_o - \frac{sy_f}{2F} \right) \right] \right\} \\
 &\hspace{15em} (5.13)
 \end{aligned}$$

This result indicates that on a background illumination of a rather random nature (provided the spectrum  $\underline{A}_1$  is broad and composed of frequency components spread over a large portion of the spectrum) there will be a set of circular Fresnel zone fringes. The contrast of these fringes depends on the similarity factor  $\alpha$  between the two transparencies. The center of this Fresnel zone pattern will be at

$$x_f = (F/s)x'_0 \quad \text{and} \quad y_f = (F/s)y'_0 \quad (5.14)$$

The spacial frequencies of the Fresnel zone pattern are given by

$$\begin{aligned} f_{x_f} &= \frac{\partial}{\partial x_f} \left[ \frac{s}{4\lambda F^2} (x_f^2 + y_f^2) - \frac{x_f x'_0 + y_f y'_0}{2\lambda F} \right] \\ &= \frac{s x_f}{2\lambda F^2} - \frac{x'_0}{2\lambda F} = \frac{s}{2\lambda F^2} \left[ x_f - \frac{F}{s} x'_0 \right] \end{aligned} \quad (5.15a)$$

and

$$f_{y_f} = \frac{s}{2\lambda F^2} \left[ y_f - \frac{F}{s} y'_0 \right] \quad (5.15b)$$

Both Equations (5.14) and (5.15) show that the center of the Fresnel zone pattern is a direct function of the shift  $x_0'$ ,  $y_0'$  between common elements of the two cascaded images. Therefore, it was expected that the easy recognition of simple circular zone rings, even offset from the optical axis, would readily allow visual detection of the alignment of the rings with respect to the optical axis. Furthermore, when the zone rings are centered about the optical axis similar pixels in both transparencies are expected to be aligned on the optical axis. We can also see the period (diameter) of the zone rings are inversely proportional to the separation distance,  $s$ . Therefore, this adjustable parameter should allow selection of a ring diameter to give the best ring visibility in different signal spectrums.

### 5.3. Experimental Realization

#### 5.3.1. Introduction

A major advantage of coherent optical data processing is the ability to readily use two-dimensional input records and process them in a parallel mode of operation. The speed and simplicity with which this processing is done is exemplified by the results described in this chapter. To give a better understanding of the processing, a description

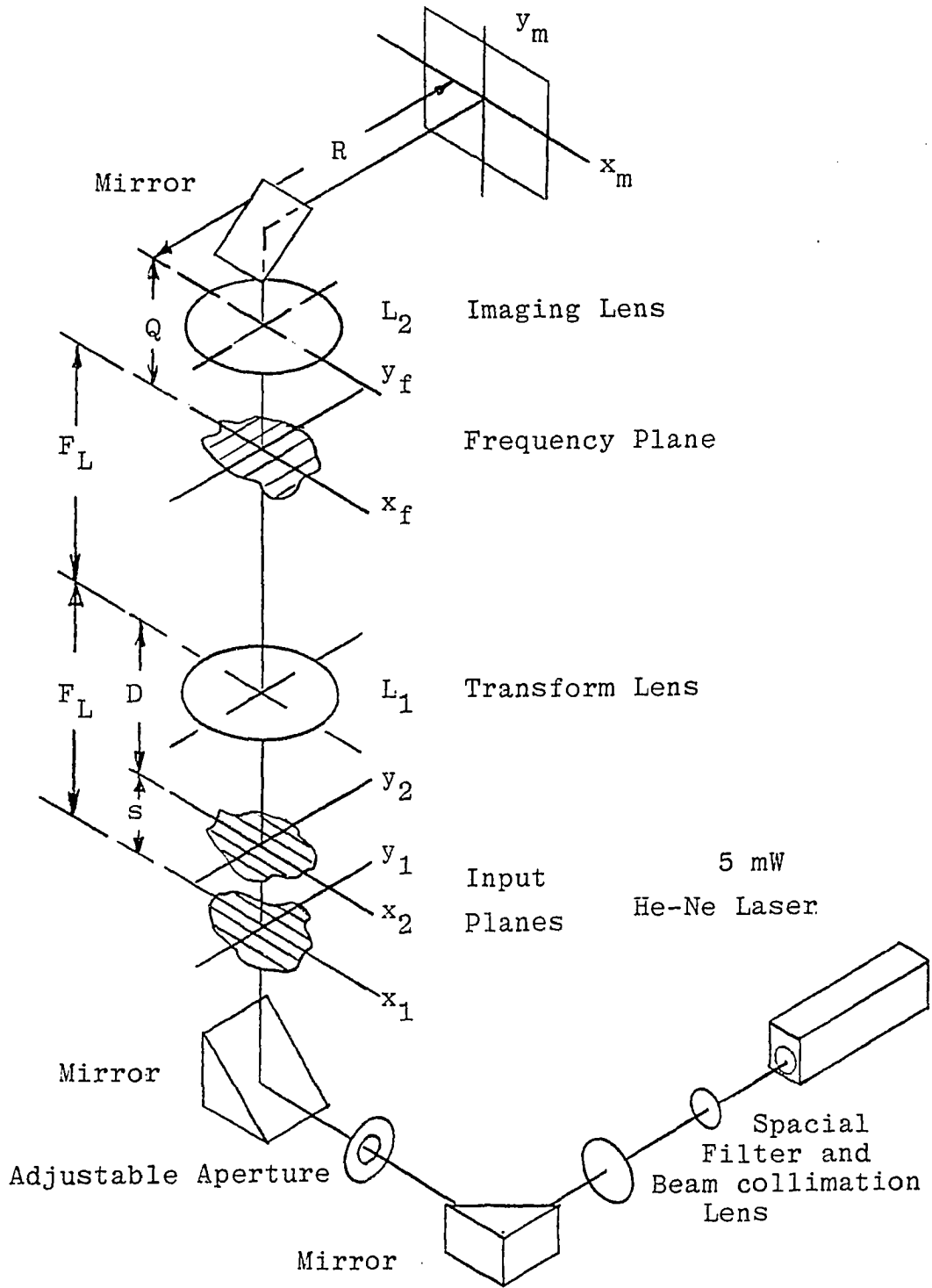


Figure 5.2. Schematic diagram of 2-D optical data processor

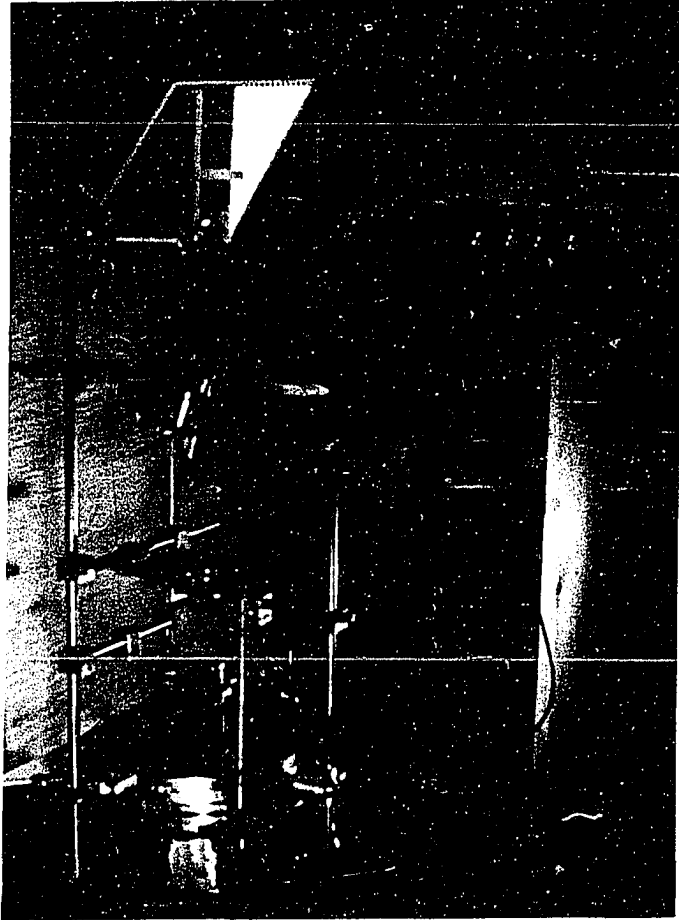


Figure 5.3. Photograph of the 2-D optical data processor

of the apparatus and its features are described in the next section.

### 5.3.2. Apparatus

Figure 5.2 shows a schematic representation of the major components of the optical data processor used in the experimental realization sections of this dissertation. Figure 5.3 shows a photograph of the actual apparatus used. The coherent light source was a Spectra Physics Model 120, 5 mW He-Ne laser. The light beam is spacially filtered by lens  $L_D$  and the pin-hole and then collimated to a parallel beam by lens  $L_C$ . The adjustable aperture provided by a small iris diaphragm was used to vary the area of illumination on the input records. The first surface mirrors are simply used to change the direction of the optical axis into a more compact and usable geometry.

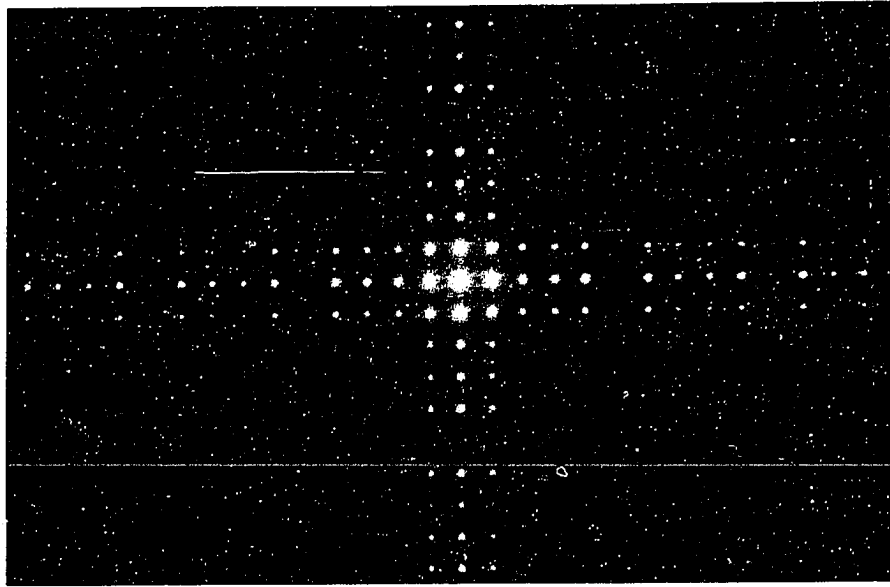
The first input record is held on the  $x_1$ - $y_1$  plane micro-positioner table. The second input record was held by another micro-positioner fixed to and above that table. The resultant motions of the input records are that both moved with the lower positioner and only the second record moved differentially with the upper positioner. The separation,  $s$ , between the records was also adjustable by vertically moving the upper positioner.

The Transform lens  $L_1$  was positioned one focal length ( $F_L = 193$  mm) above the lower positioner. The frequency (Transform) plane was, therefore, one focal length above lens  $L_1$ . It was at this frequency plane where photographs of the spectrums and spectrum fringe patterns in Chapter 4, and later in this chapter were made. The imaging lens,  $L_2$ , provided a magnified image of the frequency plane. It was in this plane where a photo optic detector was scanned across the  $x_m$ -axis and the spectrum intensity plots recorded by a x-y recorder.

### 5.3.3. Calibration

Calibration of the system was done with a 60 micrometer precision sieve with 100 holes/cm (10.0 lines/mm) as the 2-D input transparency. Figure 5.4 shows the frequency plane photograph and a graph of log intensity along the  $x_m$ -axis. The measured displacement in the frequency plane for the harmonically related spectra was 82.5 mm/20 harmonic spaces for an average of 4.15 mm/harmonic space. The calculated value from Equation (4.28) multiplied by the image magnification factor 3.33 was 4.07 mm/harmonic space and agrees favorably with the above measured value. For reference purposes, the abscissa of the intensity graph has been calibrated in increments of 50 lines/mm to allow

(a)



(b)

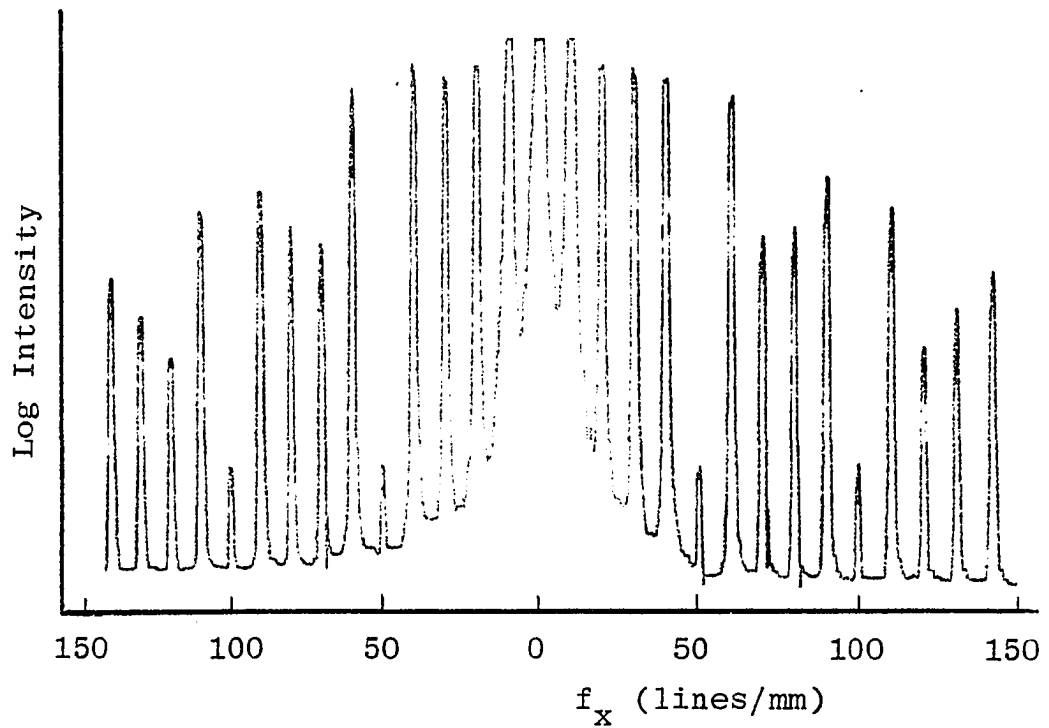


Figure 5.4. Calibration of Fourier Transform with precision sieve input. (a) Photograph and (b) Log-Intensity recording.

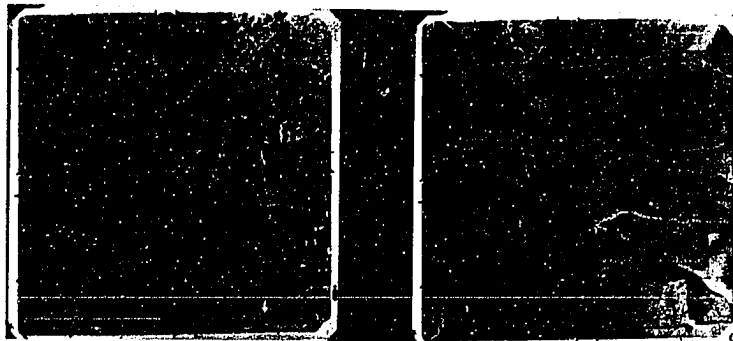


Figure 5.5. Topographical terrain stereotransparencies

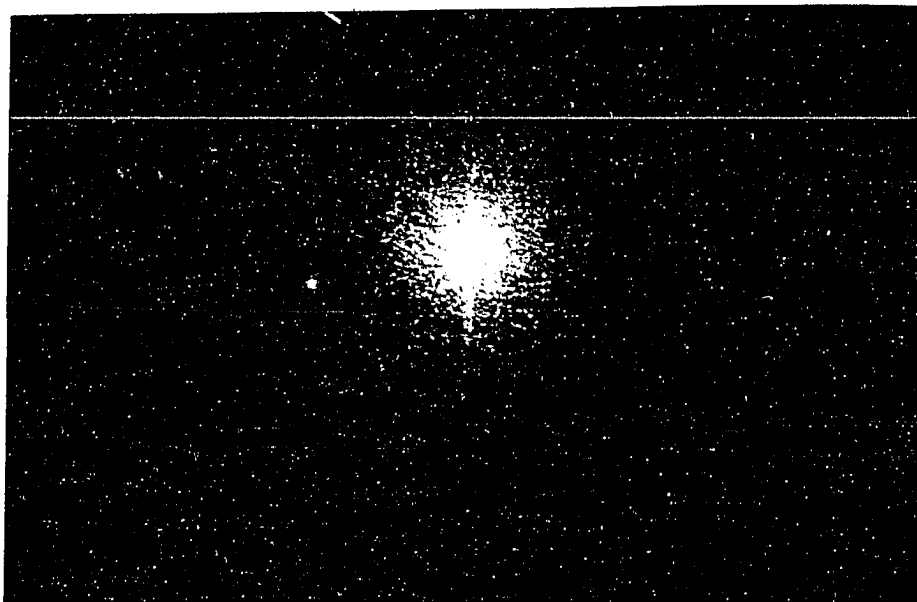


Figure 5.6. Fourier Transform of the circled area of Figure 5.5 as a density record input

easy reading of spacial frequency. Note also how the log intensity ordinate enhances the higher-order harmonics.

#### 5.3.4. Signal spectrum whitening

The whitening of the signal spectrum for a one-dimensional record phased by bromine vapor bleaching of density records was given in Section 4.2.4. The results of phasing by bleaching of two-dimensional records is given in this section.

Figure 5.5 is a copy of two topographical stereo-transparencies that were used as the signal source for this experiment. The circled area is the two-dimensional signal area that was used for both the density and the phased input records. Figure 5.6 shows the Fourier Transform of the circled area obtained from a density type record with an average optical density of 0.8. Note the intense low-order spectra and the very weak higher-order spectra. This is a common result of density type input records.

This original signal record was copied four times with varying exposures onto KODAK 120-02 film plate to obtain four separate records with average optical densities of 0.8, 1.1, 1.7, and 2.0. The records were then bleached in bromine vapor and used to show the general effect of average density of signal spectrum whitening in the following

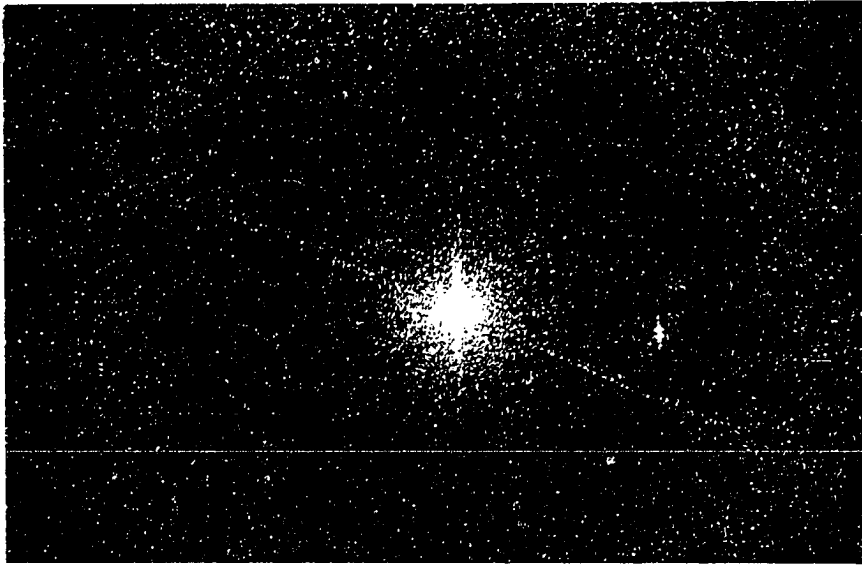


Figure 5.7. Fourier Transform of circled area showing spectrum whitening for a bleached average density of 0.8

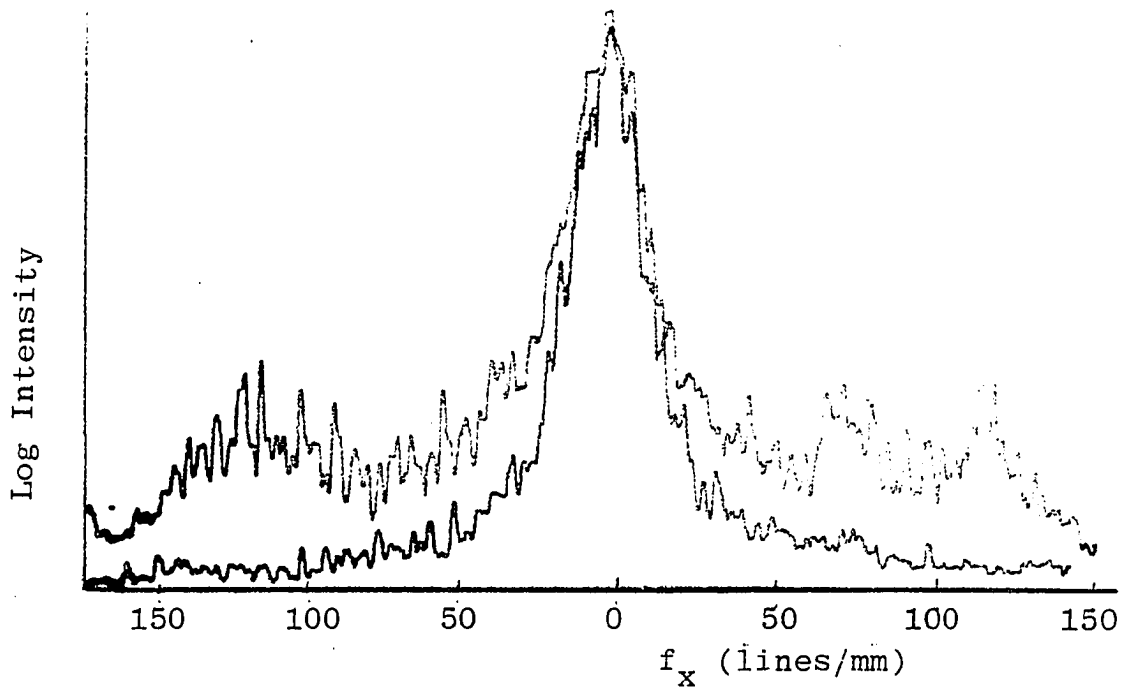
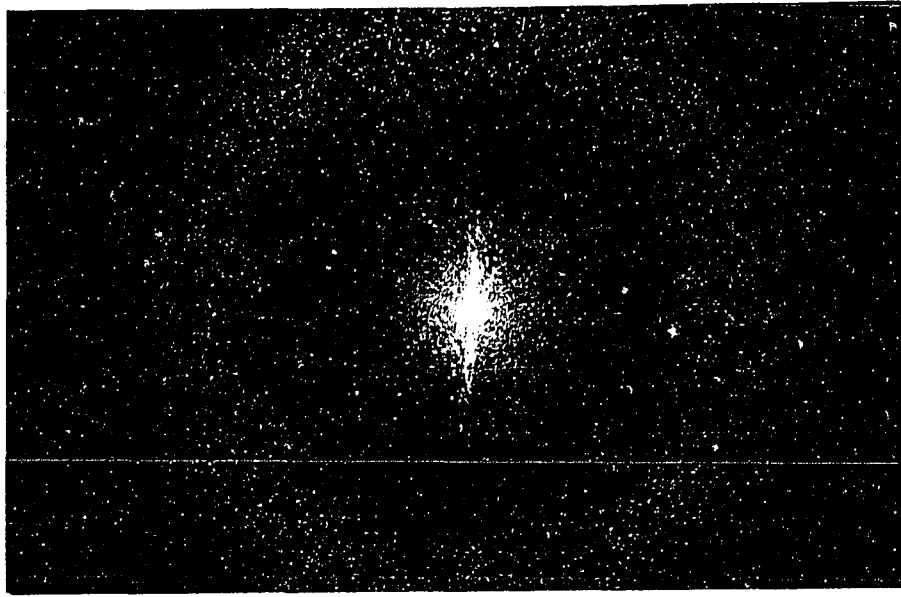


Figure 5.8. Comparative graph of Fourier Transform plane of circled area showing spectrum whitening effects for records with an average density of 0.8

(a)



(b)

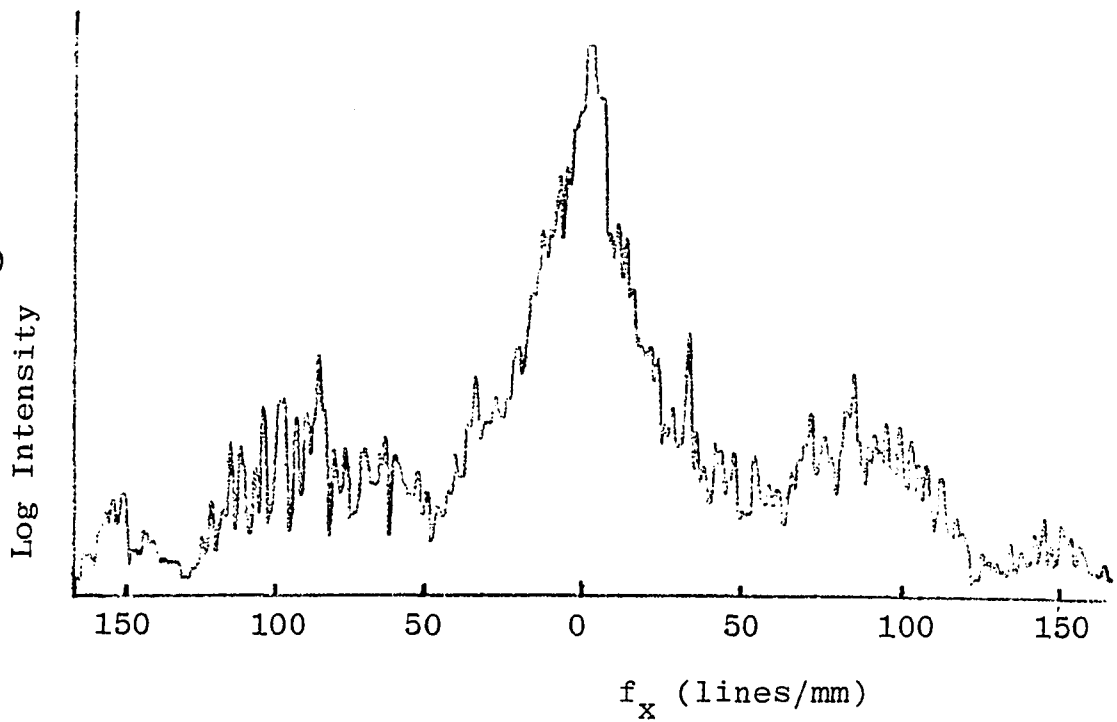


Figure 5.9. Fourier Transform plane of circled area showing spectrum whitening effects for a record with average density of 1.1

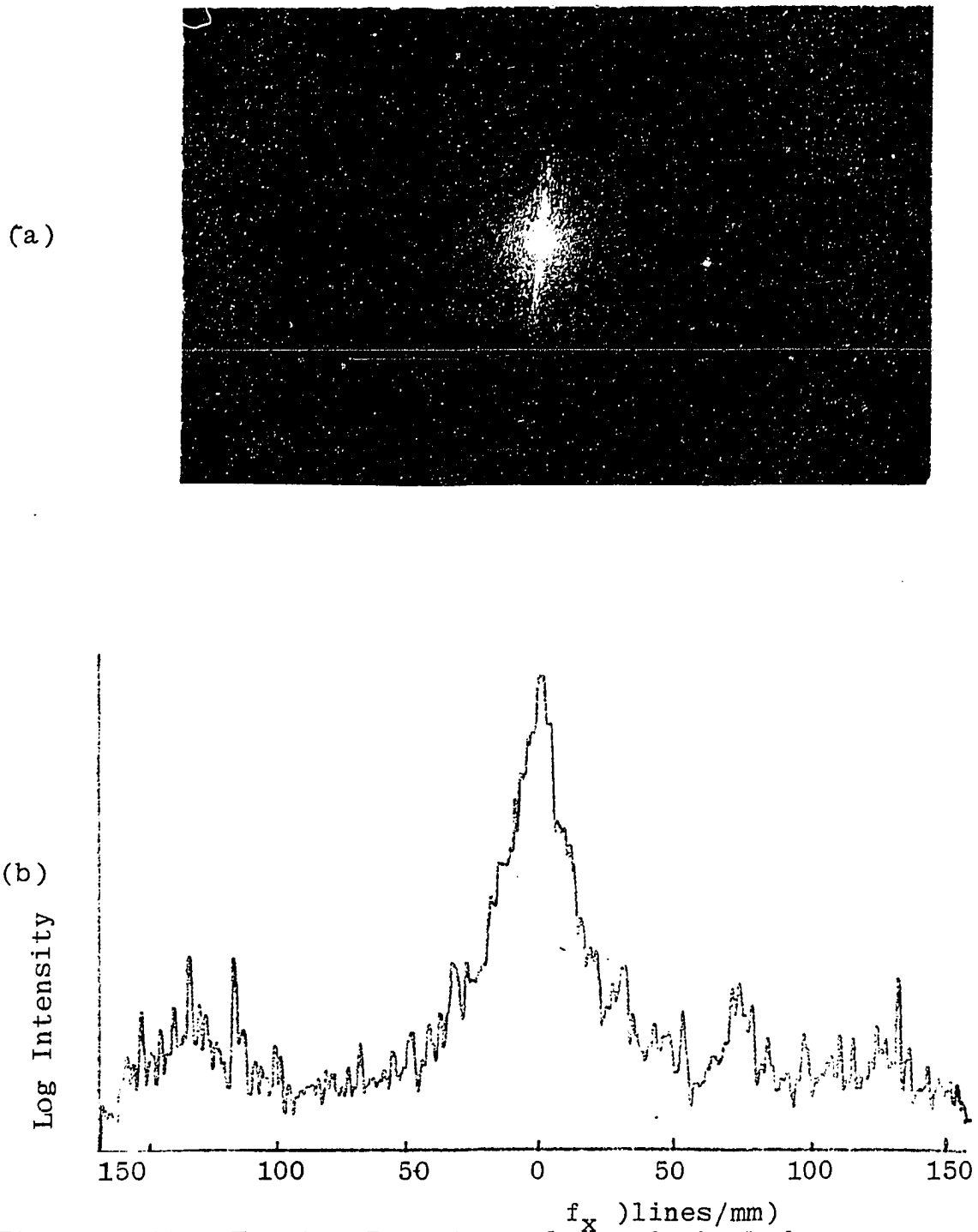
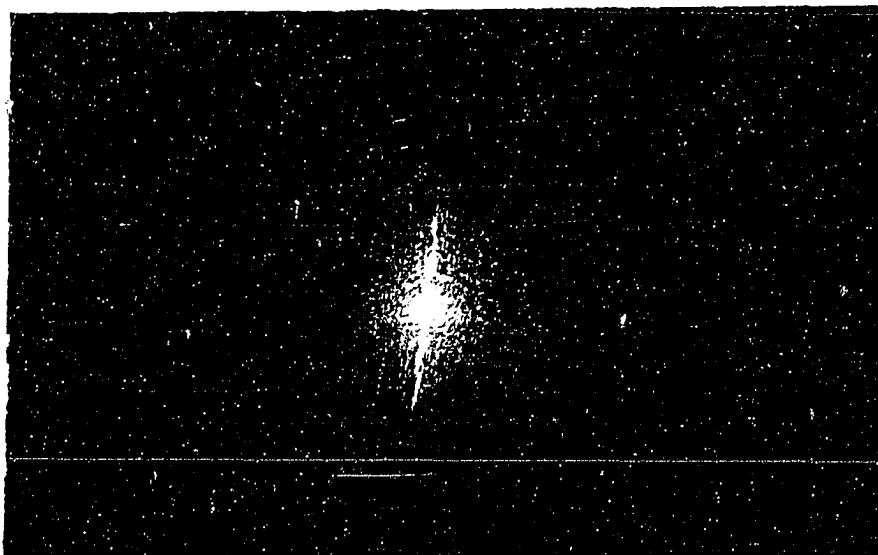


Figure 5.10. Fourier Transform plane of circled area showing spectrum whitening effects for a record with average density of 1.7

(a)



(b)

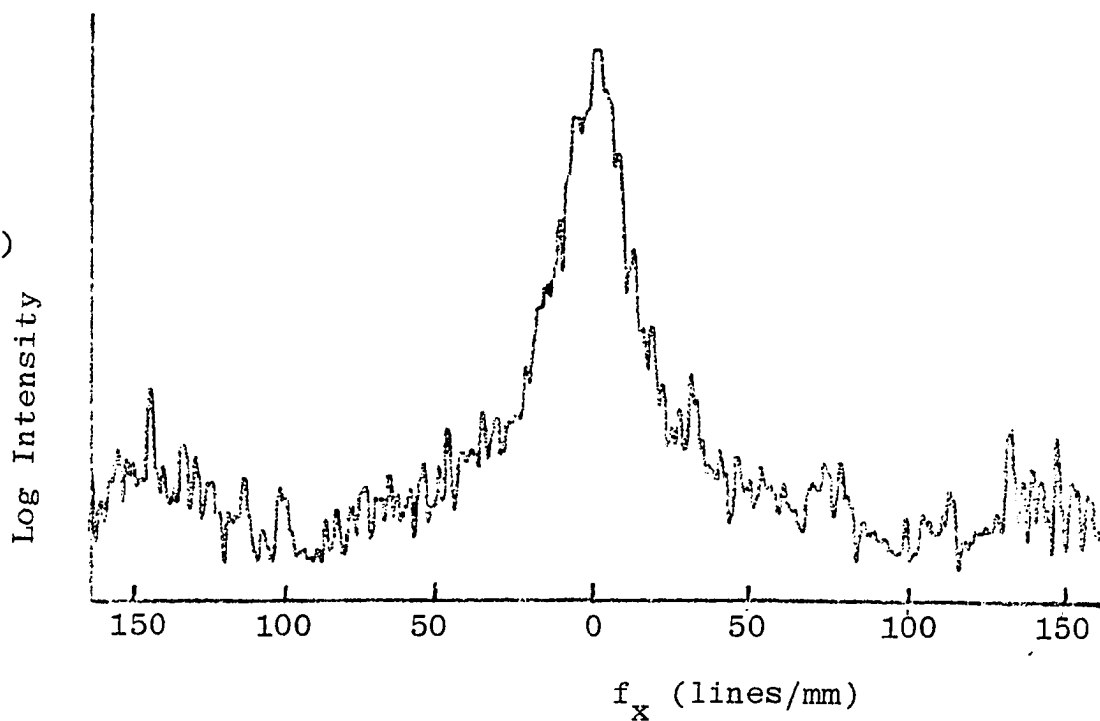


Figure 5.11. Fourier Transform plane of circled area showing spectrum whitening effects for a record with average density 2.0

examples. In each example, the input signal was the original circled area of Figure 5.5. A careful inspection of the nearly vertical spectra verifies the similarity of the inputs.

The comparative graph of the Fourier Transform planes shown in Figure 5.8 shows the effects of signal spectrum whitening by bleaching for records with an average density of 0.8. This graph is an intensity plot of the spectrums of Figures 5.6 and 5.7. The only difference in the total photographic processing is the bromine vapor bleaching process. Figures 5.9, 5.10 and 5.11 show signal spectrum whitening for phased input records with an initial average density of 1.1, 1.7 and 2.0 respectively. The log intensity plots aid the reader by giving a means of relative comparison for the spectrum intensities of the photographs. No exact quantitative relationship between the degree of spectrum whitening and record density appeared to be formable here. The major result of these experiments was the verification that signal spectrum whitening occurred in two-dimensional records as was expected.

#### 5.3.5. Fresnel zone ring "correlation"

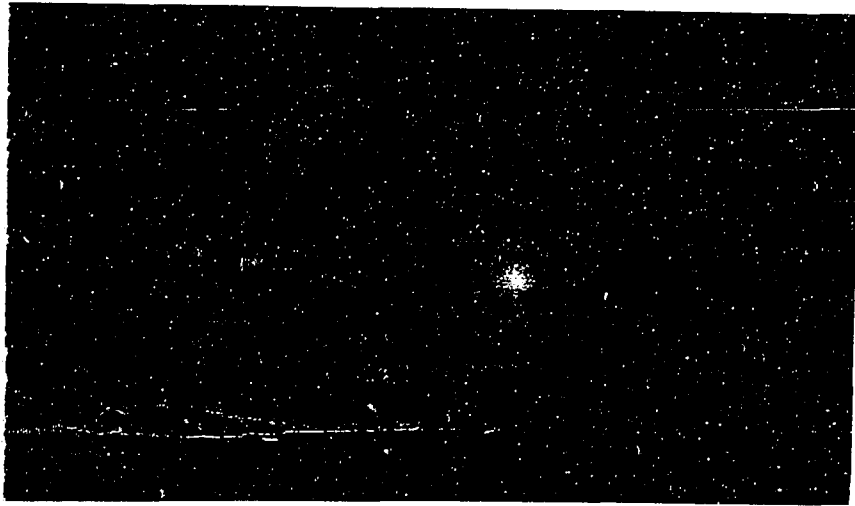
The following subsections present experimental verification of the existence of Fresnel zone ring

"correlation" for both auto and cross correlation type inputs. The inverse relationship between Fresnel zone ring radius and input record separation is demonstrated by autocorrelation of identical input records, and an offset zone ring pattern due to shifted input record is shown. A comparison of density and phased inputs for "cross correlation" is shown.

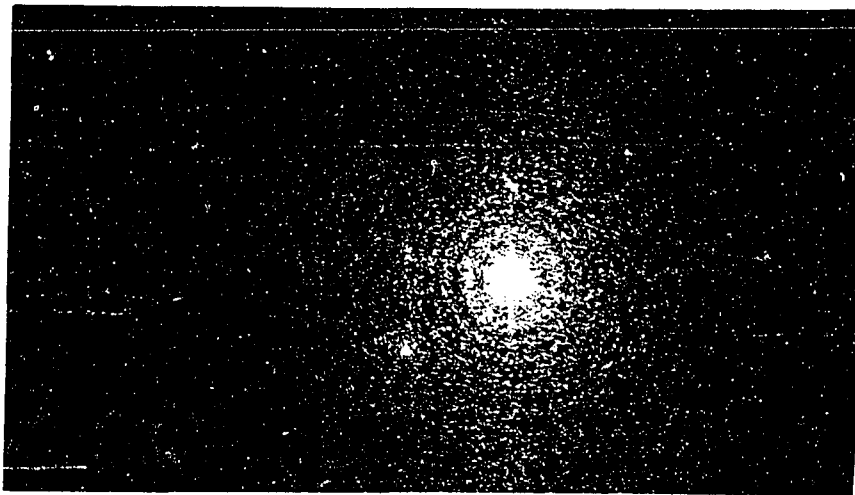
5.3.5.1. "Autocorrelation" and zone ring diameter versus plate separation Figure 5.12 and 5.13 show Fresnel zone ring "autocorrelation" of two identical phased copies of an original SEM negative of a dandelion. The phased input records were separated first by the equivalent of 23.5 mm of air, then 15.5 mm air equivalent, and then 7.5 mm air equivalent by raising and lowering the upper positioner stage. Table 5.1 gives an average value of measurements made from the photographs and recording of zone rings.

An inspection of Table 5.1 verifies that the zone ring diameter is inversely related to the input records separation,  $s$ . A quantitative evaluation of measured and theoretical values was not done because of the limited precision of measurements made.

(a)  
 $s = 23\text{mm}$



(b)  
 $s = 15\text{mm}$



(c)  
 $s = 7\text{mm}$

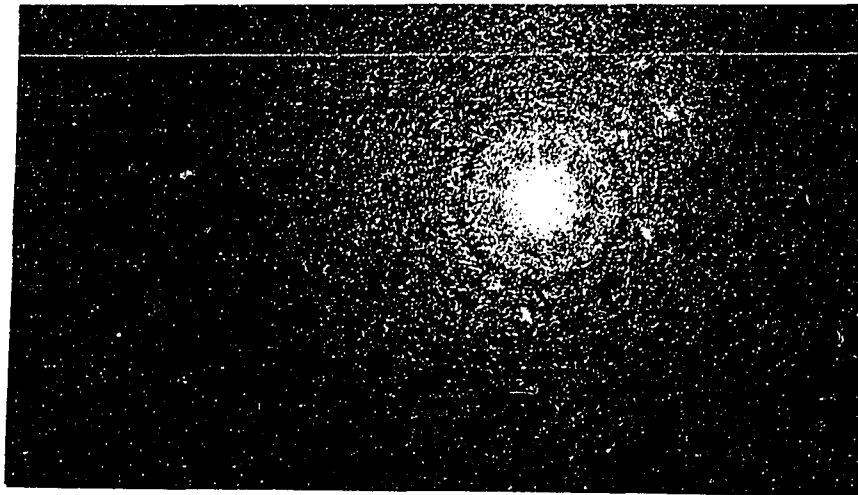


Figure 5.12. Fresnel zone rings for various record separations,  $s$ . Autocorrelation of dandelion SEM photo

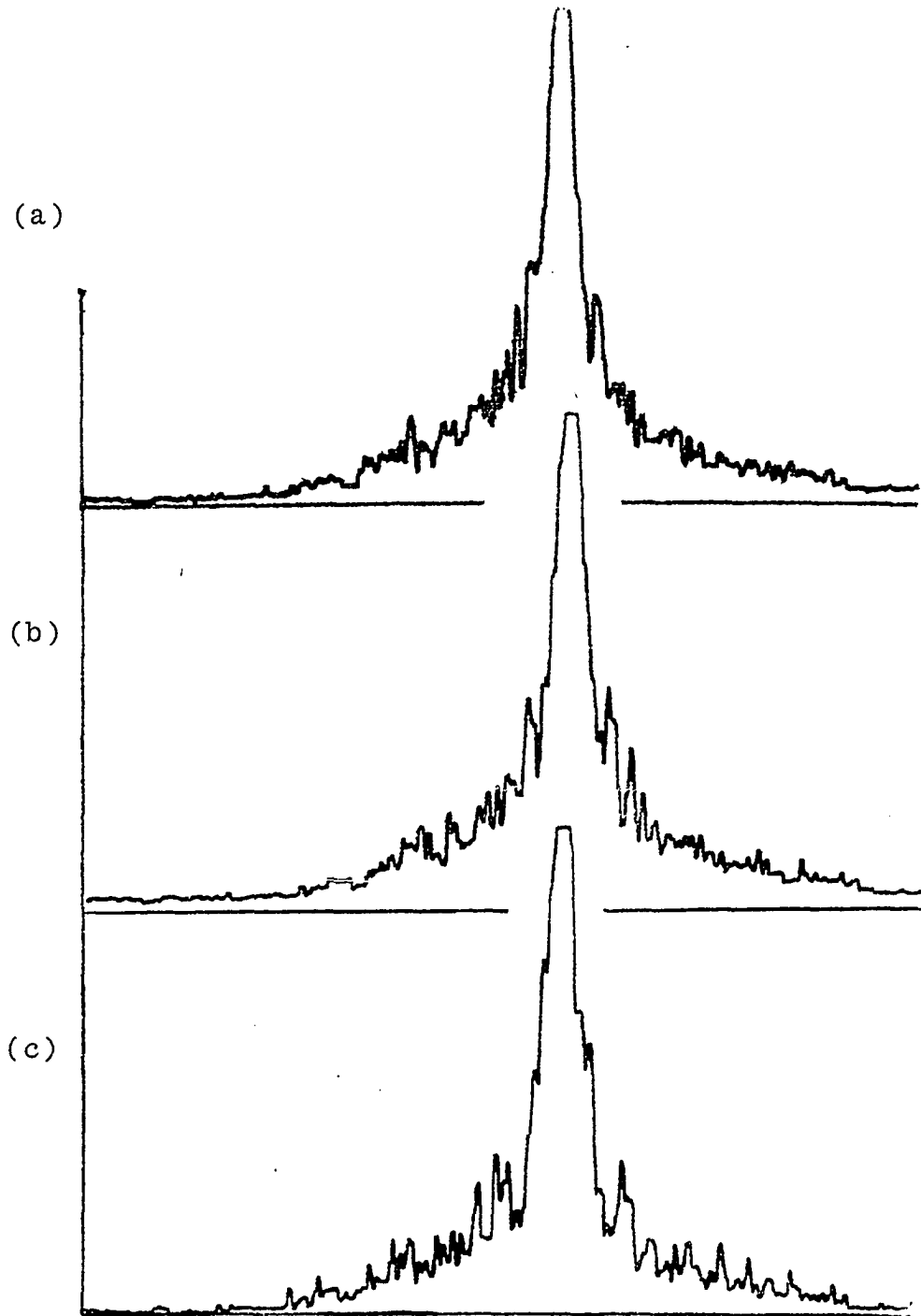


Figure 5.13. Spectrum plots of Fresnel zone rings of Figure 5.12

Table 5.1. Average measured zone ring diameter

Measured separation s(mm of air)	Average measured zone ring diameter (mm) for ring number		
	1	2	3
23.5	9.3	14.0	17.5
15.5	11.5	17.0	20.5
7.5	17.5	25.0	31.5

#### 5.3.5.2. "Autocorrelation" with zone ring offset

As discussed in the theoretical section an offset zone ring pattern was obtained when the input records were shifted so as to move similar pixels off the optical axis. Figure 5.14 shows a Fresnel zone ring pattern with a measured offset of 7.2 mm. Using Equation (5.14) and recalling  $x_m = 3.33 x_f$  we have

$$x_f = \frac{F}{s} x_o' = \frac{x_m}{3.33}$$

or

$$x_o' = \frac{x_m}{3.33} \frac{s}{F} = \frac{7.2\text{mm} \cdot 23\text{mm}}{3.33 \cdot 193\text{mm}} = 258\text{mm}$$

The micro-positioner motion induced to cause the

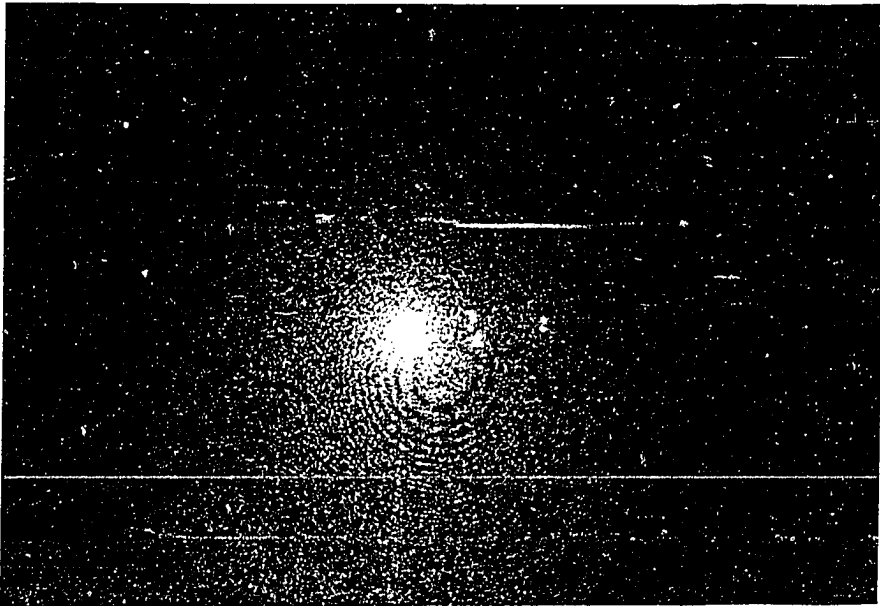


Figure 5.14. Spectrum photograph of Fresnel zone ring  
"autocorrelation" with input records offset  
 $\Delta x = 200\mu\text{m}$  and  $\Delta y = 200\mu\text{m}$

offset was a  $\Delta x = 200 \mu\text{m}$  and a  $\Delta y = 200 \mu\text{m}$  or  $283 \mu\text{m}$ . This optically measured value of  $258 \mu\text{m}$  was low but was accountable for by the error determination of the optical axis (center of bright spot) in the offset measurement.

The real value in the Fresnel zone ring pattern readout has been in the repeatability of differential measurement from one position to another position. For example, when the zone ring pattern is first centered, then the lower micro-positioner was moved several centimeters and then the upper micro-positioner's differential motion made to again center the zone pattern. Typically, the differential motion was repeatable to  $\pm 2$  micrometers.

5.3.5.3. "Cross correlation," absorption versus phased inputs The increased visibility of Fresnel zone rings can be seen by an inspection of Figures 5.15, 5.16 and 5.17. They show photographs and log intensity plots of the frequency plane for one density input and two phased input records. Figures 5.15 and 5.16 are for the cross correlation of the circled area of the terrain stereotransparencies shown in Figure 5.5. The log intensity plots of Figures 5.16 and 5.17 show the zone rings better

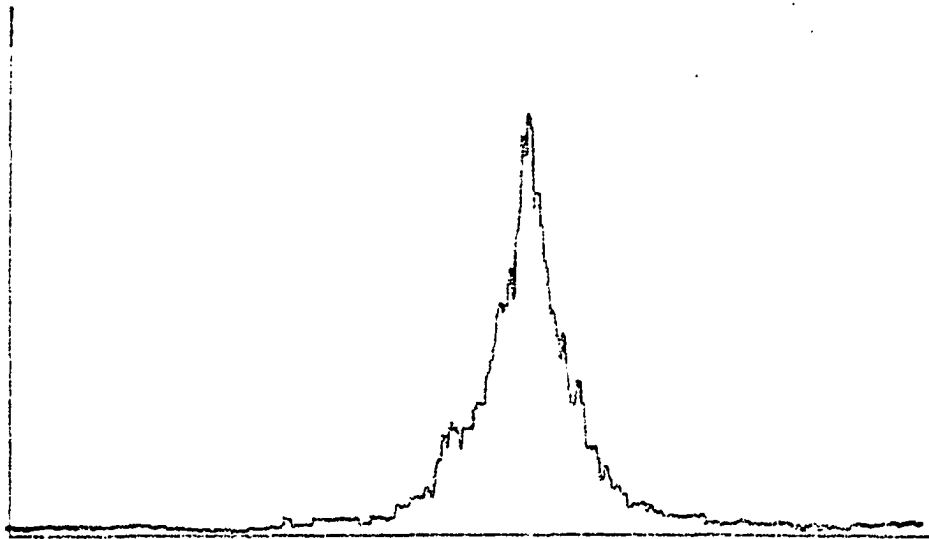
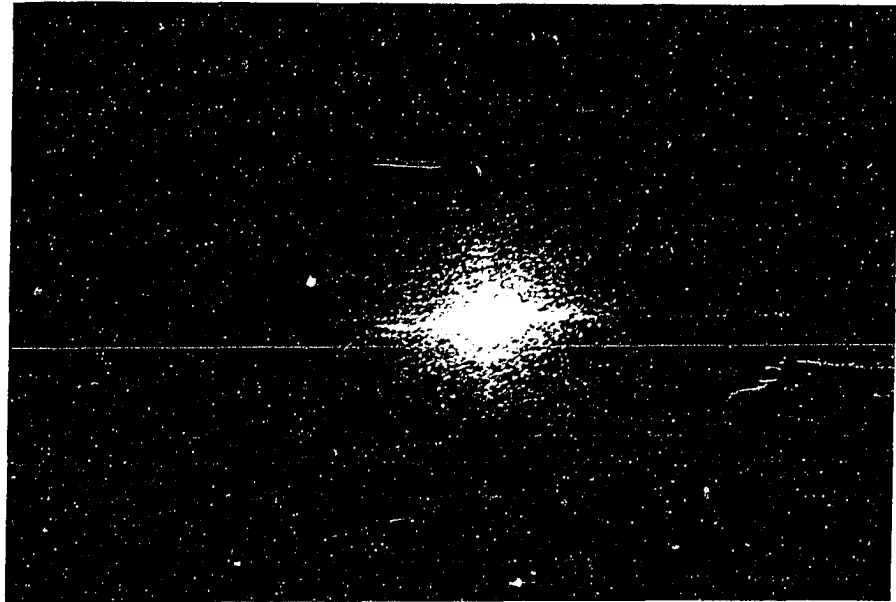


Figure 5.15. Fresnel zone ring "cross correlation" of terrain stereos for density input records

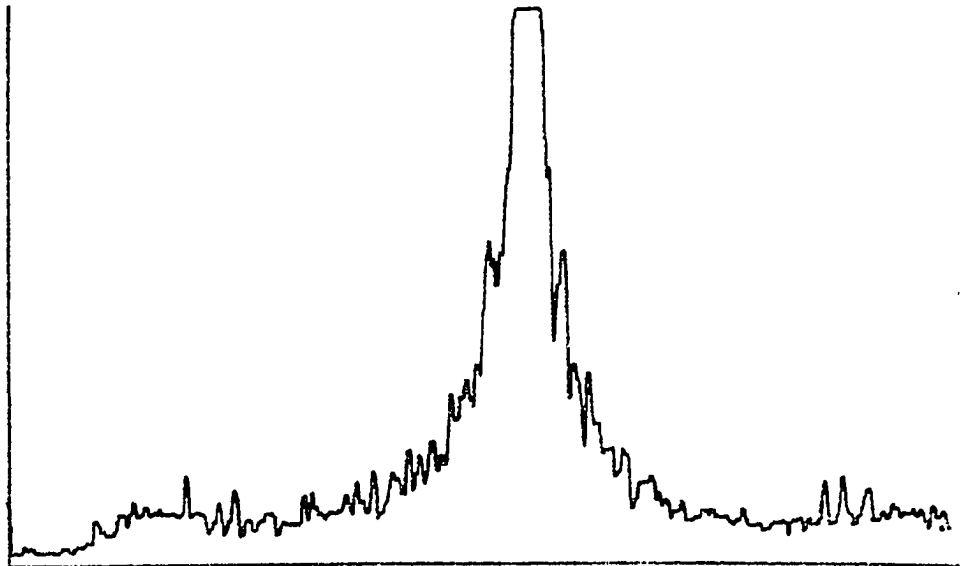


Figure 5.16. Fresnel zone ring "cross correlation of circled area on terrain stereos for phased input records

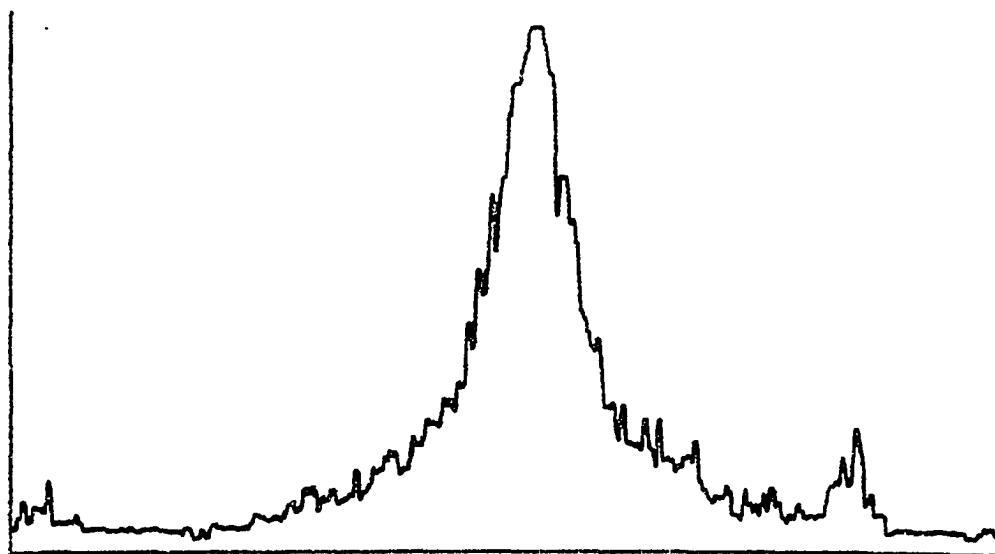


Figure 5.17. Fresnel zone ring "cross correlation" of another site on terrain stereos for phased input records

than the photographs. But past experience has shown that time integration by the eyes and mind gave a very discernible image of the fringe pattern, particularly when it was moved slowly. Some operator education with experience was also noted. Furthermore, a dc light stop inserted at the first frequency plane on the optical axis blanks the bright central spot of the magnified frequency plane increased visual sensitivity and zone ring visibility.

#### 5.3.6. Some experimental examples

The following examples and discussion will hopefully show the application of the Fresnel zone ring "correlation" technique to making measurements in many disciplines and a hint of its various other possibilities.

5.3.6.1. Terrain stereotransparencies      Figure 5.5

is a copy of two topographical stereotransparencies that are used in photogrammetry to measure parallax between images in the two photos. Simply stated, parallax is a displacement of picture elements (pixels) from photo to photo due to a change in viewing position and can be used to determine elevation contours of the terrain. The displacement of pixels on those photos has been observed as a change in position of the zone rings away from the

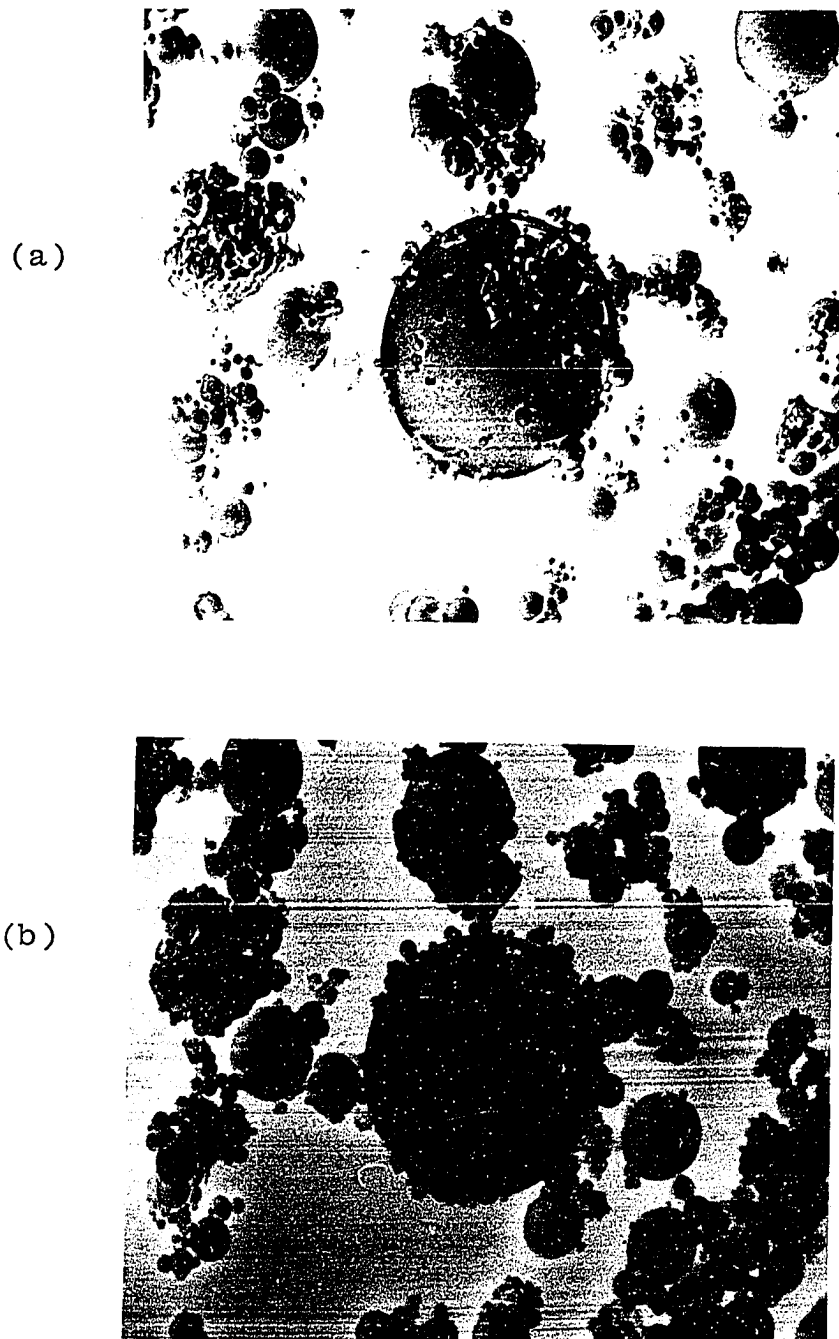


Figure 5.18. Fly Ash by SEM as seen from a relative angle of (a)  $20^{\circ}$  and (b)  $27^{\circ}$

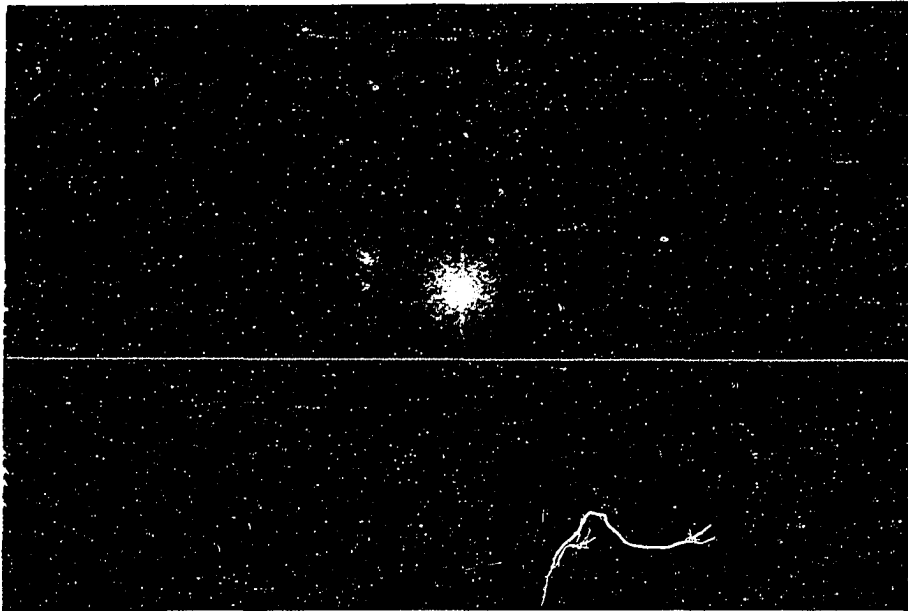


Figure 5.19. Fresnel zone rings for cross correlation of Fly Ash SEM photos with a  $7^{\circ}$  relative viewing angle change

optical axis and has been measured by differential motion of the micro-positioners to re-center the zone rings.

Presently manual operation may be done, but automation of the Fresnel zone ring "correlation" technique is a definite possibility.

5.3.6.2. SEM stereotransparencies      The above discussion on the determination of parallax applies equally well in the investigation of contours (depths) of microscopic objects. A recent source of stereotransparencies is the electron microscope (SEM). Figure 5.18 is a copy of two such photographs of fly ash from a power plant. Figure 5.19 shows the Fresnel zone ring "cross correlation" spectrum of a common area in both photos. Again a differential displacement was measurable from position to position and application of parallax formulas could be used to determine contour lines of the objects.

5.3.6.3. Beam deflection transparencies      The precise measurement of the deflection of a beam with a load is another possible area of application for the Fresnel zone ring "autocorrelation" technique. Figure 5.20 shows two photographs of a simple beam with and without

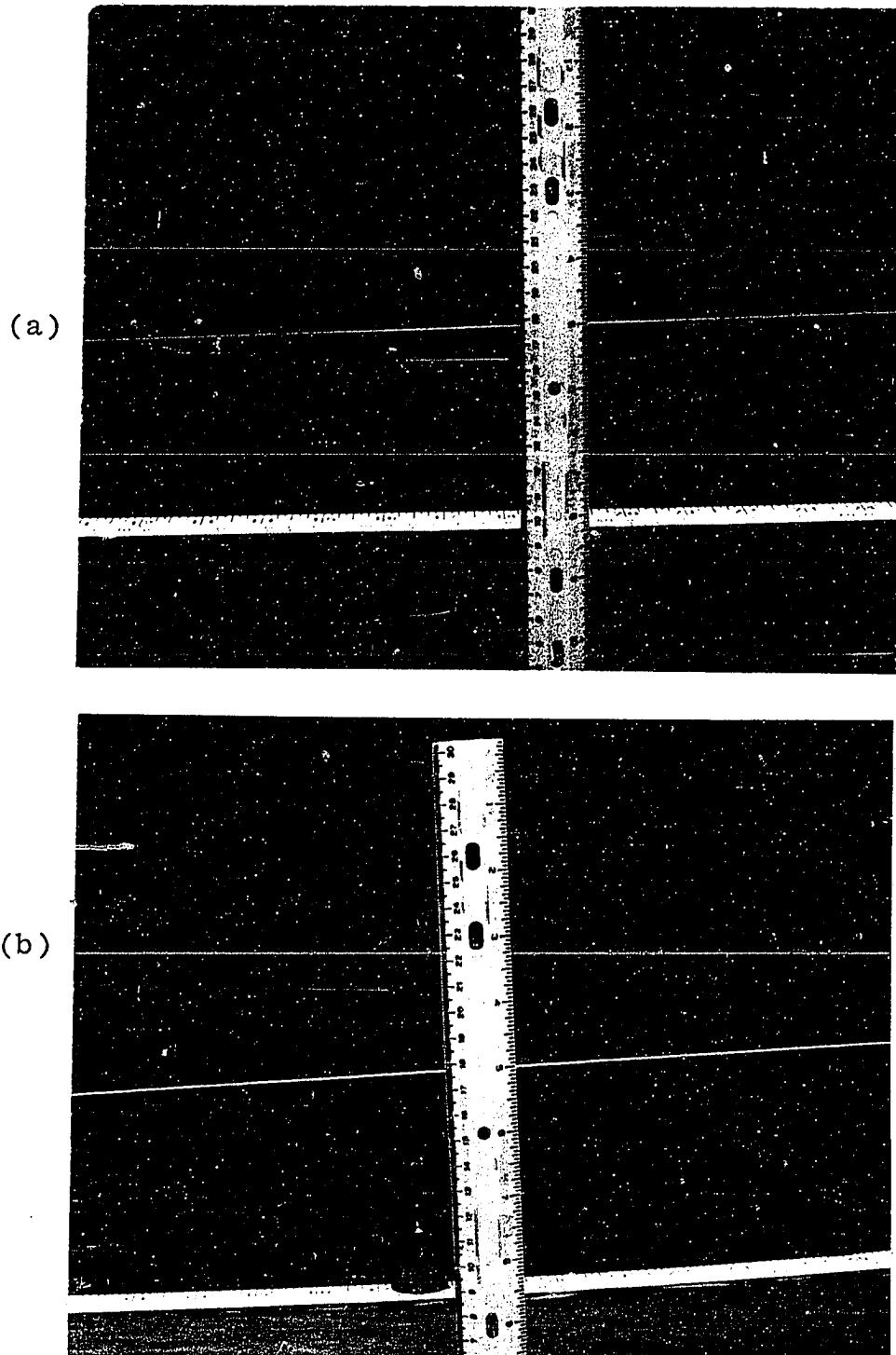


Figure 5.20. Beam deflection measurement with beam (a) unloaded and (b) loaded

a load. An inspection of the position of the beam with respect to the vertical scale, next to the beam, shows an approximate deflection of 9mm.

The negatives of these two photos were copied onto KODAK 120-02 film plate and bleached so as to whiten the original signal spectrum. The phased records were then placed into the apparatus and a concentric zone ring pattern obtained near the "50" on the back reference metric rule. A second concentric zone ring pattern was obtained from a point on the beam near the load. This gave a differential measurement of the beams motion from one photo to the other of 0.735 mm. This was multiplied by the reciprocal of the magnification factor of the reference metric rule of 13.609 and corrected for a beam distance ratio from the camera of  $77 \text{ mm}/87 \text{ mm} = 0.885$ . The calculated beam deflection was 8.853 mm. Other deflection values along the beam were also determinable.

More complicated mechanical structures would require a through knowledge of their geometry, but precise measurements from simple stereo-photographs appear to be possible.

## 6. CONCLUSIONS AND RECOMMENDATIONS

### 6.1. Conclusions

The objective of this investigation was to determine a technique to be used in the determination of pixel displacements occurring between multiple images of a scene. A new type of optical image-image "quasi-correlation" technique has been developed and demonstrated to obtain that objective. This quasi-correlation technique has shown itself to be quite capable for the determination of in-plane differential displacements. Pixel motion of any magnitude between one image to another image has been readily detectable to within a few micrometers in the image coordinate system.

For two-dimensional input records the Fresnel zone ring pattern modulation of the common pixel input signal spectrum was proposed and demonstrated. The zone ring center offset was shown to be a direct function of shifts  $x'_0$ ,  $y'_0$  between common pixels of two cascaded images. The spacing of the zone rings was shown to be inversely related to the separation,  $s$ , of the two input records.

A special case of the two-dimensional theory, one-dimensional records, was discussed where the input records had information in one direction only and the separation distance was zero. This extension of the theory was

demonstrated by the one-dimensional input records with no separation. In this special case the Fresnel zone ring pattern reduces to a uniformly spaced parallel fringe pattern. The fringe spacing was also shown to be inversely related to the signal shift as expected. In this aspect the readout is similar to the usual speckel interferometry.

Advantages of the quasi-correlation technique are the use of noncoherent illumination to make the original records, simple and separate photographic exposures, simple preprocessing, and minimal system rigidity. The adjustable record-separation allows selection of a Fresnel zone ring diameter to give the best ring visibility in different signal spectrums. There is virtually no limit on the maximum shift detectable if separate records can be made and then cascaded and mechanically shifted to within the systems' limits.

Signal spectrum whitening from phased records made by bleaching density records with bromine vapor has been shown to greatly enhance fringe visibility in the optical processing system. Complex exponentiation of input data and log intensity spectrum plots were shown to enhance fringe visibility when digital techniques were used to detect signal shifts. That procedure, used as the input to a second Fast Fourier Transform, permitted the direct

computation of a single-signal shift between signals with ratios of less than 10 to 1.

The output of the demonstrated technique is not a measure of correctness of fit in the normal correlation sense, but provides a good measure of the relative displacement of the pixels.

The single major disadvantage is the need for the input signal record to contain at least a minimum high spacial frequency content. But if not naturally occurring, this can be artificially induced by such techniques as texturing the surface of an object prior to making the photographs.

In conclusion, this dissertation has reported the results of the investigation of a new type of image-image "quasi-correlation" technique for the determination of pixel displacements in cascaded images utilizing coherent light fringe patterns. This was the objective of this dissertation.

## 6.2. Recommendations

The following recommendations are made to improve and/or extend the application of the Fresnel zone ring "correlation" technique.

Investigate in greater depth the parameters involved with signal spectrum whitening from phased input records made by a bleaching process.

Develop and investigate the application of log intensity spectrum plots and double Fast Fourier Transform computational techniques for the determination of signal shifts. Possible implementation may be in such fields as radio astronomy, noise source location, or hyperbolic navigation systems.

Investigate the use of electronic differentiation on serial scan type electronic signals (e.g., SEM, TV and satellites) to enhance the harmonic content of images in at least the scan direction. This should allow application of image-image quasi-correlation techniques to be applied to signals with low spacial frequency content.

Develop the prototype of an automated parallax scanner using Fresnel zone ring correlation techniques. A significant improvement of one or two orders-in-magnitude in the precision of measurement values appears possible.

Investigate the application of new optical input devices

to permit near or actual real-time Fresnel zone ring "correlation" determination. The Itek Corporation's (34) pockels readout optical modulator (PROM) first introduced in 1973, and a new liquid crystal image transducer recently developed by the Hughes Research Laboratory may permit real-time correlation of signals. Jacobson (35) has reported on its use as a real-time optical input device. Gara (36) has just completed an investigation of its phase characteristics for the output image as a function of input light irradiance.

## 7. BIBLIOGRAPHY

1. Whalen, A. D. Detection of Signals in Noise. New York: Academic Press, 1971.
2. Barrow, B. B., Abraham, L.G., Cowan, W. M., Jr. and Gallant, R. M. "Indirect Atmospheric Measurements Utilizing Rake Tropospheric Scatter Techniques - Part I. The Rake Tropospheric Scatter Technique." Proceedings of the IEEE, Special Issue on Remote Environmental Sensing 57, no. 4 (April 1969): 537-551.
3. Goff, K.W. "The Application of Correlation Techniques to Some Acoustic Measurements." Journal of the Acoustical Society of America 27, no. 2 (March 1955): 147-153.
4. Bendat, J. S. and Halvorsen, W. G. "Noise Source Identification Using Coherent Output Power Spectra." Sound and Vibration 9 (August 1975): 15-24.
5. Cohn, M. H. "Introduction to Very-Long Baseline Interferometry." Proceedings of the IEEE, Special Issue on Radio and Radar Astronomy 61, no. 9 (September 1973): 1192-1197.
6. O'Conner, D. "A Role for Holography in Mapping." Laser Focus 7 (December 1971): 23-26.
7. Goodman, J. W. Introduction to Fourier Optics. New York: McGraw-Hill, 1968.
8. Wertheimer, A. and Givens, M. P. "Contour Generation with Optical Processing Systems." Journal of the Optical Society of America 63 (May 1973): 1307-1312.
9. Balasubramanian, N. "Coherent Optics in Photogrammetry." Proceedings of the Society of Photo-Optical Instrumentation Engineers 45 (March 1974): 71-104.
10. Göpfert, M. W. "Contour and orthophoto mapping by optical matched filter correlation of complex exponentiated stereotransparencies." Unpublished Ph.D. dissertation. Library, Iowa State University, Ames, Iowa, 1976.

11. Balasubramanian, N. and Bennett, U. P. "Detection of Image Coincidence in Stereo Pairs Using Phase Correlation." *Optical Engineering* 13, no. 2 (March/April 1974): 147-153.
12. Rotz, F. "Parallax Measurement Using Coherent Optical Processing Techniques." International Optical Computing Conference, April 23-25, 1975.
13. Gray, P. F. and Barnett, M. E. "Matched Filtering of Continuous Tone Transparencies Using Phase Media." *Optics Communications* 14, no. 1 (May 1975): 46-50.
14. Casasent, D. and Furman, A. "Optical Pattern Recognition on Nonvertical Imagery." *Applied Optics* 16, no. 7 (July 1977): 1955-1969.
15. Read, A. A. and Göpfert, W. M. "Optical Cross-Correlation of Complex Exponentiated Input Data," *Optical Engineering* 16 (1975): 605-610.
16. Goodman, J. W. "An Introduction to the Principals and Applications of Holography." *Proceedings of the IEEE* 59, no. 9 (September 1971): 1292-1304.
17. Collier, R. J., Burkhardt, C. B. and Lin, L. H. Optical Holography. New York: Academic Press, 1971.
18. Adams, F. D. and Maddux, G. E. "On Speckle Diffraction Interferometry for Measuring Whole Field Displacements and Strains." Air Force Flight Dynamics Laboratory Technical Report AFFDL - TR - 73 - 123, Wright-Patterson Air Force Base, Ohio, December 1973.
19. Born, M. and Wolf, E. Principles of Optics. New York: Pergamon Press, 1964.
20. Bracewell, R. N. The Fourier Transform and Its Application. New York: McGraw-Hill, 1978.
21. Preston, K. Coherent Optical Computers. New York: McGraw-Hill, 1972.
22. Sommerfeld, A. Lectures on Theoretical Physics, Optics IV. New York: Academic Press, 1954.

23. Gabor, D. "A New Microscope Principle." *Nature* 161 (1948): 777-779.
24. Leith, E. N. and Upatnieks, J. "Wavefront Reconstruction with Continuous Tone Transparencies." *Journal of the Optical Society of America* 53 (1963): 1377-1381.
25. O'Neill, Edward L. "Spatial Filtering in Optics." *IRE Transactions on Information Theory* IT-2 (June 1956): 55-66.
26. Cutrona, L. J., Leith E. N., Palerma, C. J. and Porcello, L. J. "Optical Data Processing and Filtering Systems." *IRE Transactions of Information Theory* IT-6 (June 1960): 386-400.
27. Vander Lugt, A. and Rotz, F. B. "Data Reduction by Coherent Optical Systems." *Photo Optical Data Reduction Proceedings*, St. Louis, MO. March 1964.
28. Vander Lugt, A. "Signal Detection by Complex Spatial Filtering." *IEEE Information Theory* IT-10 (April 1964): 139-145.
29. Stroke, G. W. "Optical Computing." *IEEE Spectrum* 9, no. 12 (December 1972): 24-41.
30. Lander Lugt, A. "Coherent Optical Processing." *Proc. of IEEE* 62, no. 10 (October 1974): 1300-1319.
31. Goodman, J. W. "Operations achievable with Coherent Optical Information Systems." *Proc. of IEEE* 65, no. 1 (January 1977): 29-38.
32. Vander Lugt, A. and Rotz, F. B. "The Use of Film Nonlinearities in Optical Spatial Filtering." *Applied Optics* 9 (January 1970): 215-222.
33. Stark, H. and Garcia, E. "Image Analysis Using Enhanced Spacial Correlation Functions." *Applied Optics* 13, no. 8 (August 1974): 1828-1832.
34. Feinleib, J. "Optical Processing in Real-Time." *Laser Focus* 9 (September 1973): 42-44.

35. Jacobson, A. "A Real-Time Optical Data Processing Device." Information Display 12, no. 1 (1975): 17-22.
36. Gara, A. D. "Phase Response of Liquid Crystal Image Transducer." Physics Department, General Motors Research Laboratories, Warren, MI. (submitted for publication).

## 8. ACKNOWLEDGEMENTS

I wish to give special thanks to my major professor, A. A. Read, for his guidance and advice during my studies and the research herein reported. It has been a long and arduous endeavor. Additional thanks should also go to my graduate committee for their indulgence in my efforts. An extra special thanks goes to my wife, Joyce, for her steadfast encouragement of my efforts and for typing all drafts of this dissertation.

## 9. APPENDIX

## 9.1. Introduction

The following information has been extracted from course notes prepared by Professor A. A. Read of Iowa State University for courses he has taught in coherent optical data processing. The purpose of their inclusion here is to provide a concise and readily available source of definitions, functions, and Fourier Transform pairs often used in optical data processing.

## 9.2. The Fourier Transform

The following expressions are based on the assumption a traveling wave is expressed as  $\exp [j (\vec{k} \cdot \vec{r} - \omega t)]$ , that the paraxial approximation is valid, and that the Fourier Transform pair is taken to be

$$\begin{aligned} \underline{G}_i (f_x, f_y) &= F_i \left\{ \underline{g}_i (x_i, y_i) \right\} \\ &= \iint_{-\infty}^{\infty} \underline{g}_i (x_i, y_i) e^{-j2\pi (f_x x_i + f_y y_i)} dx_i dy_i \end{aligned}$$

$$\begin{aligned} \text{and } \underline{g}_i (x_i, y_i) &= F_i^{-1} \left\{ \underline{G}_i (f_x, f_y) \right\} \\ &= \iint_{-\infty}^{\infty} \underline{G}_i (f_x, f_y) e^{+j2\pi (x_i f_x + y_i f_y)} df_x df_y \end{aligned}$$

where the underline indicates a complex-valued function and the subscript indicates the plane and the coordinate system the integration is being performed on. In the expressions to follow, the  $z$ -axis is coincident with the optical axis of the system with all  $x$ -axes of the different planes colinear, and similarly for the  $y$ -axis. In all cases light is considered to propagate with a component in the positive  $z$ -direction. Also, in all these expressions the quantity  $\underline{s}_i(x_i, y_i)$  denotes a complex-valued phasor amplitude of a wave of angular frequency  $\omega$  that varies spatially over the plane described by the coordinates  $x_i$  and  $y_i$ . The quantity  $\underline{K}$  is simply a complex-valued constant multiplier that affects all values the same.

### 9.3. Transfer Through Open Space

The light distribution on plane  $x_1$ - $y_1$  of Figure 9.1 is

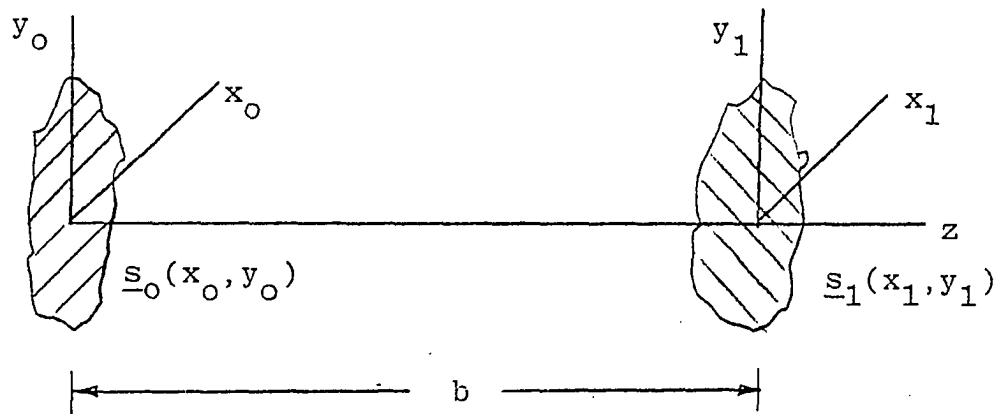


Figure 9.1. Geometry for transfer through open space

$$\underline{s}_1(x_1, y_1) = \underline{K} e^{j(\pi/\lambda b)(x_1^2 + y_1^2)} \cdot \mathcal{F}_0 \left\{ \underline{s}_0(x_0, y_0) e^{j(\pi/\lambda b)(x_0^2 + y_0^2)} \right\}$$

where  $x_1/\lambda b = f_{x_0}$  and  $y_1/\lambda b = f_{y_0}$  relate spatial frequency in the  $x_0$ - $y_0$  plane with position in the  $x_1$ - $y_1$  plane.

#### 9.4. Transfer Through a Convex Lens

The light distribution one focal length behind a convex lens from a light distribution in front of the lens is

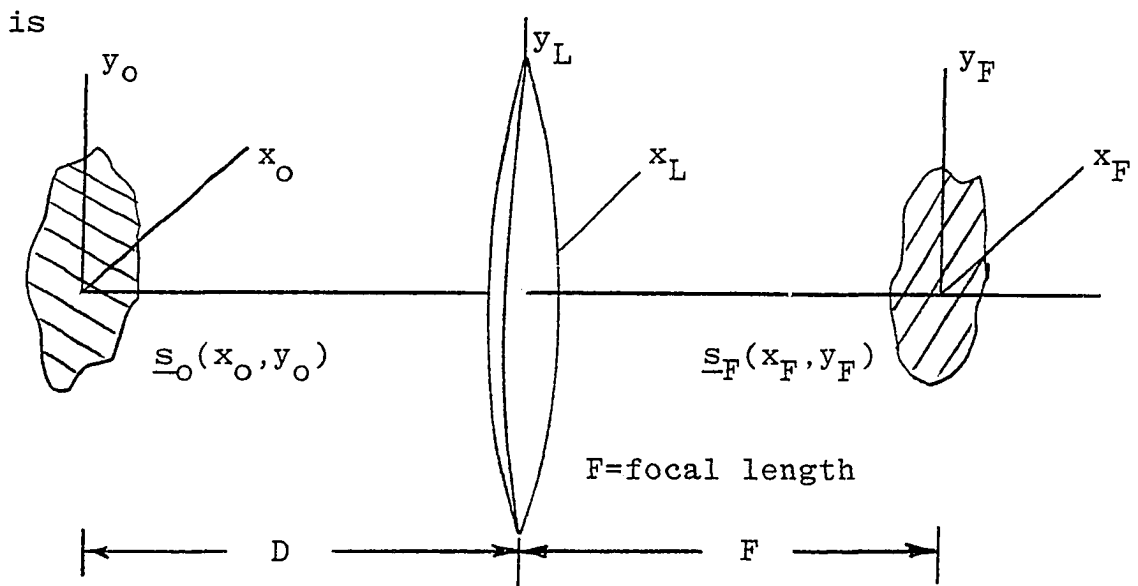


Figure 9.2. Geometry for transfer through a convex lens

$$\underline{s}_F(x_F, y_F) = \underline{K} e^{j(\pi/\lambda F)(1-D/F)(x_F^2 + y_F^2)} \cdot \mathcal{F}_0 \left\{ \underline{s}_0(x_0, y_0) \right\}$$

where  $x_F/\lambda F = f_x$  and  $y_F/\lambda F = f_y$  relate spatial frequency in the  $x_o-y_o$  plane to position in the  $x_F-y_F$  plane.

### 9.5. Some Common Transform Pairs Used In Optical Computing

In all cases below take a and b to be positive real.

If necessary change the algebraic sign of the variables.

$\text{rect}(x/a) = \begin{cases} 1 &  x  < a/2 \\ 0 &  x  > a/2 \end{cases}$	$a \text{ sinc}(af_x) = \sin(\pi af_x)/\pi f_x$
$\text{rect}(x/a) \text{ rect}(y/b)$	$ab \text{ sinc}(af_x) \text{ sinc}(bf_y)$
$\text{sinc}(x/a) \text{ sinc}(y/b)$	$ab \text{ rect}(af_x) \text{ rect}(bf_y)$
$\text{circ}(r/a) = \begin{cases} 1, r = \sqrt{x^2 + y^2} < a \\ 0, r > a \end{cases}$	$a J_1(2\pi a \rho) / \rho; \rho = \sqrt{f_x^2 + f_y^2}$
$\exp[-\pi(x^2 + y^2)/a^2]$	$a^2 \exp[-\pi a^2(f_x^2 + f_y^2)]$
$\exp[j\pi(x^2 + y^2)/a^2]$	$ja^2 \exp[-j\pi a^2(f_x^2 + f_y^2)]$
$\delta(x/a, y/b) = ab \delta(x, y)$	$ab$
$\exp[j2\pi(\frac{x}{a} + \frac{y}{b})]$	$ab \delta(f_x - 1/a, f_y - 1/b)$
$2 \cos[2\pi(\frac{x}{a} + \frac{y}{b})]$	$ab [\delta(f_x - 1/a, f_y - 1/b) + \delta(f_x + 1/a, f_y + 1/b)]$